NASA/TM–20260000527
NESC-RP-19-01470

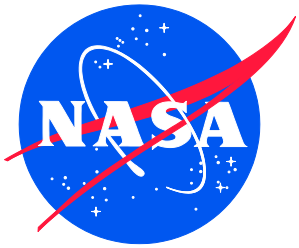

Issues with Qualification of Radiographic NDE Techniques

Eric R. Burke, K. Elliott Cramer
Langley Research Center, Hampton, Virginia

William P. Winfree
Analytical Mechanics Associates, Inc., Hampton, Virginia

Peter A. Parker, Michael D. Squire/NESC
Langley Research Center, Hampton, Virginia

January 2026

NASA STI Program Report Series

Since its founding, NASA has been dedicated to the advancement of aeronautics and space science. The NASA scientific and technical information (STI) program plays a key part in helping NASA maintain this important role.

The NASA STI program operates under the auspices of the Agency Chief Information Officer. It collects, organizes, provides for archiving, and disseminates NASA's STI. The NASA STI program provides access to the NTRS Registered and its public interface, the NASA Technical Reports Server, thus providing one of the largest collections of aeronautical and space science STI in the world. Results are published in both non-NASA channels and by NASA in the NASA STI Report Series, which includes the following report types:

- TECHNICAL PUBLICATION. Reports of completed research or a major significant phase of research that present the results of NASA Programs and include extensive data or theoretical analysis. Includes compilations of significant scientific and technical data and information deemed to be of continuing reference value. NASA counterpart of peer-reviewed formal professional papers but has less stringent limitations on manuscript length and extent of graphic presentations.

- TECHNICAL MEMORANDUM. Scientific and technical findings that are preliminary or of specialized interest, e.g., quick release reports, working papers, and bibliographies that contain minimal annotation. Does not contain extensive analysis.

- CONTRACTOR REPORT. Scientific and technical findings by NASA-sponsored contractors and grantees.

- CONFERENCE PUBLICATION. Collected papers from scientific and technical conferences, symposia, seminars, or other meetings sponsored or co-sponsored by NASA.

- SPECIAL PUBLICATION. Scientific, technical, or historical information from NASA programs, projects, and missions, often concerned with subjects having substantial public interest.

- TECHNICAL TRANSLATION. English-language translations of foreign scientific and technical material pertinent to NASA's mission.

Specialized services also include organizing and publishing research results, distributing specialized research announcements and feeds, providing information desk and personal search support, and enabling data exchange services.

For more information about the NASA STI program, see the following:

- Access the NASA STI program home page at http://www.sti.nasa.gov

- Help desk contact information:

https://www.sti.nasa.gov/sti-contact-form/
and select the "General" help request type.

NASA/TM–20260000527
NESC-RP-19-01470

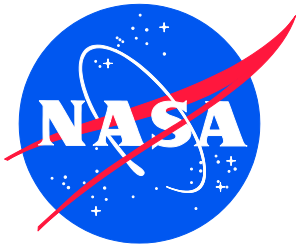

Issues with Qualification of Radiographic NDE Techniques

Eric R. Burke, K. Elliott Cramer
Langley Research Center, Hampton, Virginia

William P. Winfree
Analytical Mechanics Associates, Inc., Hampton, Virginia

Peter A. Parker, Michael D. Squire/NESC
Langley Research Center, Hampton, Virginia

National Aeronautics and
Space Administration

Langley Research Center
Hampton, Virginia 23681-2199

January 2026

Acknowledgments

The NESC team thanks Bence Bartha, Ajay Koshti, Bryan McEnerney, Donald Mendoza, Joseph Minow, Charles Nichols, Donald Roth, Scott Tashakkor, and Sara Wilson (NESC Integration Office) for their peer review of this final report and for their thoughtful comments.

The use of trademarks or names of manufacturers in the report is for accurate reporting and does not constitute an official endorsement, either expressed or implied, of such products or manufacturers by the National Aeronautics and Space Administration.

Available from:

NASA STI Program / Mail Stop 050
NASA Langley Research Center
Hampton, VA 23681-2199

NASA Engineering and Safety Center
Technical Assessment Report

Issues with Qualification of Radiographic NDE Techniques

TI-19-01470

NESC Lead: Michael Squire (K. Elliott Cramer, retired)

Technical Lead: Eric R. Burke

NRB approval date: September 24, 2025

Report Approval and Revision History

NOTE: This document was approved at the September 24, 2025, NRB.

Approved: Timmy Wilson Digitally signed by Timmy Wilson Date: 2026.01.12 11:33:23 -05'00'

NESC Director

Version	Description of Revision	Office of Primary Responsibility	Effective Date
1.0	Initial Release	Michael Squire, NESC Principal Engineer, LaRC K. Elliott Cramer. NESC Chief Engineer, LaRC (retired)	September 24, 2025

Table of Contents

1.0 Notification and Authorization 8

2.0 Signatures 9

3.0 Team Members 10

3.1 Acknowledgements 10

4.0 Executive Summary 11

5.0 Assessment Plan 13

6.0 Problem Description and Background 13

7.0 Analysis 14

7.1 Specimen Fabrication, Characterization and Etching 14

7.1.1 Specimen Fabrication and Characterization 14

7.1.2 Etching Performed on Aluminum Specimens in this NESC Study 16

7.2 Radiographic Measurement Systems 16

7.2.1 Computed Radiography 16

7.2.2 Digital Radiography 17

8.0 Data Reduction 19

8.1 Estimation of Indication Amplitude 19

8.2 Contrast-to-Noise Ratio (CNR) 21

8.3 CNR Calculation 22

9.0 Beam Angle Effects on Radiography Detectability 23

9.1 Review of Literature and Air Force Guidance on Limits for Radiographic Beam Angle 23

9.2 Analysis of Beam Angle Data in Bishop POD Study 24

9.2.1 Background on the Bishop POD Study's Estimate of Radiographic Standard NDE 24

9.2.2 Beam Angle Description 26

9.2.3 Crack Sizes within each Discrete Angle Grouping 30

9.3 Beam Angle Effect Modeling Rationale 31

9.3.1 Beam Angle Effect Modeling Results 32

9.3.2 Conclusion Beam Angle Effects on Radiography POD based Standard NDE POD Study 34

9.4 Experimental Measurement of Variation of Crack Response with Angle 35

9.4.1 CNR as a Function of Incident Angle for lightly etched (AL7) and heavily etched (AL8) cracked specimens 35

9.4.2 CNR as a Function of Incident Angle for AL1 cracked specimen 38

9.4.3 Summarizing CNR as a Function of Incident Angle for all cracked specimens 40

9.4.4 Summary Beam Angle Effects on Radiographic Detectability 42

10.0 Impact of Etching on Radiographic Crack Detection 43

10.1 Review of Radiography Inspection of Etched Crack Specimens by Convair Aerospace and Martin Marietta 43

10.2 Microscopic Examination of Pre-Etch and Post-Heavy Etch Crack Surfaces 44

10.2.1 AL7 Microscopic Image of Pre-Etch 44

10.2.2 AL7 Microscopic Image of After Heavy Etch 46

10.2.3 AL11 Microscopic Image of After Heavy Etch 47

10.2.4 AL8 and AL9 Microscopic Image of After Heavy Etch 47

10.3 Computed radiography images of aluminum plates pre-etch, and post-light etch. 48

10.4 Digital radiography images of aluminum plates following a light and heavy etch. 50

10.5 Simple Simulation of Rotated Specimen with Different Crack Configurations 52

10.6 Analysis of Post-Heavy Etch Specimens 54

10.6.1 AL7 Radiograph Image and Profile Comparison 54

10.6.2 AL11 0° and 10° Radiograph Image and Profile Comparison 55
10.6.3 AL9 Radiograph Image and Profile Comparison 57
10.6.4 AL8 0° and 10° Radiograph Image and Profile Comparison 59
10.6.5 Comparison of Radiographs for 20° Rotation 59
10.7 Estimation of Detectability with Etching with Film Inspection 61
10.7.1 Computational Simulations to Estimate Canyon Depth and Width 61
10.7.2 Equivalence of Etch Canyon, Wire IQI, and Plaque-Type Penetrameter / IQI 64
10.8 Summary of Radiography of Etched Specimens 65
10.9 Analysis of Double-wall Radiography 65
10.9.1 Existing Publications on Double-Wall Radiographic Inspections 66
10.9.2 Measurement procedure for comparing crack indication amplitude for double-wall to single-wall 67
10.10 Results of Single and Double-wall Measurements 67
10.10.1 Aluminum Double-wall Measurements 67
10.10.2 Inconel Double-wall Measurements 71
10.11 Change in CNR between Single Wall and Double Configurations 73
10.12 Computational Simulations of Double-wall Inspection 75
10.13 Summary of Double-wall Inspection 79
11.0 Findings 80
12.0 Observations: 80
13.0 Recommendations: 81
14.0 Alternate Technical Opinion(s) 81
15.0 Other Deliverables 81
16.0 Recommendations for the NASA Lessons Learned Database 81
17.0 Recommendations for NASA Standards, Specifications, Handbooks, and Procedures 81
18.0 Definition of Terms 81
19.0 Acronyms and Nomenclature List 82
20.0 References 82
Appendix 85
A.1 Computational Simulation of the Radiographic Inspection Technique 85

List of Figures

Figure 7.1.1-1. Crack samples the 0.08 mm wide notches are 0.38 mm deep, 0.2 mm wide notches are 1.0 mm deep (Note the illustration is not to scale). 15
Figure 7.2.2-1. Digital radiography measurement system with double-wall configuration..... 18
Figure 7.2.2-2. The full radiographic image of the single plate configuration of AL7 with 0° rotation..... 19
Figure 8.1-1. Typical DR image, region of interest with crack indication, and estimation of the approximate path of the crack. 20
Figure 8.1-2: Profile across crack from acquired data and IQI normalized data. 21
Figure 8.3-1. Points on crack detected for analysis, Location on crack of maximum CNR value, Average and maximum CNR Values for all angles. 22
Figure 9.1-1. Planar Discontinuities with Known Orientation 23
Figure 9.2.1-1. Crack Length versus Depth of the 420 Cracks in the Bishop POD Study 25
Figure 9.2.1-2. Crack Depth-to-Thickness Ratio (a/t*100) of the 420 Cracks in the Bishop POD Study. 25
Figure 9.2.2-1. Bishop (1973). X-ray Beam Angle-to-Flaw Relationship..... 27
Figure 9.2.2-2. Bishop X-ray Exposure Geometry. Radiographic Procedure for Convair (left side) and Martin Marietta (right side) Specimens. 28
Figure 9.2.2-3. Mapping of the crack locations for Convair thin and thick specimens to grids in Bishop report. Grid line spacings are 0.5 inches (1.3 cm). 28
Figure 9.2.2-4. Mapping of the crack locations for Martin Marietta sides A and B of thin specimens to grids in Bishop report. Grid line spacings are 0.5 inches (1.3 cm). 29
Figure 9.2.2-5. Mapping of the crack locations for Martin Marietta sides A and B of thick specimens to grids in Bishop report. Grid line spacings are 0.5 inches (1.3 cm). 29
Figure 9.2.3-1. Range of Crack depth/thickness (a/t) by Angle Grouping 30
Figure 9.3.1-1. 90% Detectable Flaw Size (a90) versus Angle when Combining All Specimen Thicknesses. 32
Figure 9.3.1-2. 90% Detectable Flaw Size (a90) versus Angle for Thin 1.52-mm (0.060-inch) Specimens 33
Figure 9.3.1-3. 90% Detectable Flaw Size (a90) versus Angle for Thick 5.33-mm (0.210-inch) Specimens 34
Figure 9.4.1-1. AL7 DR Images at angles +10, +5, 0, -5, -10 angles of incidence..... 35
Figure 9.4.1-2. IQI normalized AL7 DR with background subtraction applied at angles +10, +5, 0, -5, -10 angles of incidence. 36
Figure 9.4.1-3. IQI normalized AL8 DR for five Beam Angles with background subtraction. 37
Figure 9.4.1-4. Comparison of the angular dependence of CNR of AL7 and AL8 38
Figure 9.4.2-1. Specimen AL 1 radiograph indications with background subtraction applied for five beam angles..... 39
Figure 9.4.2-2. Normalized CNR in specimen AL-1 vs Angle of inspection relative to X-ray beam. 40
Figure 9.4.2-3. Average normalized CNR loss relative to angle for single wall inspection. 41
Figure 9.4.2-4. Realigned average normalized signal loss relative to angle for single wall inspection. 42
Figure 10.2.1-1. Comparison of AL7 micrograph and DR radiograph at 20° rotation 45
Figure 10.2.1-2. Different regions of the micrographs of AL7 indicating the variable gap widths. 45
Figure 10.2.2-1. Comparison of microscopic image of crack and DR radiograph at 20° rotation for AL7 post-heavy etch. (The micrograph has been flipped about the horizonal axis to have the same orientation as the radiograph.)..... 46
Figure 10.2.2-2. High magnification micrographs of a small region of the AL7 crack, with the microscope focused on the surface and at the bottom of the canyon created by the etching..... 47

Figure 10.2.3-1. High magnification micrographs of a small region of the AL11 crack, with the microscope focused on the surface and at the bottom of the canyon created by the etching. 47
Figure 10.2.4-1. Micrographs of a small region on the cracks in AL8 and AL9. 48
Figure 10.3-1. Comparison of computed radiography images of AL7, AL9, and AL11 pre-etch and post-light etch with zero rotation angle. 49
Figure 10.3-2. Computed radiography images of Al 37 pre-etch and post-light etch with zero rotation angle. 49
Figure 10.4-1. Comparison of digital radiography images of AL7, AL9, and AL11 post-light etch and heavy etch with zero rotation angle. 51
Figure 10.4-2. Digital radiograph of AL8 at 0° without and with estimated plot of crack location. The two right plots are of the values of the intensities along the crack path for AL7, AL8, AL9, and AL11 following heavy etches. 52
Figure 10.5-1. Configurations of simulation setup for the specimens in Cases 1-3 53
Figure 10.5-2. Profiles cross the simulation of cracks in Cases 1-3 54
Figure 10.6.1-1. Digital Radiography: Comparison of post-light and heavy etch profile in AL7 for 0° rotation angle. The red line indicates the location of the profile. 54
Figure 10.6.1-2. Digital Radiography: Comparison of light and heavy etch indication profiles for AL7 where specimen is rotated 10° 55
Figure 10.6.2-1. Digital Radiography: Comparison of post-light and heavy etch profile in AL11 for 0° rotation angle 56
Figure 10.6.2-2. Digital Radiography: Comparison of light and heavy etch indication profiles for AL11 where specimen is rotated 10° 56
Figure 10.6.3-1. Digital Radiography: Comparison of light and heavy etch indication profiles for AL9 with the rotation angle of 0° 57
Figure 10.6.3-2. Digital Radiography: Post-light-etch Comparison of the profiles across the center of the 0º rotation radiographs of AL7, AL8, AL9, and AL11 58
Figure 10.6.3-3. Digital Radiography: Comparison of light and heavy etch indication profiles for AL9 with the rotation angle of 10° 58
Figure 10.6.4-1. Radiographic data for AL8 after heavy etch 59
Figure 10.6.5-1. Digital radiographs of AL7 and AL11 at 20° rotation. The two plots on the right are of the peak values of the intensities along the crack path for 20° rotation of AL7, AL8, AL9, and AL11 following heavy etches 60
Figure 10.7.1-1. Simulation configuration with the left image giving the overall configuration and the right image focusing in on the crack surface and the ellipsoidal cylinder used to approximate the canyon 62
Figure 10.7.1-2. Aligned experimental results and simulations for 20° rotation 63
Figure 10.7.1-3. Relative shapes of the elliptic cylinder representation used in simulations for the surface canyons created by heavy etching 64
Figure 10.9.1-1. Comparison of single-wall and double-wall POD as a function of EDM notch volume for film radiography from Bavendiek et al. 66
Figure 10.9.2-1. Measurement configurations for Double-wall Assessment (not to scale) 67
Figure 10.10.1-1. Data obtained for three different separations between the AL7 and a second plate with the same thickness and data obtained for AL7 alone. Plate separations are given in the titles for the images. 68
Figure 10.10.1-2. Data obtained for three different separations between the AL9 and a second plate with the same thickness and data obtained for AL9 alone. Plate separations are given in the titles for the images. 68

Figure 10.10.1-3. Data obtained for three different separations between the AL 11 and a second plate with the same thickness and data obtained for AL 11 alone. Plate separations are given in the titles for the images. 69
Figure 10.10.1-4. For data acquired on AL7, AL9, and AL11 the normalized indication amplitude as a function of distance from the center of the crack 70
Figure 10.10.2-1. Data obtained for three different separations between the C7 specimen and a second plate with approximately the same thickness and data obtained for the C7 specimen alone. Plate separations are given in the titles for the images. 71
Figure 10.10.2-2. Data obtained for three different separations between the C9 specimen and a second plate with approximately the same thickness and data obtained for the C9 specimen alone. Plate separations are given in the titles for the images. 72
Figure 10.10.2-3. For data acquired on specimens C7 and C9, the normalized indication amplitude as a function of distance from the center of the crack 72
Figure 10.11-1. Comparison of the normalized indication of AL36 single wall and double-wall with 20 cm separation 74
Figure 10.12-1. Side view of simulation configuration for a single wall with randomized crack path. 76
Figure 10.12-2. Change in normalized optical density profiles across the crack in aluminum plates with specifics of different configurations in the text 77
Figure 10.12-3. Normalized change in film transparency profiles across the crack in aluminum plates with specifics of different configurations in the text 78

List of Tables

Table 7.1.1-1. Aluminum (2219 Alloy) Crack Panels 15
Table 7.1.1-2. Aluminum (2219 Alloy) Crack Panels List of Inspections Preformed 15
Table 9.2.3-1. Number of Cracks per Angle Group 30
Table 9.4.1-1. Comparison of CNR for AL7 and AL8 as a function of angle. 37
Table 9.4.2-1. AL1 Digital Radiography Contrast to Noise as Function of Angle 39
Table 9.4.2-2. Summary of the normalized response relative to angle of inspection. 40
Table 9.4.2-3. Realigned summary of the normalized response relative to angle of inspection. 41
Table 10.1-1. Martin Marietta data on crack detection before and after etching. 44
Table 10.4-1. CNR Values for AL Samples Pre- and Post-light Etch 50
Table 10.7.1-1 Simulation estimate of depths and widths of canyons with the estimated width and depth from the microscopic images. 63
Table 10.7.2-1 Diameter of equivalent wire IQI d_e and the plaque thickness p_e. 65
Table 10.10.1-4. Measured radiographic crack indication amplitude, noise and CNR for different aluminum double-wall and single-wall specimens and configurations 70
Table10.10.2-1. Measured radiographic crack indication amplitude, noise, and CNR for different Inconel-Inconel double-wall and single-wall configurations 73
Table 10.11-1. Combined Aluminum and Inconel Double-wall CNR Reduction for Different Wall Separations 73
Table 10.12-1. Simulation X-ray source acceleration voltage and exposure for different material and total thickness combinations 75
Table 10.12-2. Simulation Results for Single-wall Double-wall, and Cylinders for Materials and Thicknesses of typical COPVs 78

Technical Assessment Report

1.0 Notification and Authorization

This assessment was requested by the Johnson Space Center (JSC) Nondestructive Evaluation (NDE) Lead, Ajay Koshti. Several issues have been raised relative to both the qualification of X-ray techniques for double-wall radiographic inspections of welds on composite overwrapped pressure vessel (COPV) liners and metallic pressure vessels, as well as deficiencies in the original testing used to establish the acceptable radiography standard detectable flaw size provided in NASA Standard 5009 (NASA-STD-5009).

Key stakeholders include all NASA programs and projects that rely on standard radiographic NDE inspection, including possible implications for tube welding, and missions that use COPV welded liners that are inspected with double-wall radiography. This includes nearly all human and robotic space programs and projects, as COPVs are widely used in launch vehicles and spacecraft.

This assessment was formally authorized by the NESC Review Board (NRB) on February 14, 2021. Dr. William Prosser was assigned as the assessment lead, with Mr. Eric Burke selected as the technical lead. An updated assessment plan was approved on August 16, 2022. Following Dr. Prosser's retirement in November 2024, Mr. Elliott Cramer, NASA Engineering and Safety Center (NESC) Chief Engineer (LaRC), was assigned as the new assessment lead. Upon Mr. Cramer's retirement in July 2025, Michael Squire, Principal Engineer (LaRC), assumed the role of NESC Lead.

2.0 Signatures

Submitted by: NESC Lead

Michael Squire Digitally signed by Michael Squire Date: 2026.01.09 16:14:16 -05'00'

Mr. Michael Squire

Significant Contributors:

Eric Burke Digitally signed by Eric Burke Date: 2026.01.09 16:03:45 -05'00'

Mr. Eric R. Burke

Signature and concurrence received via email, dated January 9, 2026, attached

Dr. Peter Parker

Signature and concurrence received via email, dated December 30, 2025, attached

Dr. William Winfree

Signatories declare the findings, observations, and NESC recommendations compiled in the report are factually based from data extracted from program/project documents, contractor reports, and open literature, and/or generated from independently conducted tests, analyses, and inspections.

3.0 Team Members

Name	Discipline	Organization	* New to NESC Assessments
Core Team			
Michael Squire	NESC Principal Engineer	NESC/LaRC	
Elliott Cramer	NESC Chief Engineer (retired)	NESC/LaRC	
Eric Burke	Technical Lead	LaRC	
Bence Bartha	Mechanics of Materials and Structure	KSC	
Ron Beshears	Mechanical Materials and Structures	MSFC	
Steve Gentz	NESC Chief Engineer (retired)	NESC/MSFC	
Ken Hodges	NDE Deputy Tech Fellow	LaRC	
Ajay Koshti	Mechanics of Materials and Structure	JSC	
Erin Lanigan	NDE	MSFC	
Peter Parker	NDE	LaRC	
William Prosser	NESC NDE Tech Fellow (retired)	NESC/LaRC	
Sam Russell	NDE (retired)	MSFC	
William Schneck	Electronics of Materials	LaRC	*
Raju Subedi	Aerospace Flight Systems	MSFC	
James Walker	Aerospace Flight Systems (retired)	MSFC	
Bill Winfree	NDE (retired)	AMA/LaRC	*
Business Management			
April Albert	Program Analyst	MTSO/LaRC	
Assessment Support			
Betty Trebaol	Project Coordinator	AMA/LaRC	
Linda Burgess	Planning and Control Analyst	AMA/LaRC	
Christa Hahn	Technical Editor	AMA/LaRC	

3.1 Acknowledgements

The NESC team thanks Bence Bartha, Ajay Koshti, Bryan McEnerney, Donald Mendoza, Joseph Minow, Charles Nichols, Donald Roth, Scott Tashakkor, and Sara Wilson (NESC Integration Office) for their peer review of this final report and for their thoughtful comments.

4.0 Executive Summary

This is an initial examination of the limitations of X-ray radiography for the detection of high cycle fatigue cracks. It addresses three specific issues related to the qualification of radiography for inspection of fracture-critical flight hardware: 1) the methodology required to qualify double-wall radiography; 2) how etching may have affected the results of earlier probability of detection (POD) studies, in particular the Bishop [1] POD study, and; 3) how X-ray crack detectability changes with radiation angle of incidence.

The beam angle and effects of etching assessments began with an examination of the Bishop POD study and the reports of Rummel [2] and Anderson [3], which provide details of specimen preparation and an initial radiographic inspection before and after etching. A careful analysis of the data from the Bishop POD study was unable to support or refute the NASA-STD-5009C requirement for a beam angle of ±5°. Consideration of the Rummel report indicates 21% of the cracks examined for the Bishop POD study had radiographic detectabilities that were increased by etching.

Both computed radiography (CR) and digital radiography (DR) measurements were performed on cracked aluminum and Inconel plates with fatigue cracks of different depths. Both the Rummel and Bishop are based on film radiography but this study will seek to establish similar trends using digital radiographic methods and use simulation to relate the trends to film as the digital methods will be more prevalent in future applications. The DR produced more consistent quantitative measurements, therefore much of this report focuses on an analysis of the digital radiographs. The specimens were placed on a rotation stage in the DR system, and measurements were performed at stage/specimen rotation angles from -10° to 20°. The contrast-to-noise ratio (CNR) was calculated for each angle shot, and based on these limited data, the expectation is that the POD for a beam angle of 5° is not significantly different from that for 0°.

The aluminum plates were etched twice: first following the procedure used prior to dye penetrant inspection, which is a light etch, and the second a heavy etch similar to the etch performed by Rummel. Digital radiographs were acquired after the light and heavy etches. The radiographs show that when the crack CNR is high, the etching has little effect. When the CNR post-light etch is small, the additional etching significantly increases the CNR. Computational simulations relate these results to the detectability of the etch by itself with film radiography. A comparison of CIVA simulations and digital radiographs were performed to estimate the amount of material removed at the surface at the crack opening. These CIVA simulations were of simulations of the DR panels. The amount of material removed is then related to the detectability of the crack etch and is discussed in Section 10.7.2.

DR measurements were also performed to simulate double-wall radiographic inspections. DR was performed with a single cracked plate, then a plate of equal thickness was placed between the cracked plate and the detector. Data were acquired with three different distances between the cracked plate and the second plate. Analysis of the data indicated the spacing between the plates did not significantly change the CNR. However, the CNR decreased in double-wall configurations compared to a single cracked plate alone.

Computational simulations were performed for typical composite overwrapped pressure vessel (COPV) materials and wall thicknesses with single wall, two walls in contact, two walls with a separation equal to the interior diameters of typical COPVs, and a cylinder of the same interior diameter. The results of the computational simulations agree with the experimental

measurements, with a decrease in CNR when going from one wall to two walls and the separation between walls not affecting the CNR.

As pointed out in previous reports, the Bishop POD study probably overstates the capabilities of radiographic crack inspection. Relying on its results for double-wall inspections further reduces the reliability of the inspection.

5.0 Assessment Plan

An assessment plan was developed to address three specific issues related to the qualification of radiography for inspection of fracture-critical flight hardware. These included the methodology to qualify double-wall radiography as well as the effects of both etching and radiation angle of incidence on X-ray detectability. To address the issue associated with double-wall radiography, the team evaluated a range of COPV welded liner designs (e.g., materials, thicknesses, and vessel diameters) currently in use within NASA to determine the X-ray POD testing parameters needed for consideration. The team also utilized currently available X-ray NDE modeling software for comparison to testing results in evaluating crack detectability for double-wall X-ray inspection configurations across the range of identified parameters. In parallel, an experimental test program was defined and executed to validate and refine the model analysis predictions. CR and DR X-ray methodologies were used both in the modeling and testing. The desired outcome was to determine whether various test parameters such as the vessel geometry, including wall thickness and diameter, had appreciable effects on defect detection. If so, the plan was to identify a bounding double-wall inspection test configuration, or set of configurations, that can be recommended for future X-ray POD qualification testing to cover the extent of COPV welded liners used by NASA. A formal POD study was not performed as part of this activity. The proposed methodology, if adopted by NASA, would not preclude any provider from performing inspections specific to their vessel design per NASA-STD-5009C guidance.

To address the issues with the historical testing used to support Standard X-ray NDE flaw sizes, X-ray NDE modeling and limited experimental testing were performed to evaluate the effects of etching and X-ray incidence angle on detectability of standard X-ray flaw sizes (*i.e.*, 70% of thickness or 0.7t). These results were used to determine whether the current standard flaw sizes and angle limits are valid, or whether changes should be proposed to these limits.

6.0 Problem Description and Background

On August 1, 2019, William Prosser, NASA Technical Fellow for NDE (now retired), presented an initial evaluation to the NRB titled “Issues with Qualification of Radiographic NDE Techniques (TI-19-01470).” In this presentation, three issues were identified that are the subject of this assessment. The first was the need for agency-wide consistent treatment of qualification testing for double-wall radiography that is widely used to inspect close-out welds in metallic pressure vessels and COPV liners. It was determined within NASA these inspections were not being uniformly executed across the agency. These inspections as NASA Special NDE, per the guidance in NASA-STD-5009C, and required that POD demonstration tests be performed in a simulated double-wall X-ray inspection configuration. The simulation consists of two thicknesses of plates with a separation distance to be representative of the vessel diameter, with the plate containing fatigue cracks to be detected on one side and the other representing the second vessel wall. However, another center had previously allowed inspectors to be qualified for double wall radiography with demonstration tests including only a single flawed panel. Subsequent testing by that center demonstrated that personnel that passed the test for a given flaw size in the single-wall configuration could not pass the same test in a simulated double-wall configuration. Thus, the agency NDE leadership has determined that all double-wall X-ray qualification shall be performed in a double-wall configuration. The purpose of this assessment was to determine if the type of material, thickness, and wall spacing have any significant

influence on detectability such that a preferred (conservative) double-wall test configuration should be recommended for use by the agency.

The second and third issues identified were related to the testing performed to establish the NASA Standard X-ray flaw sizes provided in NASA-STD-5009C. It is noted that there will be variation between the film results and the testing preformed in this study. It was determined from reviewing the original test data that all the flaws in the testing had been etched, as required for penetrant inspection, since the flaws were also used in penetrant POD testing. However, etching is not required nor used in practice before X-ray inspections, and a concern was raised that the standard X-ray flaw sizes may not be conservative. It is noted that pressurized structures require proof testing, as well as both surface and volumetric inspections before and after proof. Thus, testing and further analysis of the original test data was planned to determine whether etching has a significant impact on detectability of flaws with X-ray. Another issue was that the original test data may not have adequately covered the range of allowable angles of the crack with respect to the X-ray beam, which is +/- 5°. Again, testing and modeling were planned to determine whether that angle restriction should remain the same or be adjusted.

7.0 Analysis

7.1 Specimen Fabrication, Characterization and Etching

7.1.1 Specimen Fabrication and Characterization

Crack specimens with starter notches were fabricated from dog-bone tensile samples with an electro-discharge machined (EDM) and were fatigued tested in a tension-tension cyclic frame to grow a crack to a target length and depth. Development tests were performed to determine the size of the EDM starter notch, the tensile load level, and number of cycles to yield a crack of the desired size. Once a crack was grown in the panel, the surface of the panel was milled to remove the EDM starter notch. This resulted in a crack that may have metal smeared over the outside surface of the crack. Figure 7.1.1-1 shows the design of the crack panels. Table 7.1.1-1 provides relative dimensions for all of the aluminum samples discussed in this paper. Table 7.1.1-2 provides a list of all of the aluminum samples and which measurement techniques were performed on that sample and by which NASA center. Note that phased array ultrasound (PAUT) after etching of the specimens was used to measure the crack depth[1] and dye penetrant was used to size the surface breaking length of the cracks for the data presented in Tables 7.1.1-1 and 7.1.1-2.

[1] Note standard calibration of the PAUT unit was performed before measurements.

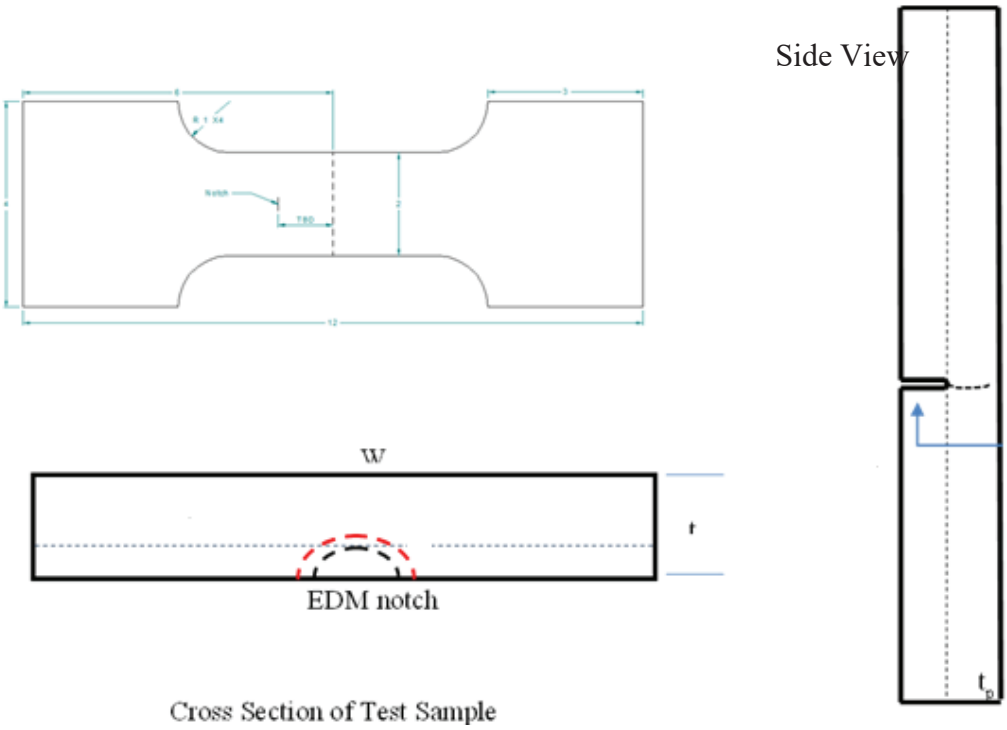

Figure 7.1.1-1. Crack samples the 0.08 mm wide notches are 0.38 mm deep, 0.2 mm wide notches are 1.0 mm deep (Note the illustration is not to scale).

Table 7.1.1-1. Aluminum 2219 Alloy Crack Panels

Specimen	Thickness (mm)	Crack length (mm)	PAUT estimate of crack depth (mm)	Depth/thickness (A/T) (mm)
AL1	10.39	20.85	5.13	0.49
AL7	2.74	11.68	2.72	0.99
AL8	2.79	7.65	1.27	0.45
AL9	3.43	11.43	2.01	0.63
AL11	4.70	13.84	4.09	0.87
AL36	12.70	37.41	5.51	0.43
AL37	18.52	33.66	10.19	0.55

Table 7.1.1-2. Aluminum 2219 Alloy Crack Panels List of Inspections Performed

	Pre-Etch	Post-Etch
AL1	PAUT (MSFC)	CR (MSFC), DR (LaRC)
AL7	CR (MSFC), PAUT (MSFC)	CR (MSFC), DR (LaRC)
AL8	PAUT (MSFC)	CR (MSFC), DR (LaRC)
AL9	CR (MSFC), PAUT (MSFC)	CR (MSFC), DR (LaRC)
AL11	CR (MSFC), PAUT (MSFC)	CR (MSFC), DR (LaRC)
AL36	PAUT (MSFC)	CR (MSFC), DR (LaRC)
AL37	PAUT (MSFC)	CR (MSFC), DR (LaRC)

7.1.2 Etching Performed on Aluminum Specimens in this NESC Study

Aluminum crack samples manufactured for this study were etched at NASANASA's Marshall Space Flight Center (MSFC).). The first etch procedure performed on the specimens followed Organizational Work Instruction EM30-WI-021: "Process Specification for Etching Aluminum Alloys Prior to Dye Penetrant Inspection." Under this procedure, the surface is degreased and cleaned by a vapor degreaser, solvent, or mild alkaline cleaning solution; dried; and masked. The etchant can be hand swabbed onto the surface, or the part can be immersed in a vat of the chemical etchant. For this study, it was hand swabbed. The chemical used for etching was TURCO MIL-ETCH. For swabbing, 16 oz. was diluted with water to a gallon. Manual swabbing was performed at room temperature. The etch time was established such that 0.005 mm to 0.01 mm was removed for machined surfaces, consistent with the guidance in NASA-STD-5009C. For aluminum, 0.01 mm material is required to be removed from the machined surface for the light etch. The etched area was thoroughly washed with demineralized water and the deoxidizer solution (Oakite® LNC (deoxidizer) diluted with water to a 10% concentration) was applied for 5 to 15 minutes. The surface was again rinsed with demineralized water and dried prior to inspection and material removal was in the remainder of this report this is referred to as the "light" etch.

The second etch procedure, referred to in this report as the "heavy etching," attempted to approximate the etch performed by Rummel [2]. This etch followed this same procedure except for the etch time. The etchant was left on long enough to remove an additional 0.05 mm of material, 5x more material than was removed with the previous etch. The samples that were heavily etched had also been lightly etched, with; a total of 0.055-0.060 mm removed.

7.2 Radiographic Measurement Systems

7.2.1 Computed Radiography

CR is often considered as a replacement for conventional radiography and uses equipment similar to that used for conventional radiography, except that in place of a radiographic film a reusable fluorescence imaging plate (IP) is used to create the X-ray images. The IPs are generally housed in a cassette and positioned in the appropriate orientation with the object under examination between the X-ray source and the plate/cassette. IPs are processed through an on-site portable laser scanner instead of developing an exposed film in a darkroom using chemicals. The general mode of operation for the portable scanner is to first subject the IP to a special laser scanner that reads and digitizes the image. The IP is then erased using high-intensity ultraviolet light. The digital image can be viewed and enhanced (e.g., contrast, brightness, filtration, and zoom) using software with functionality like that of other conventional digital image processing software. The CR IP contains a photostimulable storage phosphor layer (typically 0.1 to 0.3 mm thick), which stores the radiation shadowgram as a latent image within the phosphor layer as elevated electron energies. When the IP is transported through the scanner, the scanning laser beam causes the electrons to relax to lower energy levels, emitting light that is converted by a photomultiplier to an electrical signal. The electrical signal is then digitized and processed by a computer, resulting in a digital radiographic image that can be viewed, stored, and analyzed. IPs can theoretically be reused thousands of times if they are handled carefully and under certain radiation exposure conditions. IP handling under industrial conditions often results in damage after a few hundred uses. Mechanical damage (e.g., scratches and abrasions) is common, as well as radiation fatigue or imprinting due to high-energy applications. An image can be erased by

exposing the IP to a room-level fluorescent light, but more efficient, complete erasure is required to avoid signal carryover and artifacts. After complete erasure, the IP can be reused.

The system used in this study is located at MSFC and is a FUJIFILM DynamIx HR2, which can scan the CR plates at high-resolution ranging from 25 to 100 μm pitch. High-resolution plates from FUJIFILM were also used (DynamIx HR2, Imaging plate), offering high-resolution readings down to 25 μm pitch.

7.2.2 Digital Radiography

Industrial DR panels are not generally as portable as CR and is most often performed in a facility. For this study, it provided more consistent quantitative measurements and increased spatial resolution in the inspection plane. For this study, digital radiography had a particular advantage over CR in that multiple measurements can be performed without remounting the crack specimen.

DR is a form of radiography that uses X-ray-sensitive digital detector arrays to directly capture X-ray photon counts during inspection. DR uses an amorphous silicon detector array, and the incident X-ray radiation is converted into an equivalent electric charge forming a digital image. The image is immediately transferred to a computer system without the use of an intermediate cassette.

The DR system used in this report is located at NASA's Langley Research Center (LaRC) and consists of an X-ray flat panel detector, an X-ray source, and a positioning/rotation stage located between the source and the detector. The system uses a PerkinElmer XRD 1621 xN ES detector panel that has a 200 μm pixel pitch.

The X-ray source has a variable acceleration voltage, spot size, and current. The maximum current is determined by the acceleration voltage and the spot size. Unless otherwise specified, the acceleration voltage was 75 keV;, the source spot size was 5 μm, and the current 55 mA for measurements performed for this report.

The X-ray flat panel detector has a 2000-by-2000 element array with a 0.2 mm pitch. After acquiring a radiographic response, the detector array transfers the data to a data acquisition computer to form an image. Multiple images are averaged to give a single radiographic image for a particular configuration of the specimen. To obtain a single radiographic image for this report required approximately 15 minutes. The resulting images were transferred to disk storage, then transferred to other computers for data analysis.

A picture of the system is shown in Figure 7.2.2-1 with the crack specimen placed close to the source to allow for geometric magnification of the crack indications in the resulting images. This enabled the plane of the cracked specimen to be imaged with a magnification of 14x and a spatial resolution of 14.3 μm, which is considerably better than the 200 μm resolution of the DR detector panel. This is closer to a literature film resolution value cited as being better than 50 μm. The intent was not to duplicate a film measurement, rather to quantify any changes in crack indication amplitude as a function of different specimen configurations.

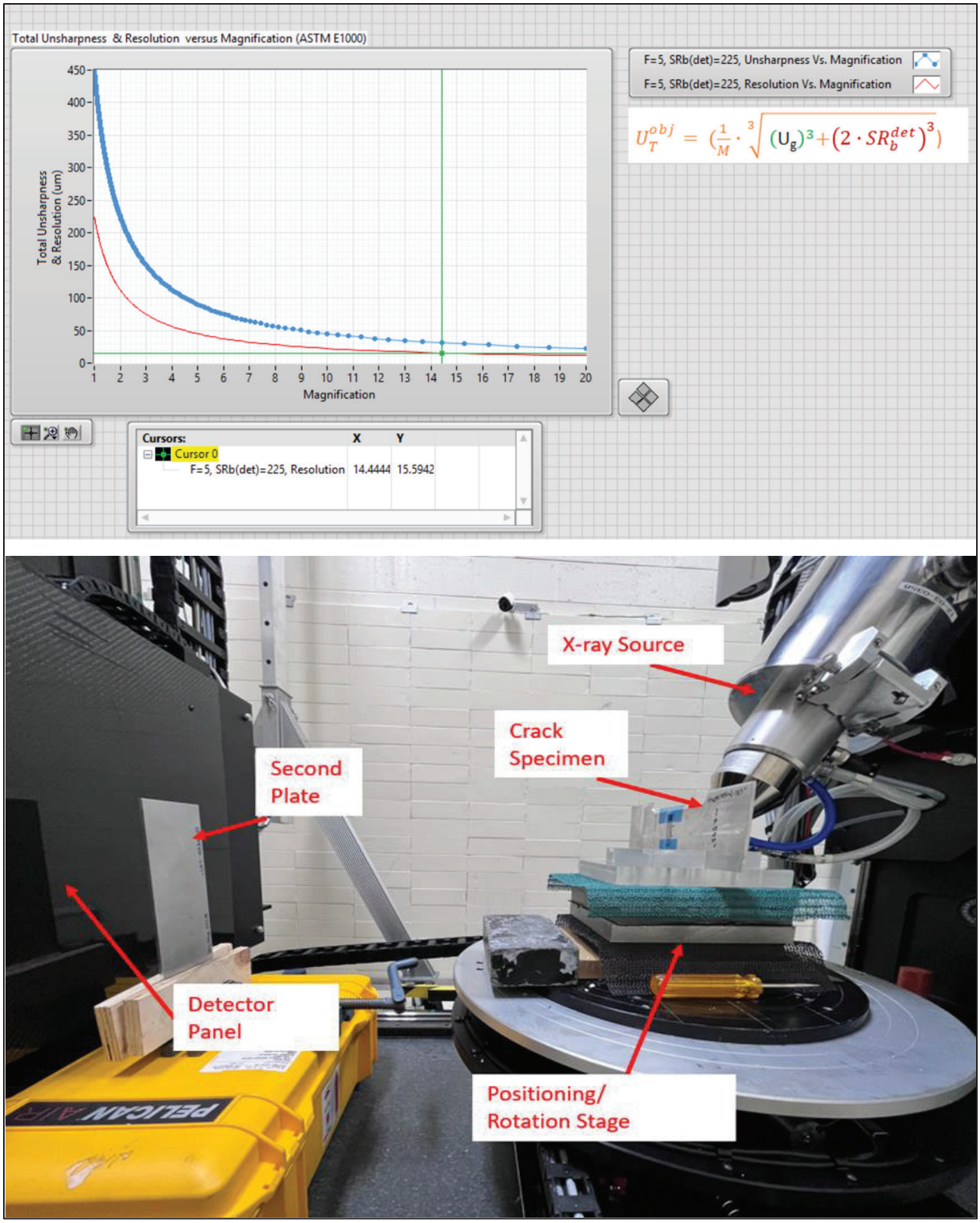

Figure 7.2.2-1. Digital radiography measurement system with double-wall configuration.

Before acquiring data on a given specimen, unless otherwise specified, a three-hole 0.25 plaque image quality indicator (IQI) was mounted on the specimen. This allowed us to achieve the

required the sensitivity of the radiographic images for subsequent quantitative characterization of the crack's radiographic response. The three-hole plaque IQI is an ASME standard and is discussed in detail in ASTM E1025-18 [4].

The specimen was placed on the positioning/rotation stand located between the source and detector, such that the crack side of the specimen was facing the detector, and the specimen was parallel to the detector face. The specimen was then translated in a direction parallel to the detector face to align the center of the crack with a line passing through the center of the detector, center of rotation, and source location. The proper alignment with the center of the detector and beam should produce the maximum crack indication amplitude.

An acquired image for specimen AL7 is shown in Figure 7.2.2-2 with a rotation angle of 0°. The left side of the image is a portion of a 0.25 IQI plaque, with the three 1T, 2T, and 4T holes clearly visible. To the right of the IQI is the crack indication.

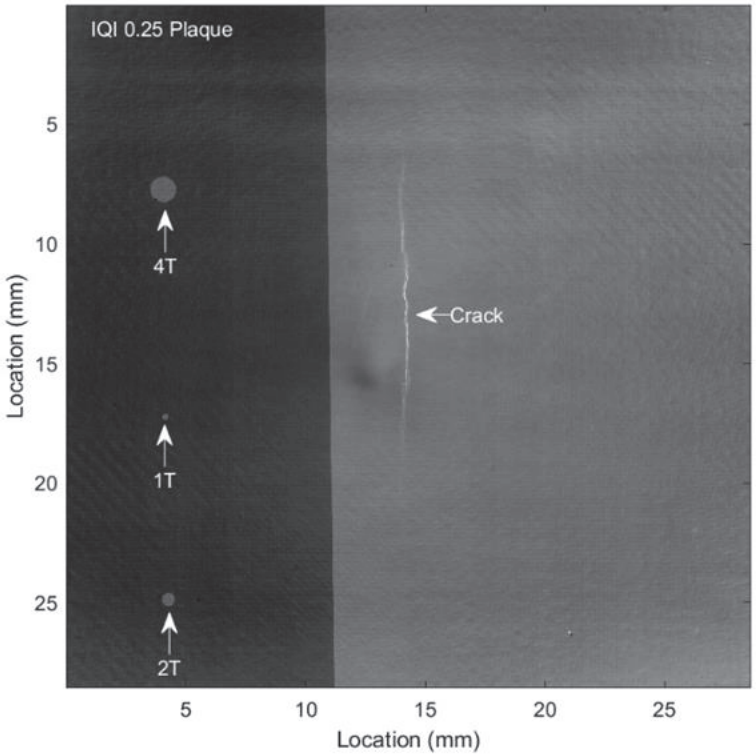

Figure 7.2.2-2. The full radiographic image of the single plate configuration of AL7 with 0° rotation.

8.0 Data Reduction

8.1 Estimation of Indication Amplitude

A quantitative comparison of different crack indications can be made by finding an IQI normalized indication amplitude. The IQI indication amplitude is calculated by first selecting a region of interest containing both the crack and IQI indications. The original DR image and the selected region of interest are shown in the left and center images, respectively, in Figure 8.1-1. As can be seen from the region of interest image, the crack does not fall on a straight line, so an estimate for the path is made by finding the location of the maximum along each horizonal

profile and smoothing those locations as a function of y with a spline. The estimated path of the crack is shown superimposed on the crack in the right image of the Figure 8.1-1.

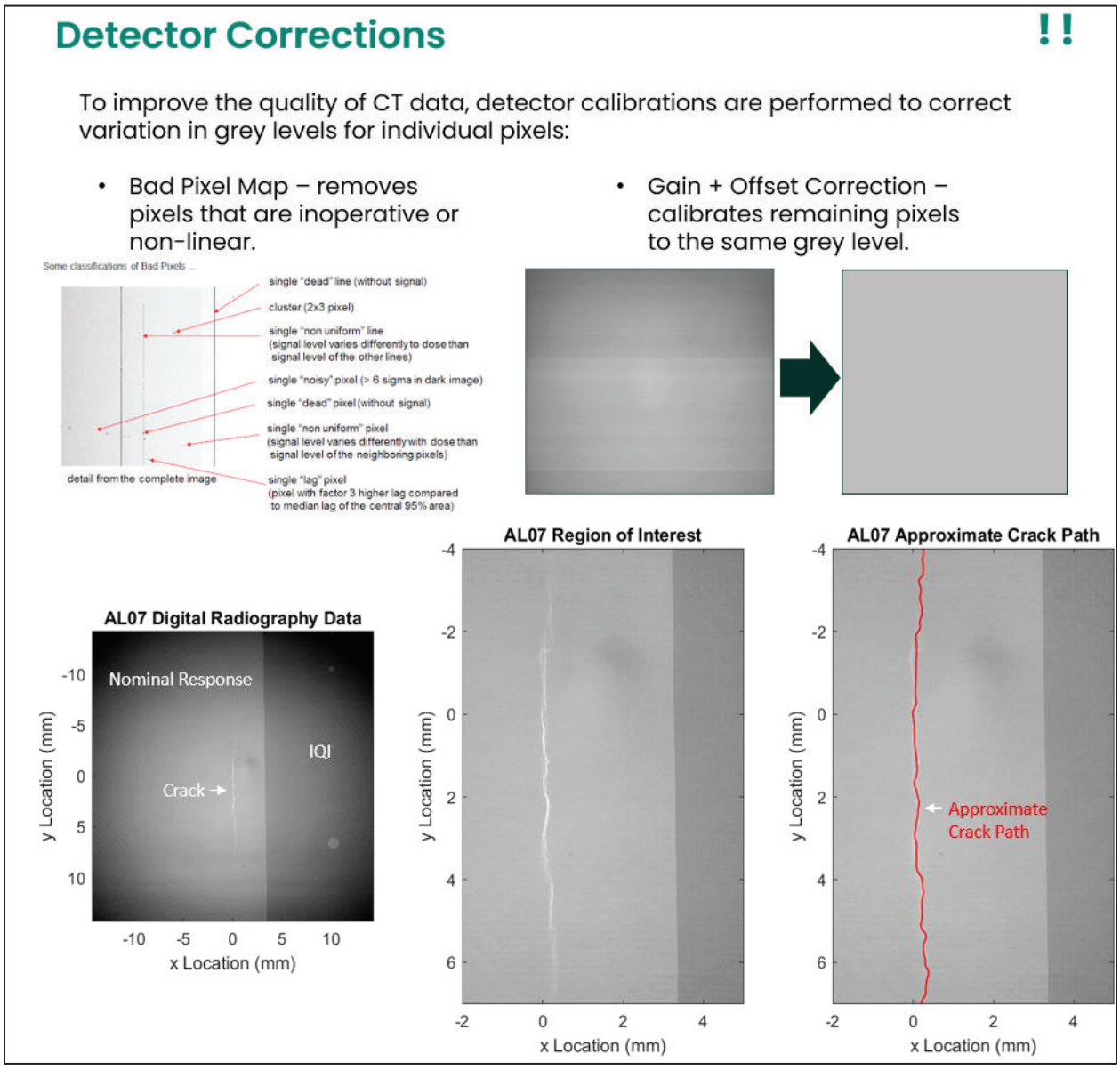

Figure 8.1-1. Typical DR image, region of interest with crack indication, and estimation of the approximate path of the crack.

To find an IQI normalized amplitude, the image is first normalized by dividing the image by the change in intensity at the edge of the IQI. This change in intensity is estimated by fitting the intensities with an error function. The parameters of a polynomial surface fit of the nominal response portion of the normalized image are used to estimate a background for the entire region of interest. This background is subtracted from the normalized image, yielding an image where the nominal regions of the image are approximately zero and the IQI value is approximately -1, as can be seen in the "Normalized Profile" in Figure 8.1-2 (center image). The IQI normalized indication amplitude reported in this report is the amplitude of the crack indication shown in the center plot. The plot on the far right of Figure 8.1-2 indicates how the IQI normalized indication

amplitude is different for different locations along the crack. The indication amplitudes are an average value of the indication along a segment crack path. When reporting values for different configurations of the same specimen, the same region of interest is used for all of the radiographs.

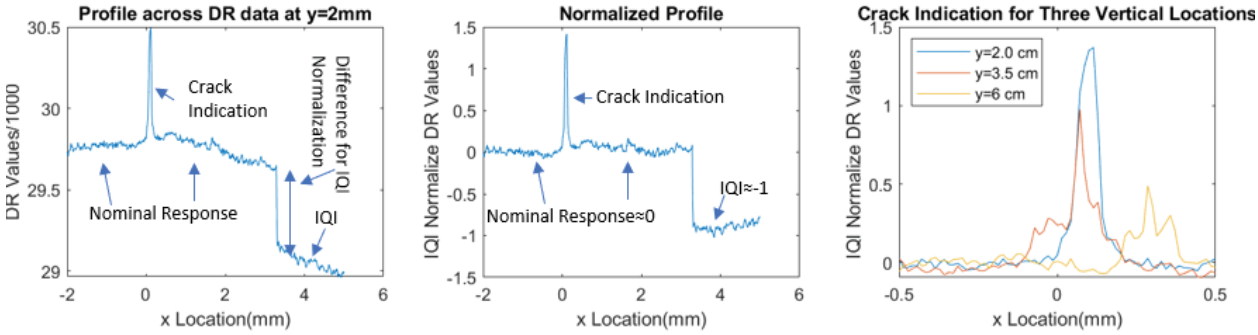

Figure 8.1-2: Profile across crack from acquired data and IQI normalized data.

8.2 Contrast-to-Noise Ratio (CNR)

CNR can be generalized as the quotient of the mean value of the target area divided by the standard deviation of the noise. CNR calculations were performed in accordance with ASTM E2737 [5]. For the DR data, a custom algorithm was used to map CNR values along the length of the crack.

$$CNR = \frac{\|I_{bg} - I_t\|}{\sigma_t} \quad \text{(Eq. 1)}$$

$$I_{bg} = IntestityIntensity\ of\ Backround\ Measurement$$

$$I_t = Intestity\ of\ Target\ Measurement$$

$$\sigma_t = Standard\ Deviation\ of\ the\ Noise$$

Rose [6] defines a criterion for a circular indication, which is proportional to the CNR (signal-to-noise ratio in the paper) of an indication times the solid angle subtended by the circle from the viewers perspective. When the criterion is greater than the "threshold signal-to-noise ratio" referred to as k, the circle is visually detectable. By experimentation, Rose finds, "k lies in the neighborhood of 5."

Tisseur [7] defines a similar criterion for a rectangular indication, which is proportional to the square root of the area times the CNR. If the criteria are greater than 1.5, the rectangle is detectable. Tisseur data also indicate there is not an exact threshold where the rectangle transitions from undetectable to detectable, rather when the criteria is around 1.5. A comparison of the threshold for Rose (k=5) and Tisseur (k=1.5) indicates the threshold is dependent on the shape of the indication.

A crack indication is not circular or rectangular, nor is its intensity constant along the length of the crack, but it is expected that CNR times the indication length would be proportional to a similar criterion. When the criteria those criteria approach an unknown constant, a crack indication transitions from undetectable to detectable. Determining a value of that constant is beyond the scope of this effort, however, small changes in CNR are not likely to change a crack's detectability.

8.3 CNR Calculation

Fiji, an image processing package in ImageJ [8], from the National Institutes of Health, was used to view all the radiograms. A region of interest (ROI) is drawn over the crack to bound the region for analysis.

In the DR images, there is considerable variation in the regions of the specimen with the nominal specimen response. This becomes very noticeable when trying to calculate CNR values for these images. For some cases, the CNR values for the raw data are below 2.5, but the cracks are clearly visible.

To correct for the background variation of the image, a rolling ball background subtraction technique was applied. A background image was calculated from the average of a large circular region around each pixel. This background image was subtracted from the original image. This technique is very good for removing the overall background signal while not affecting the signal response.

A custom plug-in was then executed that automatically detected the crack path and generated both a crack signal and an average signal required for CNR. These calculations were then performed along the length of the crack to generate an array of CNR values along the entire crack length. Finally, an average crack CNR response and maximum CNR response was recorded for the specimen.

Due to the inherent "noisiness" of the CR images, a median filter was applied with a radius of 2 pixels. In the case where multiple images were taken on the same sample, such as for multiple angle shots, image gray levels were set so that the average value in the reference ROI on the zero-angle image and reference ROI on the comparison image were equal. The output of the ImageJ analysis software is shown in Figure 8.3-1, with the crack path shown in the left image, the location of the maximum CNR shown in the center image, and a plot of the average and maximum CNR values shown in the plot on the right.

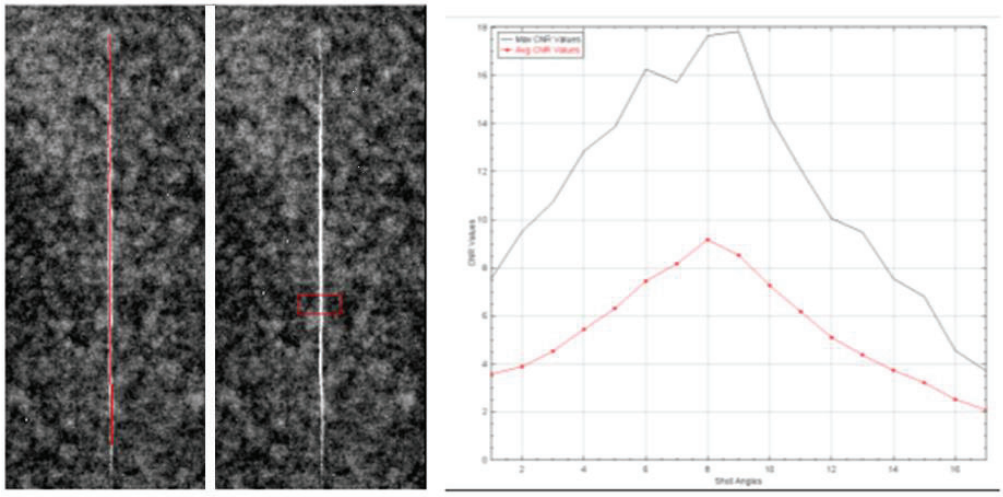

Figure 8.3-1. Points on crack detected for analysis, Location on crack of maximum CNR value, Average and maximum CNR Values for all angles.

9.0 Beam Angle Effects on Radiography Detectability

9.1 Review of Literature and Air Force Guidance on Limits for Radiographic Beam Angle

The primary reference on the effect of incident angle on radiograph detection of cracks is "*Nondestructive Evaluation of Fatigue Cracks"* by C.R. Bishop [1]. This reference is discussed in detail in the next section.

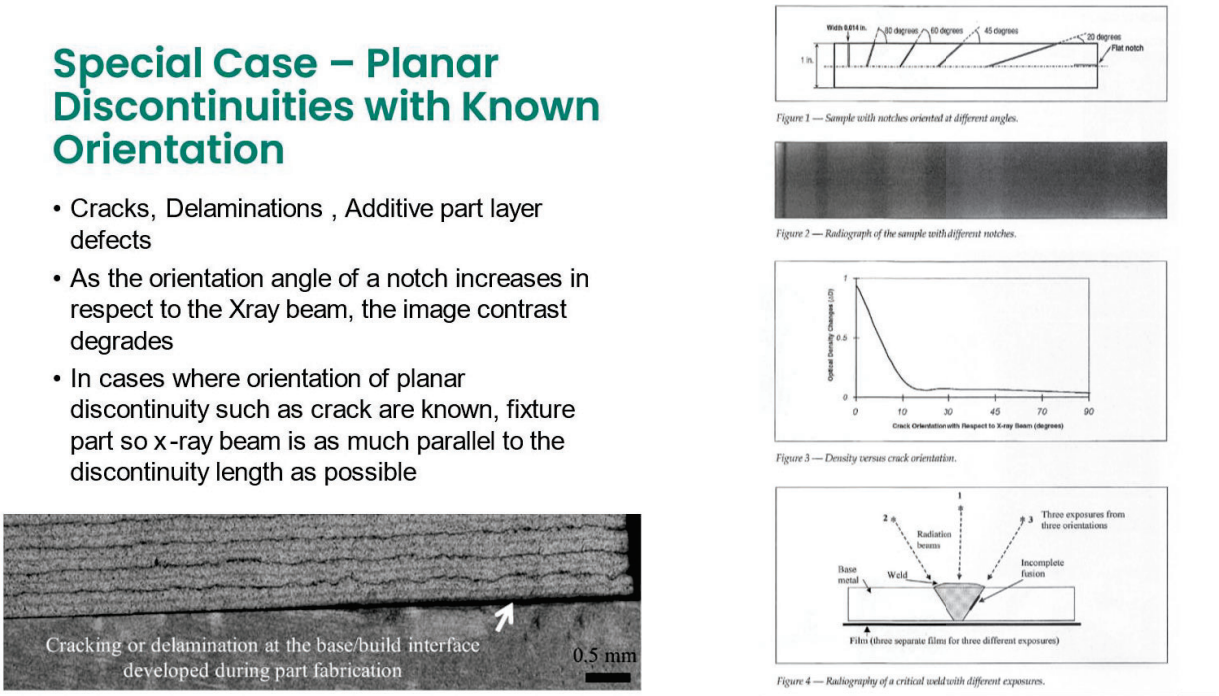

Figure 9.1-1. Planar Discontinuities with Known Orientation

Bishop's report references a paper by Rueschert [9] that discusses the detection of cracks in 3.9 mm corrosion-resistant steel weld of Ti plates. Cracks were induced in the weld, however the method for generating the cracks was not specified in the paper. Based on a figure in the paper, at least 50 relatively closely spaced cracks were induced in the weld region. The number of cracks was assumed to be the largest number of cracks detected by an inspector with an incident angle was 0°. The cracks were relatively shallow, 13% to 29% of the thickness of the weld. Data were acquired at the beam angles (0°, 9°, 15°, 21° , 27°, and 45°). A quadratic spline interpolation yields approximately 7% reduction in the number of cracks detected at 5°. The publication does not attempt to estimate the variation in POD as a function of beam angle.

Air Force guidance for radiographic inspection for cracks states, "Radiography can only be depended on to reveal crack-like discontinuities that are aligned within approximately 7° of the X-ray beam." [10]

These publications support the statement, "The plane of radiation shall be within +/-5° of the assumed crack orientation." in NASA-STD-5009C.

9.2 Analysis of Beam Angle Data in Bishop POD Study

9.2.1 Background on the Bishop POD Study's Estimate of Radiographic Standard NDE

This section examines beam angle effects of radiographic POD based on the Bishop [1] POD study that supported the Orbiter Fracture Control Plan described in King [11]. Standard NDE flaw size for penetrant and radiography, as stated in NASA-STD-5009C, are directly traceable to Bishop's POD study and analysis.

Bishop's POD study included multiple inspectors from three facilities using radiographic, ultrasonic, eddy current, and penetrant NDE methods. It is the earliest reference to estimate the flaw size that a large proportion of inspectors are expected to reliably detect. Flaw S. A comprehensive discussion on Bishop and the POD database is provided in Parker [12], and aspects of the study relevant to exploring beam angle effects on radiographic inspection are discussed in this section.

The Bishop POD study featured 420 fatigue cracks in Al 2219-T87 specimens. The 420 cracks were induced in 164 specimens fabricated by Martin Marietta and General Dynamics Convair. Specimen nominal dimensions were 10.2 cm wide and 4 cm long with nominal thicknesses of 1.5 mm and 5.3 mm, referred to as "thin" and "thick" specimens. Each specimen contained multiple fatigue cracks, with some specimens having fatigue cracks on both sides. All of the flaws in this study were open to the surface, partly through the thickness cracks. Bishop reports that, "The location and occurrence of the flaws were carefully selected to eliminate any pattern effect which may have been detected by the inspectors."

Specimen fabrication details are provided in Rummel [2] and Anderson [3]. All of the cracks were chemically etched at two levels of material removal by the two fabricators. Etching was only required for penetrant inspection; however, a single set of specimens was used for all four NDE methods. Rummel reports that about 75% of Bishop's specimens were chemically etched to remove 0.05 mm of material thickness, while Anderson reports an etching rate and time of exposure that suggest a material removal of about 0.02 mm thickness for the other 25% of the cracks.

No blank (unflawed) specimens were included in this POD study, and therefore the probability of a false call could not be estimated.

There were seven inspectors for radiography from Rockwell, Martin Marietta, and General Dynamics Convair, however, the affiliation of the inspectors is not identified in Bishop's POD database. The inspectors are designated alphabetically as A-G.

Crack length (2c) versus depth (a) of the 420 cracks is shown in Figure 9.2.1-1. The crack aspect ratio (2c/a) ranges from 0.7 to 16.4, with the majority of cracks having an aspect ratio of 1 to 9. Radiographic POD is typically modeled as a function of crack depth-to-thickness ratio (a/t). Figure 9.2.1-2 provides the distribution of a/t for the 1.52 mm and 5.33 mm specimens. There are many shallow cracks (*i.e.*, low a/t) that are weakly informative to modeling radiographic POD. In order to get a 90/95 detection capability of around 0.70t, (crack depth = 70% of specimen thickness), a more uniform distribution is expected. This non-optimized crack size distribution is a result of Bishop's crack set being designed to cover the capability of all four inspection methods that have varying 90/95 crack sizes. Crack opening was not characterized in the Bishop study, and all cracks were implicitly assumed to have the same opening. Variation in

crack opening could influence the POD detection capability of radiography, as discussed in Section 10.2.

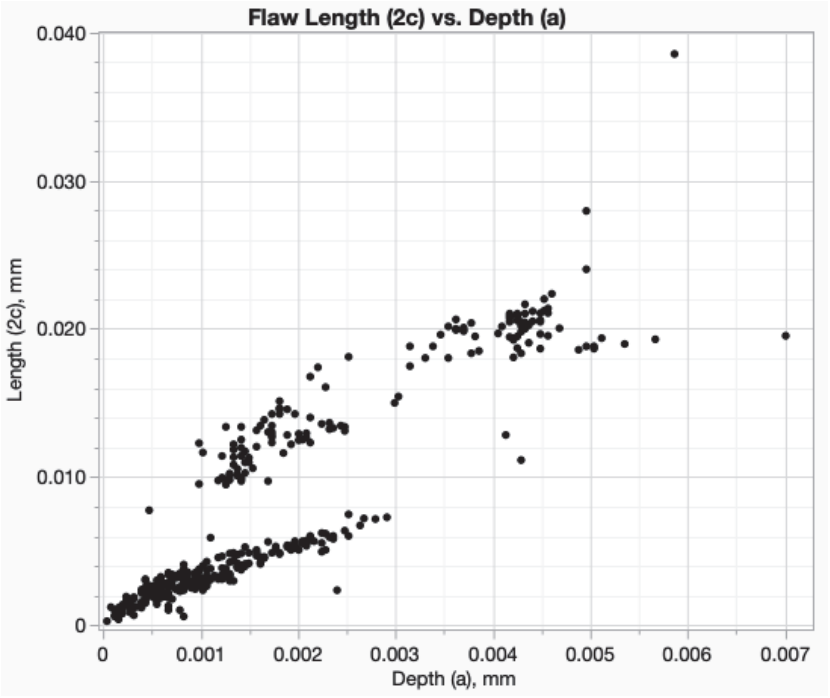

Figure 9.2.1-1. Crack Length versus Depth of the 420 Cracks in the Bishop POD Study

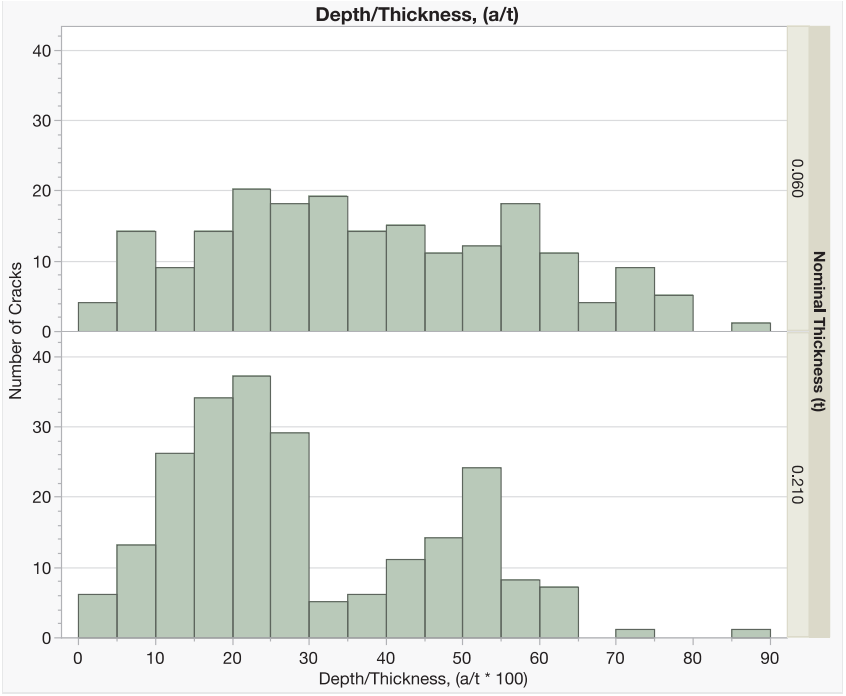

Figure 9.2.1-2. Crack Depth-to-Thickness Ratio (a/t*100) of the 420 Cracks in the Bishop POD Study

Bishop developed the Sorted Group Ascent Method (SGAM) to estimate the flaw size that was intended to provide 90% probability of detection with 95% confidence that was expected to be

demonstrated by 95% of qualified inspectors, known as the 90/95/95 flaw size. Bishop's radiographic Standard NDE flaw size was reported as 0.7t, and it is the traceable source of 0.7t provided in NASA-STD-5009C. Salkowski [13] discusses the motivation for employing the SGAM and provides technical criticisms. Parker [12] describes SGAM in detail and compares it to the NESC's analysis of Bishop's POD data using MIL-HDBK-1823A modeling methodology that provides a Standard NDE radiographic flaw size of 0.83t which is significantly larger 90/95 value than is 0.7t. Individual inspectors in the study demonstrated between 0.59t and 0.79t 90/95 detection capability, with 4 of the 7 inspectors demonstrating greater than 0.7t. It was found that 0.7t provides about 50% inspector coverage (*i.e.*, it's the 90/95/50 flaw size). Therefore, Bishop's SGAM was found to be nonconservative for radiography. When evaluating the POD as a function of beam angle in this section, this discrepancy with NASA-STD-5009C Standard NDE flaw sizes is noted. Therefore, the relative change in detectable flaw size as function of beam angle is the focus on the analysis rather than absolute flaw sizes.

The effect on radiographic POD by chemically etching the cracks is another qualification on the detectable flaw sizes estimated from Bishop's study. Rummel reports with respect to the 0.05 mm etched specimens that "Many of the cracks were visible on close visual inspection after chemical milling." In addition, Rummel indicates that radiographic inspection capability was greatly enhanced by etching. Recent experimental studies and computational modeling of the effects of etching on radiographic images are discussed in Section 10.4.1 of this report. All analyses of the Bishop POD study are qualified as representing detection capability on etched cracks. A comprehensive POD study comparable to Bishop (1973) with unetched cracks was not found.

9.2.2 Beam Angle Description

Bishop's POD data include a column labeled "INCLD ANGLE," and Bishop page A-1 defines the parameter: "INCLD ANGLE – The number represents the angle in degrees between the assumed flaw plane and the direction of the radiation beam during radiographic inspection at Rockwell only."

The flaw angles were assumed to be with respect to the normal to the specimen surface. The included angle was determined in order to investigate the slope of the X-ray sensitivity curve. Cursory analysis indicated that the probability of detection was indeed a function of included angle; however, the data were insufficient to reconcile the response curve completely so that it would approximate a Heaviside function as the other techniques do. Ruescher [9] investigates the effect of included angle more completely.

Regarding "inspections at Rockwell only," as previously noted, the inspector affiliations in Bishop's database were not provided, and the inspectors are anonymously labeled as A-G. Therefore, it is not possible to identify the Rockwell inspectors. "Cursory analysis" may refer to a form of the SGAM, which was rudimentary and found to be nonconservative, as discussed in Parker [12]. The inability to "reconcile the response curve" and potential differences in POD response curves as a function of beam angle was likely limited by these rudimentary statistical analysis methods at the time of the study. Ruescher does not provide analysis of Bishop's POD data.

Bishop further discusses the effect of beam angle that was evaluated during the radiographic technique optimization using the Reference Standard Specimens (*i.e.*, not during the POD study with blinded inspectors). It was found by laterally offsetting the source location relative to a

crack that at angles greater than 6°, a crack with a/t = 0.47 (0.086-inch (2.18 mm) long by 0.029-inch (0.73 mm) deep crack in a 0.062-inch (1.6 mm) thick specimen) was "distorted to such an extent that it could no longer be identified on the radiograph." This finding established the radiographic procedure for the POD study.

It is assumed that the source-to-film distance (SFD) and crack grid location were used to compute the included angle. The SFD was reported to be 24 inches (61 cm). There was a 0.50-inch (1.3 cm) grid specimen overlay provided for the inspectors to report a crack indication. Based on the geometry shown in Figure 9.2.2-1, the angle is computed as the $\tan^{-1}$(grid location from source/SFD), e.g., $\tan^{-1}(0.50/24) = 1.2°$, and the maximum offset of 2.5 inches (6.4 cm) corresponds to $\tan^{-1}(2.5/24) = 5.9°$. Accordingly, 0.50-inch (1.3 cm) grid locations at 24 inches (61 cm) SFD provides the reported discrete levels of included angles of 0°, 1.2°, 2.4°, 3.6°, 4.8°, and 5.9°.

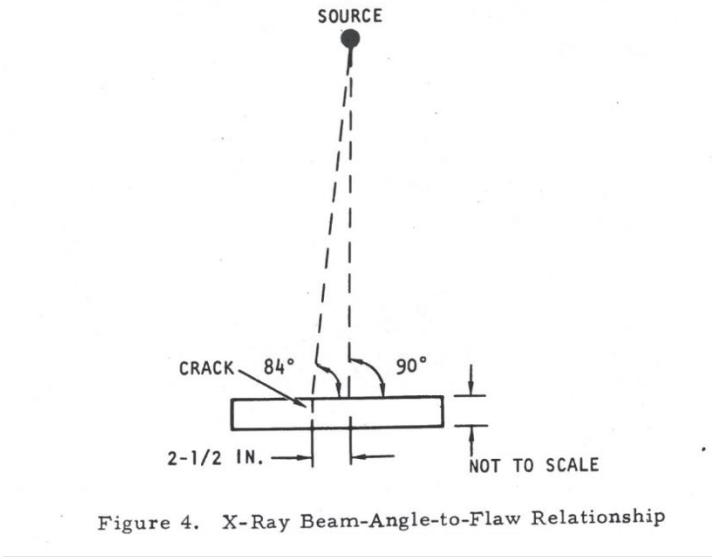

Figure 9.2.2-1. Bishop (1973). X-ray Beam Angle-to-Flaw Relationship.

The radiographic procedure for the POD study reported that it exposed two specimens simultaneously side by side, and two exposures were made for each specimen with the source laterally offset at ±2 inches (5.1 cm) or ±2.5 inches (6.4 cm) from the center-line to maintain less than a 6° beam angle ()see Figure 9.2.2-2).). The different offsets were a result of the different inspection area lengths for the Convair and Martin Marietta specimens. The Convair specimens had an 8-inch-long inspection area, resulting in a ±2-inch (5.1 cm) offset to cover the full area, and the Martin Marietta specimens had a 10-inch-long inspection area resulting in a ±2.5-inch (6.4 cm) offset.

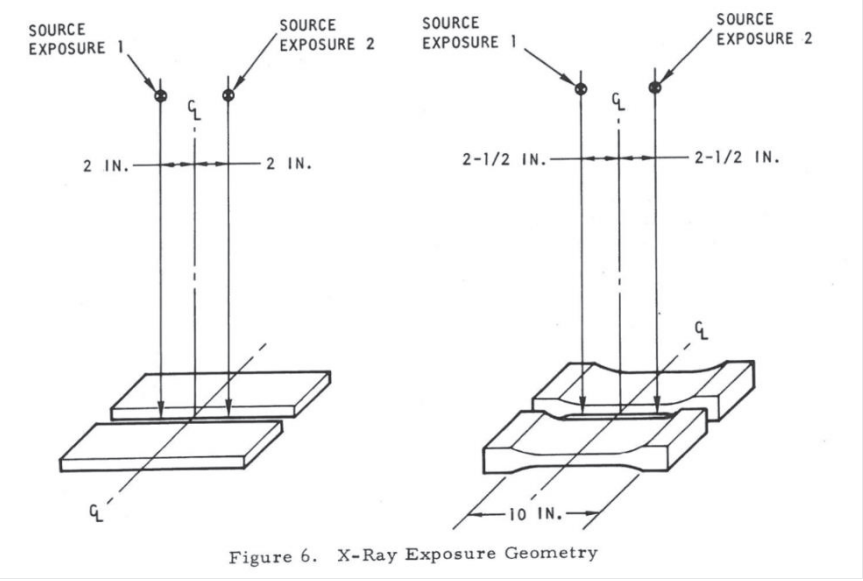

Figure 9.2.2-2. Bishop X-ray Exposure Geometry. Radiographic Procedure for Convair (left side) and Martin Marietta (right side) Specimens.

Table 1 of Bishop provides the key for the crack-naming convention of the specimens and additional details are provided in Appendix A. Bishop's Figure 9.2.2-3 shows the 0.5-inch (1.3 cm) grids that identified the location of a detected crack. From the crack names, locations, and angles given in the Appendix, it is possible to create a map of where the cracks occurred on the grids if they had been detected. There are two grids for the Convair specimens, one for the thin specimens and one for the thick specimens, shown in Figure 9.2.2-3. Marked on the grid is a red horizonal line above which the X-ray source would have been located for the –2.5-inch (6.4 cm) and +2.5-inch (6.4 cm) exposures. The map of crack locations indicates that the offset was 2.5 inches (6.4 cm) for the Convair specimens, which contradicts the 2-inch (5.1 cm) offset shown in Figure 9.2.2-2 from the Bishop report. Subsequent analyses in this report assumes the tabulated locations and angles, supporting the mapping in Figure 9.2.2-3, are correct.

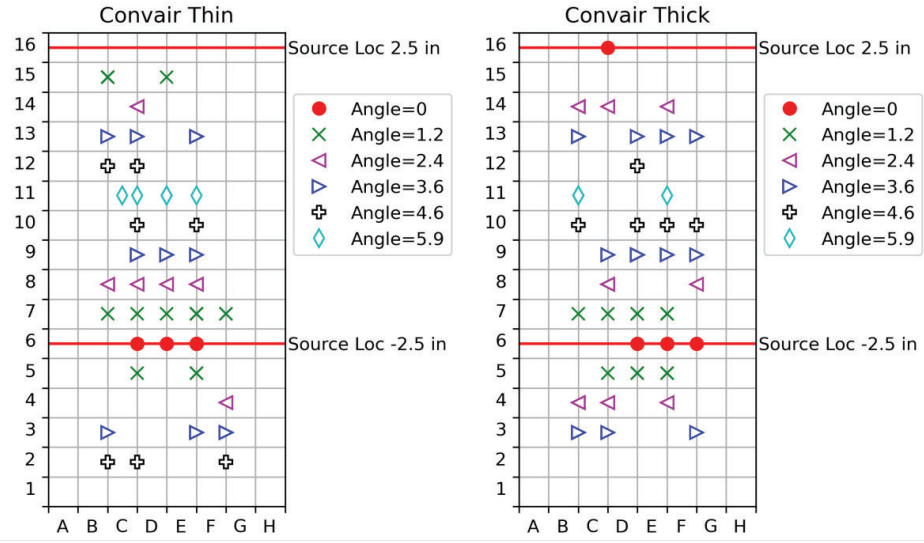

Figure 9.2.2-3. Mapping of the crack locations for Convair thin and thick specimens to grids in Bishop report. Grid line spacings are 0.5 inches (1.3 cm).

There are four grids for the Martin Marietta specimens for sides A and B of the thin and thick specimens. The thin specimen mappings are shown in Figure 9.2.2-4, and the thick specimens are shown in Figure. Marked on the grid is a red horizonal line above which the X-ray source would have been located for the –2.5-inch (6.4 cm) and +2.5-inch (6.4 cm) exposures.

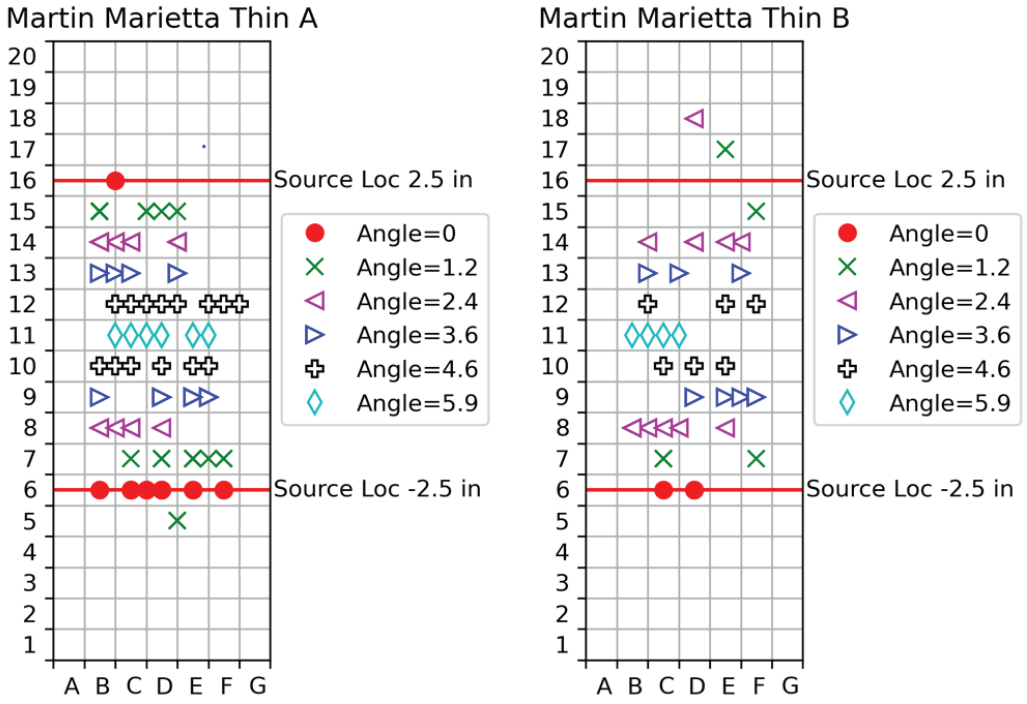

Figure 9.2.2-4. Mapping of the crack locations for Martin Marietta sides A and B of thin specimens to grids in Bishop report. Grid line spacings are 0.5 inches (1.3 cm).

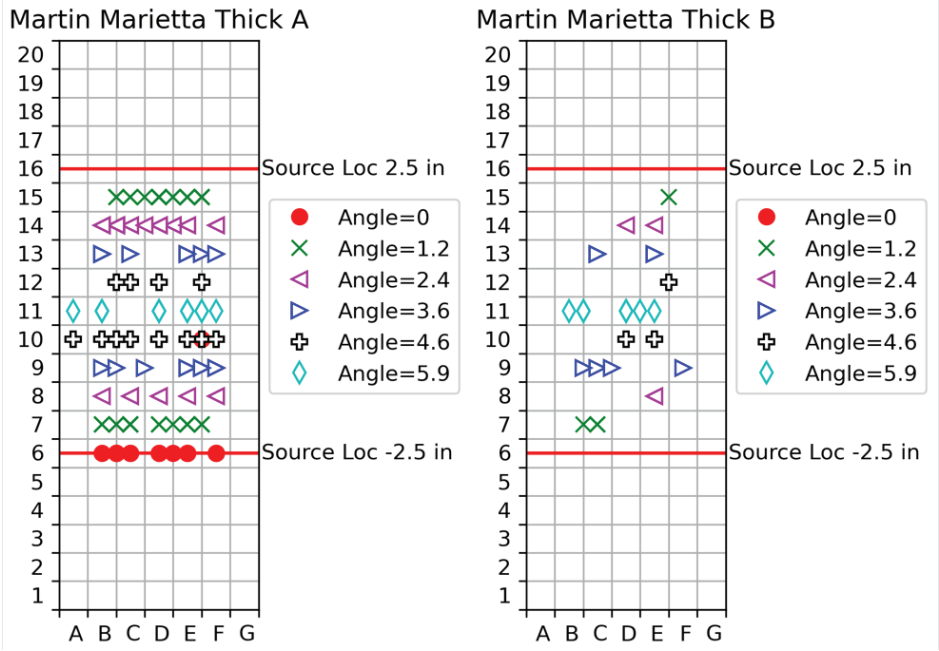

Figure 9.2.2-5. Mapping of the crack locations for Martin Marietta sides A and B of thick specimens to grids in Bishop report. Grid line spacings are 0.5 inches (1.3 cm).

One interesting feature seen in these maps is that cracks detected further than 2.5 inches (6.4 cm) from the source line are not captured in the report. The intent of the study was to only record cracks with incident angles less than 5.9°.

9.2.3 Crack Sizes within each Discrete Angle Grouping

Table 9.2.3-1 provides the number of cracks per angle group.

Table 9.2.3-1. Number of Cracks per Angle Group

Included Angle	N
0.0	44
1.2	88
2.4	86
3.6	80
4.8	75
5.9	47

There are fewer flaws at 0° and 5.9°, and there are less than the minimum recommendation of 60 flaws for a hit/miss analysis in MIL-HDBK-1823A (2009) by angle grouping. However, the quality of the POD models depends on both the number of cracks and their size distribution relative to the NDE method's detection capability. Figure 9.2.3-1 shows the range of a/t by angle grouping with boxplot overlaid. The pinched center of the boxplot indicates the median a/t — the box itself covers 75% of the a/t values — and the whiskers of the boxplot extend to the minimum and maximum a/t. As previously noted for radiographic inspections across all beam angles, an excess of shallow cracks are weakly informative in estimating the 90% POD range, which is assumed to be around 0.7t. For 5.9°, there is a gap in a/t crack sizes between 0.55t and 0.7t and only 2 cracks larger than 0.7t. This poor size distribution at 5.9° deteriorates the ability to model the POD curve in this critical region, which is expected to cover 90% POD.

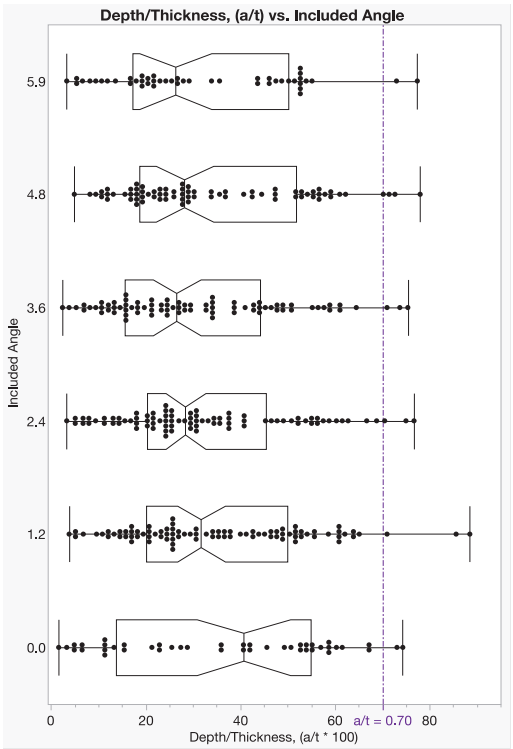

Figure 9.2.3-1. Range of Crack depth/thickness (a/t) by Angle Grouping

9.3 Beam Angle Effect Modeling Rationale

A modeling rationale to leverage the Bishop POD study was developed to answer the following primary questions:

1. If increasing beam angle shows a deterioration in radiographic POD over the angle range in this study (*i.e.*, less than 5.9°), at what angle is there a discernable onset of POD decline?
2. Does Bishop's POD study support NASA-STD-5009C's requirement [NER 29] in Section 4.1.4.4.3 (c) stated as, "The local X-ray axis of the radiation beam **shall** be within ±5° of the assumed crack plane orientation"? This requirement restricts the usage of Standard NDE radiographic flaw sizes to inspections that have beam angles within ±5°.

It is acknowledged that the Bishop POD study was not originally designed to answer these questions related to beam angle, and it suffers from limitations cited here and in Parker [12]. However, the following analysis approach and supporting rationale were developed to maximize the value of Bishop's unique POD study under its constraints:

POD modeling by angle combines all inspector calls. Modeling by inspector, as done for Standard NDE, is not performed. *Supporting rationale:* (1) Even though the "included angle" was reported to apply to Rockwell inspectors only, those inspectors cannot be identified; (2) There are a limited number of cracks and non-optimized crack size distribution in each angle grouping, and further dividing those groupings for each inspector would reduce the available data for POD modeling; (3) Combining all inspectors averages the beam angle effect across the sample inspectors, and it can be inferred to represent the population of qualified inspectors. As a cautionary note, combining inspectors increases the apparent sample size and would artificially reduce the statistical uncertainty, since it does not increase the sample size of unique cracks.

POD flaw size a90 (90%) is used to compare angle effects, not the a90/95 flaw size. *Supporting rationale:* (1) Since sample size is increased by combining all inspector calls, the 95% confidence interval would be artificially reduced; (2) There are unequal sample sizes within each angle group (*i.e.*, there are varying numbers of cracks at each of the discrete angles). The unequal sample sizes affects the 95% confidence interval width. Detecting a difference and/or trend as a function of angle would be confounded with varying confidence interval widths. Based on these reasons, confidence bounds (*i.e.*, a90/95) are not reported.

POD modeling is performed by combining both specimen thicknesses for each thickness grouping. *Supporting rationale:* (1) Bishop's Standard NDE flaw sizes were based on the combination of both specimen thicknesses; (2) While there are sample size benefits in combining specimen thickness, the beam angle effect was conjectured to be worse for thin specimens based on computational modeling, so it is evaluated separately too.

POD modeling combines all crack aspect ratios. *Supporting rationale:* (1) Bishop's POD results for all NDE methods were over all aspect ratios (*i.e.*, POD as a function of aspect ratio was not reported by Bishop); (2) While the Orbiter Fracture Control Plan and NASA-STD-5009C report POD as a function of aspect ratio, Parker concluded that Bishop's POD crack size design does adequately support POD modeling as a function of aspect ratio.

The POD modeling was consistent with MIL-HDBK-1823A. Generalized linear model regression with a probit link function was used. There was no transformation applied to the depth/thickness (a/t) flaw size in the modeling.

No individual inspector responses or cracks were removed from Bishop's POD dataset. Regardless of whether specific calls may appear anomalous, e.g., a hit at a low value of a/t, without first-hand knowledge of the study signifies that a consistent rationale could not be developed to exclude individual inspections or specimens.

Overall, the radiographic inspection modeling is consistent with the NESC's evaluation of Bishop's POD dataset presented in Parker *et al.* (2022), except for combining all of the inspector calls. As a technical note, a generalized linear mixed model (GLMM) could have been used with inspectors considered as random effects. This technique is discussed in Appendix D of Parker. GLMMs are not discussed in MIL-HDBK-1823A or supported by the handbook's companion software, and therefore, are not common in practice. While this approach may be considered more statistically correct, the additional complexity was considered unwarranted under the cited limitations of this POD study.

9.3.1 Beam Angle Effect Modeling Results

Figure 9.3.1-1 shows the results of modeling POD as a function of beam angle when combining all specimen thickness (*i.e.*, both "thin" and "thick" specimens). The y-axis is the 90% POD (a90) flaw size, not the a90/95. A visual reference line is provided at 0.70t, which is the NASA-STD-5009C Standard NDE flaw size. As a caution, the a90 flaw sizes on the y-axis are not directly comparable to the Standard NDE flaw size, since they do not include estimates of statistical uncertainty nor inspector-to-inspector variability. e.g., The detection capability appears to deteriorate above 2.4° as noted by the increasing 90% a/t value above this angle. The a90 estimate at the maximum angle of 5.9° appears to indicate an increase in detection capability, however, this is expected to be a result of an insufficient crack distribution to fully support POD modeling near 90% POD at this angle.

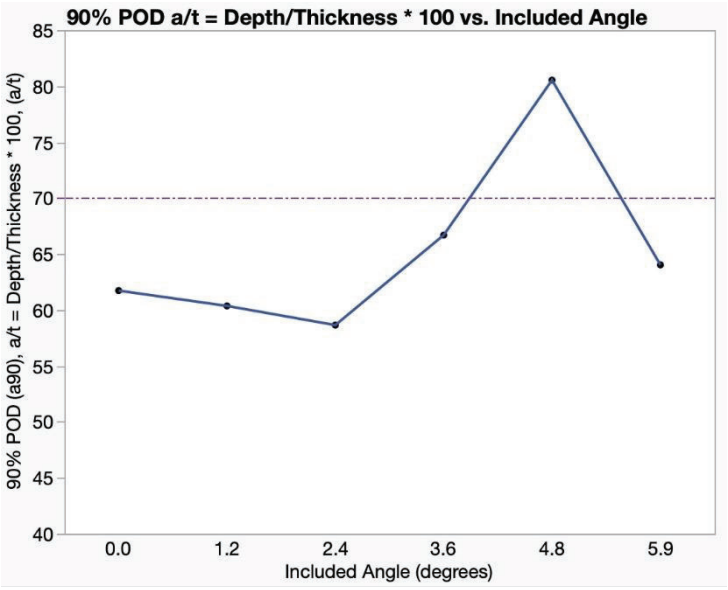

Figure 9.3.1-1. 90% Detectable Flaw Size (a90) versus Angle when Combining All Specimen Thicknesses.

Figure 9.3.1-2 shows the results of modeling POD as a function of beam angle for "thin" 1.52 mm specimens only. In this plot, a similar onset of the decrease in detection capability occurs after 2.4°. While the a90 values are higher for these thin-only specimens, compared to combining the specimen thicknesses, the relative change in detection capability is consistent. Once again, there is an apparent increase in detection capability at 5.9°, and it is also considered specious, even though the crack size distribution is somewhat better for thin specimens as shown in Figure 9.2.1-2.

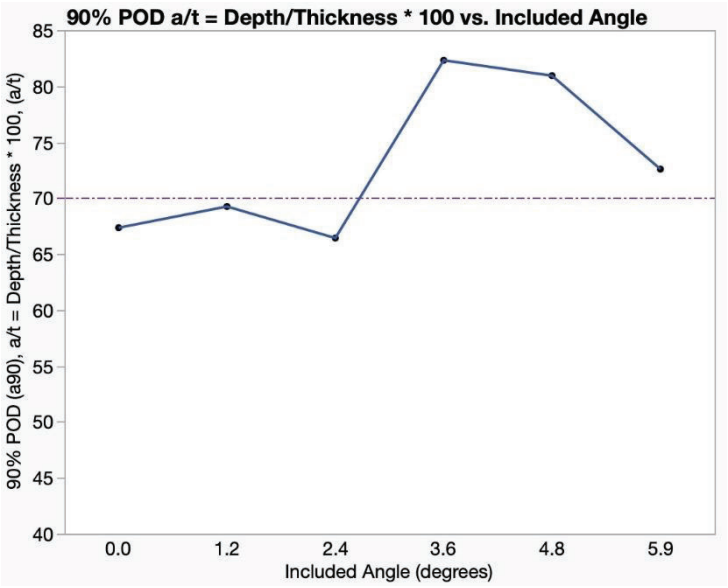

Figure 9.3.1-2. 90% Detectable Flaw Size (a90) versus Angle for Thin 1.52-mm (0.060-inch) Specimens

Figure 9.3.1-3 shows the results of modeling POD as a function of beam angle grouping for "thick" 5.33 mm specimens only. In this plot, the onset of the decrease in detection capability occurs at 3.6°, which is higher than the combined thickness analysis and the thin-only analysis. As previously mentioned, computational modeling suggested that the effect of beam angle would be worse on thin specimens, and this is consistent with a later onset of capability deterioration. While the a90 values are lower compared to thin-only models, the relative change in detection capability is consistent. The apparent increase in detection capability at 5.9° continues to be evident, and it is considered specious, especially for the crack size distribution of thick specimens shown in Figure 9.2.1-2.

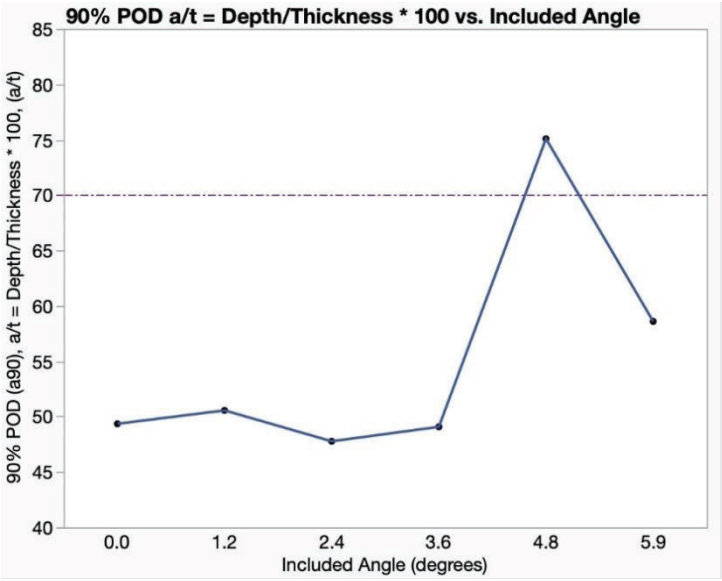

Figure 9.3.1-3. 90% Detectable Flaw Size (a90) versus Angle for Thick 5.33-mm (0.210-inch) Specimens

In summary, the POD modeling that combines both specimen thicknesses, shown in Figure 9.3.1-1, is considered the best representation of Standard NDE, since specimen thicknesses were combined in the Standard NDE flaw size in NASA-STD-5009C based on Bishop's data. It is recommended that the 5.9° a90 predictions be visually omitted based on the poorly supported statistical models at this angle. Furthermore, an increase in detection capability at the highest angle is inconsistent with the physics-based expectations and computational modeling discussed in Section 10.5. Therefore, it is concluded from Figure 9.3.1-1 that detection capability is deteriorated with increasing beam angle, and the deterioration is evident at angles greater than 2.4°.

Evaluating NASA-STD-5009C's requirement of beam angle within ±5° is challenging since Bishop's POD data do not support a Standard NDE flaw size estimate at each angle. Therefore, the data from this POD study are unable to support or refute NASA-STD-5009C's requirement. However, qualitatively, since inspectors were combined in this analysis, the a90 could be thought of as the average inspector capability, analogous to 50% coverage of the population of qualified inspectors, (*i.e.*, a90/95/50), which 0.7t in NASA-STD-5009C was found to represent and was not revised based on Parker findings due to an argument of historical performance sufficiency. So if the a90 flaw size at each angle is considered representative of the average a90/95 flaw size of individual inspectors from a hypothetical well-designed Standard NDE POD study with large sample sizes of inspectors and cracks, then evaluating when the a90 POD crosses the 0.7t threshold is plausible. Therefore, based on Figure 9.3.1-1 and using 0.7t as a threshold suggests that an angle between 3.6° and 4.8° is acceptable and this is near NASA-STD-5009C's requirement of 5°. The Bishop POD does not support increasing the beam angle requirement to greater than 5°.

9.3.2 Conclusion Beam Angle Effects on Radiography POD based Standard NDE POD Study

An analysis of the Bishop POD study was performed to investigate the effect of beam angle on radiographic inspection POD capability. It is acknowledged that there are numerous limitations

on broad application of these results due to the exclusive use of aluminum specimens and on a limited range of specimen thickness and crack mouth openings. Bishop's POD study contained a number of limitations: (1) it was not designed to evaluate beam angle; (2) it had a poor crack size distribution for radiographic POD modeling of 90% POD; (3) it used chemically etched cracks that are expected to enhance detectability; (4) it did not have the ability to identify the specific radiographic inspectors from Rockwell that are correlated with included angle; and (5) it used film radiography instead of current digital techniques. Nevertheless, even with all of these limitations, the Bishop POD study is the only suitable dataset available to evaluate the beam angle effects on POD for radiographic inspections. It is recommended that these POD analyses are considered complementary to the image analyses of other experimental studies and computational modeling results, both of which are expected to be correlated with POD discussed in this report. (See findings F-1 and F-2)

9.4 Experimental Measurement of Variation of Crack Response with Angle

Radiographic images were acquired with a single specimen placed between the source and detector. The stage was rotated from -10° up to 30° for an assessment of how the crack detectability changes as a function of the angle between the X-ray beam and the specimen surface normal. The large rotations were to attempt to measure the gap width of the crack along the whole depth of the crack.

9.4.1 CNR as a Function of Incident Angle for lightly etched (AL7) and heavily etched (AL8) cracked specimens

The specimen AL7 has the largest CNR, with the crack depth estimated to be 99% of the thickness. For both the CR and DR radiographs, the crack indication was visible for beam angles of -10° to 10° between the X-ray beam and the specimen surface normal. The DR X-ray images of the crack indication acquired after the specimen had been lightly etched are shown in Figure 9.4.1-1. In these images, the crack indication is visible through the full range of 10° to -10°.

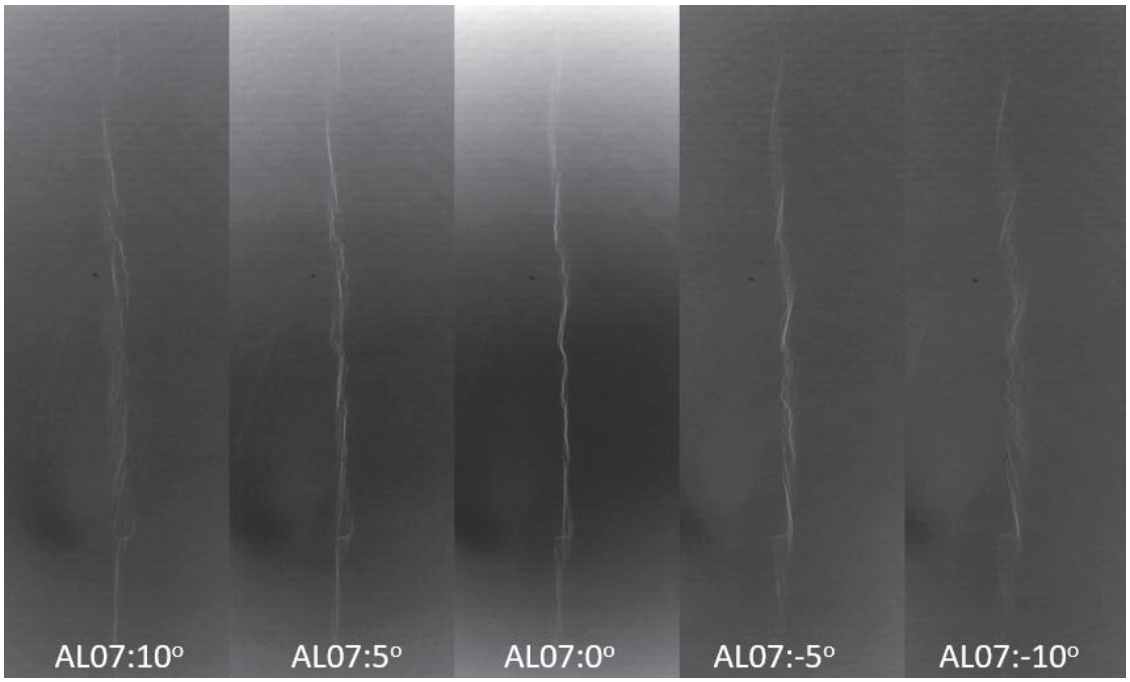

Figure 9.4.1-1. AL7 DR Images at angles +10, +5, 0, -5, -10 angles of incidence.

The IQI normalized, background subtraction DR images are seen in Figure . The background subtraction improves visualization of the decrease in the amplitude and increase in width of the crack indication as the absolute value of the beam angle increases. It is also seen in the images of each angle that the indication amplitude increases towards the center of the crack (vertically) and decreases towards the ends of the crack, as would be expected if the depth of the crack is largest at the center.

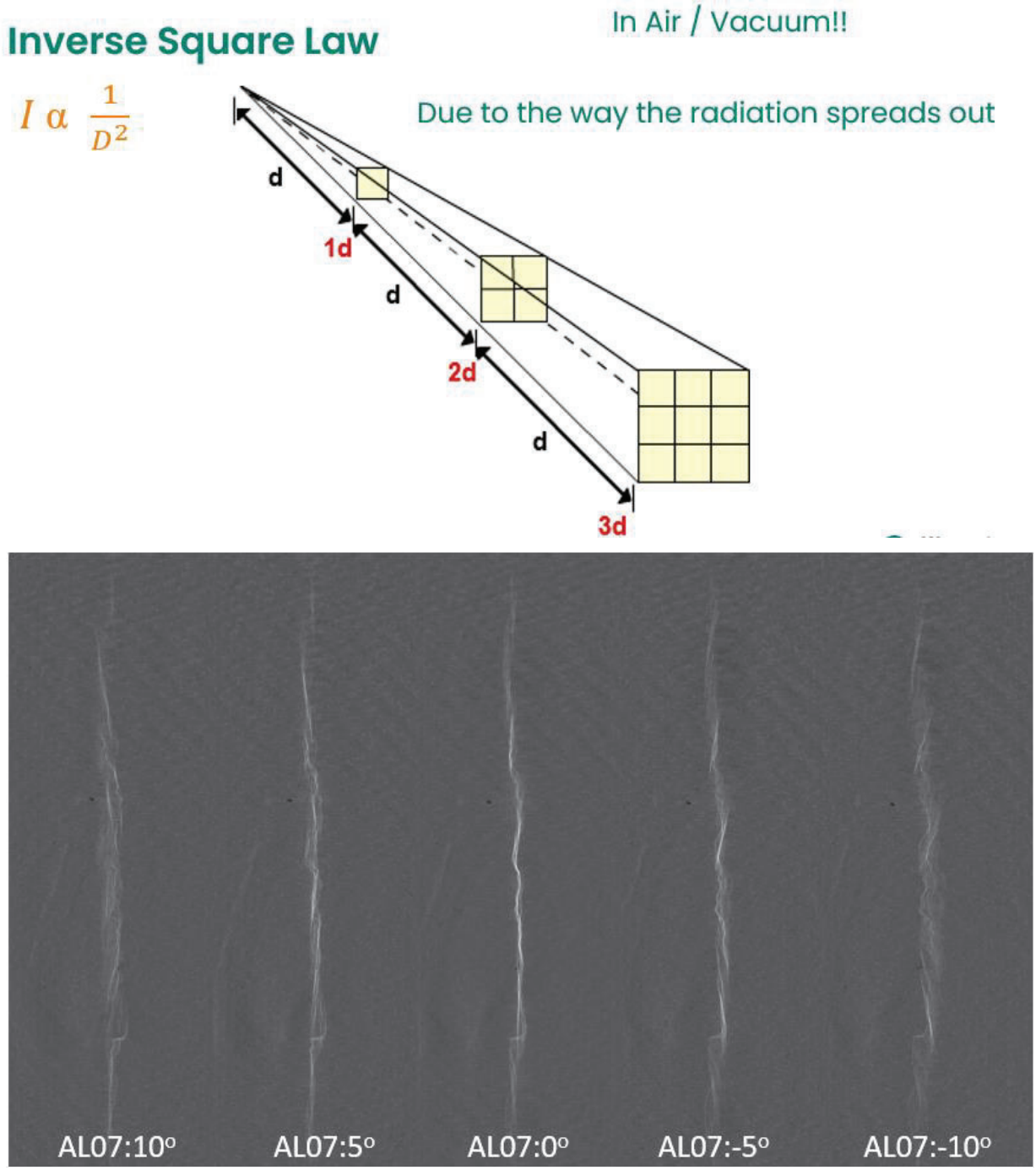

Figure 9.4.1-2. IQI normalized AL7 DR with background subtraction applied at angles +10, +5, 0, -5, -10 angles of incidence.

Radiographs were acquired for AL8 after the heavy etch. The IQI normalized, post background subtraction images are shown in Figure 9.4.1-3. As mentioned in Section 7.1.2, the heavy etch this procedure was intended to approximate the heavy etch performed by Martin Marietta. There are two immediate differences between these images and those for AL7. First, the indication amplitudes are approximately the same for the whole length of the crack. This will be discussed again in Section 10.7. The second difference is that the indication amplitude does not change significantly as a function of angle.

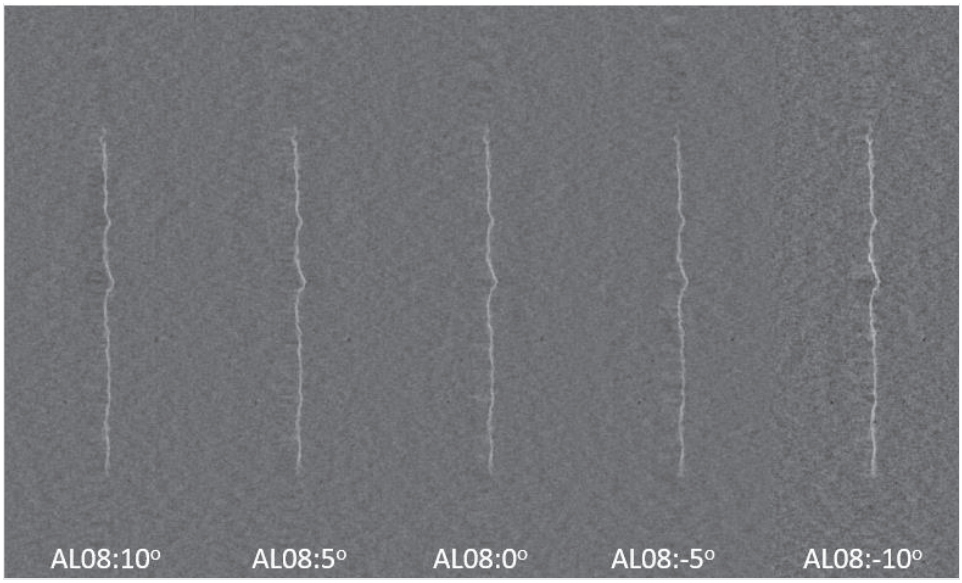

Figure 9.4.1-3. IQI normalized AL8 DR for five Beam Angles with background subtraction.

Both differences become apparent when comparing the IQI normalized CNR as a function of angle, given in Table 9.4.1-1. For AL8, the largest CNR decrease as a function of angle is only 18%, while for AL7, the largest decrease is 76%. This indicates this degree of etching significantly increases the detectability of cracks when the beam is off angle. The ratio of max CNR to average CNR is on average 1.17 for AL8, while the same ratio is 1.79 for AL7, which shows that the indication amplitude as a function of location along the crack is more constant for AL8 than AL7.

Table 9.4.1-1. Comparison of CNR for AL7 and AL8 as a function of angle.

Angle	Average AL7 CNR	AL7 Max CNR	Average AL8 CNR	AL8 Max CNR
-10	5.57	15.91	5.34	6.79
-8	7.17	17.63	5.59	6.27
-6	9.15	19.09	5.46	6.77
-5	10.60	21.18	5.58	6.90
-4	12.12	24.73	5.75	7.23
-3	14.78	28.31	6.10	7.50
-2	17.40	29.83	6.21	6.97
-1	18.62	25.48	6.19	7.04
0	23.21	33.72	6.28	7.49
1	17.51	24.35	6.52	7.78
2	16.60	29.17	6.40	7.25
3	16.07	30.70	6.48	7.24
4	15.76	28.46	6.31	7.22

Angle	Average AL7 CNR	AL7 Max CNR	Average AL8 CNR	AL8 Max CNR
5	13.67	20.25	5.93	7.06
6	11.85	15.23	5.80	6.64
8	9.48	13.29	5.57	6.34
10	7.23	11.26	5.62	6.26

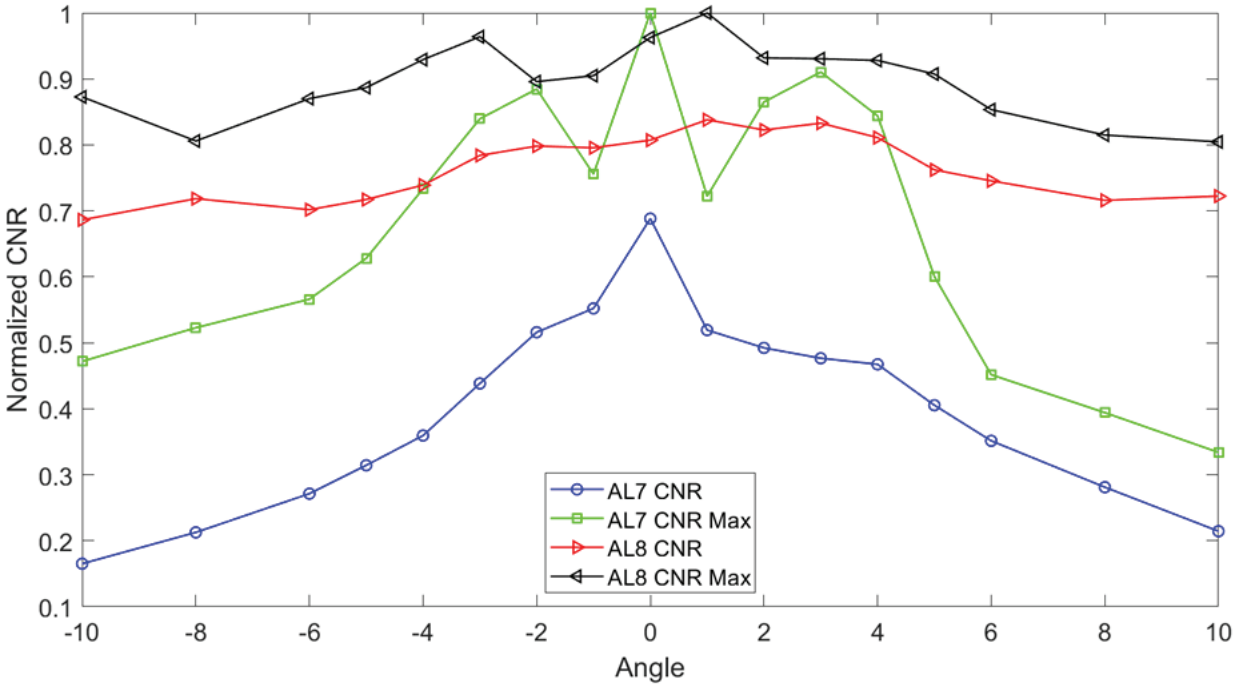

Figure 9.4.1-4. Comparison of the angular dependence of CNR of AL7 and AL8

The difference in angular dependence is visible if the CNRs for each specimen are normalized to the maximum CNR of the specimen and then plotted as shown in Figure 9.4.1-4.. The normalized CNRs for AL8 are shown to be relatively constant as a function of angle, while normalized CNRs for AL7 show the significant reduction as the absolute value of the beam angle increase. Therefore, based on this trend it is likely that some of the etched cracks in the Bishop POD study supplied by Martin Marietta would have been more detectable at beam angles greater than zero than equivalent nonetched cracks at the same beam angles.

9.4.2 CNR as a Function of Incident Angle for AL1 cracked specimen

An example of the representative radiograms of the crack in sample AL1 relative to the X-ray beam can be seen in Figure 9.4.2-1. DRs were taken at angles relative to the beam at intervals of 10°, 8°, 6°, 5°, 4°, 3°, 2°, 1°, 0°, -1°, -2°, -3°, -4°, -5°, -6°, -8° and -10°. As the relative angle of the sample to the beam increases, the relative sharpness and visibility of the crack to X-ray decreases, as expected. There does not appear to be any relative change in the background noise through subsequent measurements. The main sources of background noise for DR inspections are electronic noise in the detector panel and material X-Ray beam scattering.

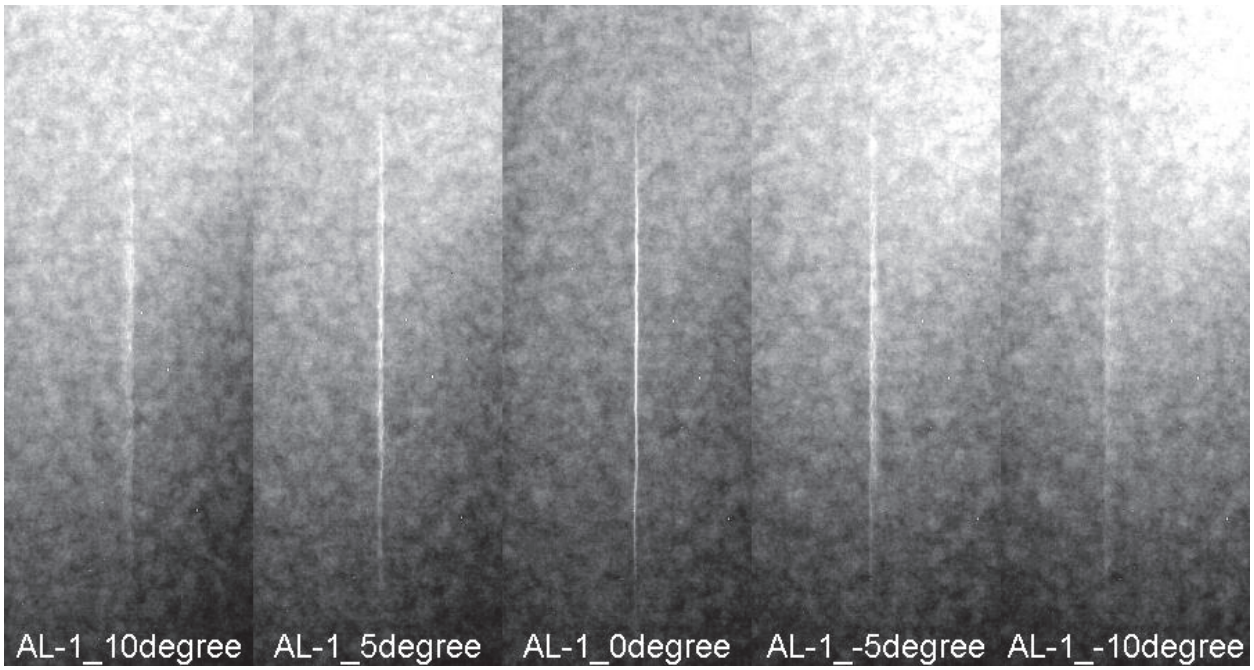

Figure 9.4.2-1. Specimen AL 1 radiograph indications with background subtraction applied for five beam angles.

As done with the previous specimens, for each of the respective radiograms, the CNR and max CNR values can be calculated to characterize the response during X-ray inspection. These values for all the relative angles are listed Table 99.4.2-1. Additionally, it was noted if the crack was visible to the inspectors reviewing the image.

Table 9.4.2-1. AL1 Digital Radiography Contrast to Noise as Function of Angle

Angle	Maximum CNR	Average CNR	Crack Visible
10	8.32	4.38	yes
8	8.79	4.88	yes
6	10.11	5.50	yes
5	12.60	6.43	yes
4	14.60	7.51	yes
3	16.30	9.04	yes
2	15.38	10.10	yes
1	17.74	11.17	yes
0	17.58	10.39	yes
-1	15.15	8.80	yes
-2	12.42	7.45	yes
-3	10.49	6.10	yes
-4	8.54	5.01	yes
-5	7.07	4.31	yes
-6	6.38	3.74	yes
-8	4.91	2.79	yes
-10	3.92	2.07	yes

A normalized (to maximum CNR) CNR value is valuable in determining the loss of signal relative to the incident angle of the X-ray beam. This was again calculated from the data in Table

9.4.2-1.determined. These normalized values can be plotted relative to the angle of the sample to the beam to create a profile of the loss of single, shown in Figure 9.4.2-2.

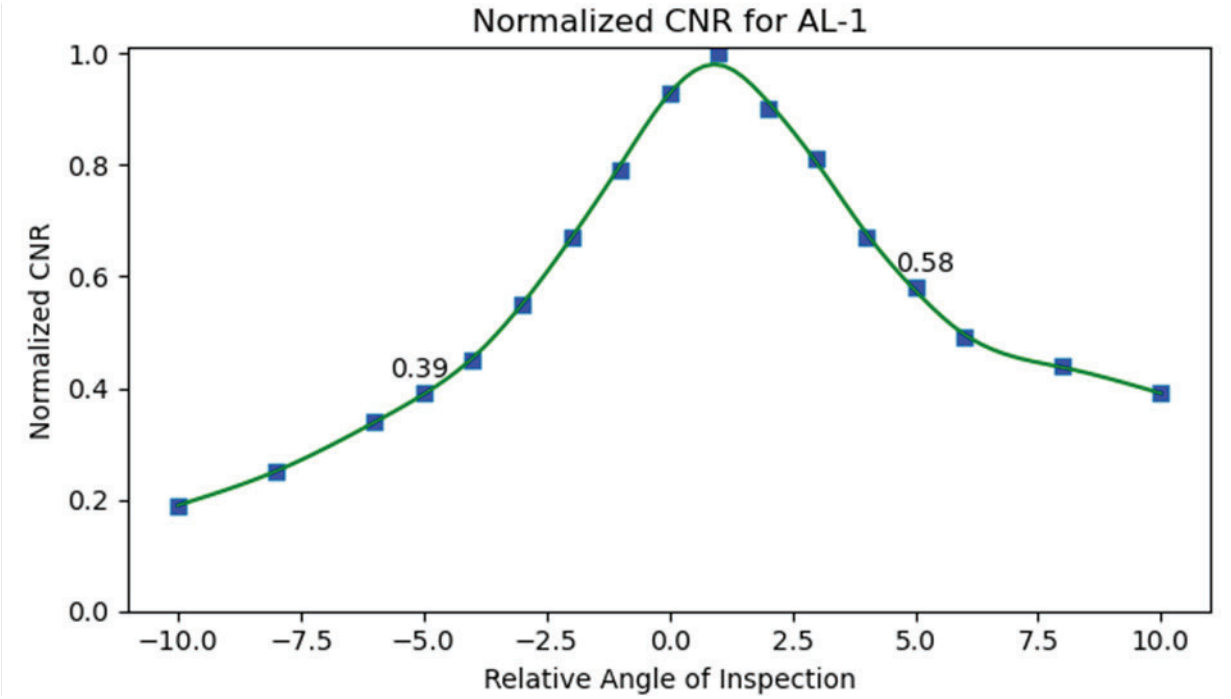

Figure 9.4.2-2. Normalized CNR in specimen AL-1 vs Angle of inspection relative to X-ray beam.

For sample AL1, the maximum response did not occur at the zero angle but at the 1° angle. NASA-STD 5009 also states that angle limit of +/-5° is acceptable for inspection, so these points have been labeled specifically. In the case of sample AL1 at the -5° and +5° points there is an approximate loss of CNR due to loss of signal of 39% and 58%, respectively.

9.4.3 Summarizing CNR as a Function of Incident Angle for all cracked specimens

Similar calculations can be performed for all the samples tested and averaged together to produce an average representation of the expected single loss relative to the incident angle of the beam. These results are summarized in Table 9.4.2-2 and plotted in Figure 9.4.2-3.

Table 9.4.2-2. Summary of the normalized response relative to angle of inspection.

Angle	AL1	AL7	AL8	AL9	AL11	AL36	AL37	C7	C9	C13	Average Normalized Signal
10	0.39	0.41	0.91	0.69	0.46	0.78	0.44	0.27	0.36	0.20	0.49
8	0.44	0.48	0.88	0.80	0.56	0.79	0.50	0.33	0.45	0.25	0.55
6	0.49	0.58	0.88	0.79	0.70	0.81	0.62	0.41	0.51	0.34	0.61
5	0.58	0.62	0.93	0.85	0.77	0.93	0.72	0.48	0.60	0.40	0.69
4	0.67	0.68	0.95	0.90	0.85	0.98	0.84	0.51	0.67	0.52	0.76
3	0.81	0.73	0.97	0.93	0.86	0.94	0.93	0.62	0.76	0.71	0.83
2	0.90	0.76	0.99	0.90	0.85	1.00	1.00	0.66	0.81	0.93	0.88
1	1.00	0.79	0.97	0.98	0.88	0.98	1.00	0.78	0.99	1.00	0.94
0	0.93	1.00	1.00	1.00	0.97	0.93	0.93	1.00	1.00	0.86	0.96
-1	0.79	0.80	0.97	0.94	1.00	0.82	0.78	0.95	0.93	0.66	0.86
-2	0.67	0.75	0.96	0.83	0.99	0.77	0.68	0.91	0.91	0.50	0.80

Angle	AL1	AL7	AL8	AL9	AL11	AL36	AL37	C7	C9	C13	Average Normalized Signal
-3	0.55	0.66	0.99	0.78	0.90	0.67	0.58	0.75	0.77	0.40	0.71
-4	0.45	0.59	0.99	0.79	0.80	0.62	0.53	0.62	0.79	0.33	0.65
-5	0.39	0.54	0.95	0.76	0.70	0.53	0.51	0.50	0.75	0.28	0.59
-6	0.34	0.48	0.97	0.69	0.61	0.50	0.50	0.43	0.62	0.24	0.54
-8	0.25	0.40	0.94	0.72	0.55	0.48	0.46	0.34	0.63	0.19	0.49
-10	0.19	0.33	0.91	0.65	0.51	0.47	0.46	0.28	0.52	0.15	0.45

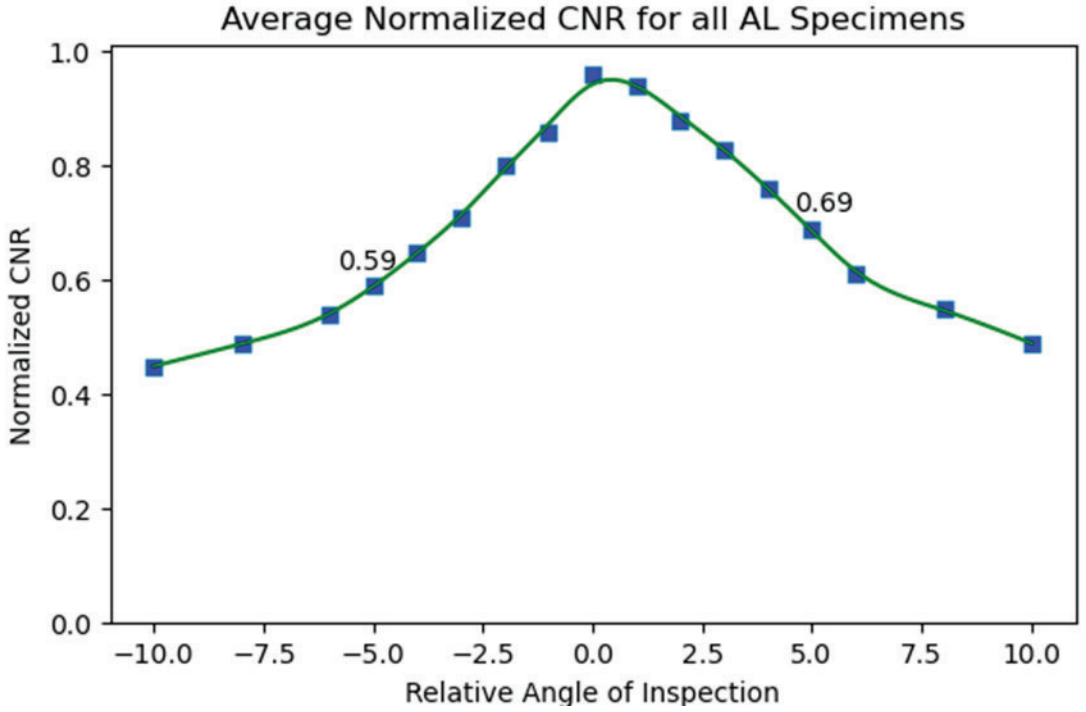

Figure 9.4.2-3. Average normalized CNR loss relative to angle for single wall inspection.

For half of the samples, the maximum average normalized response did not occur at the 0° angle. There are several reasons that this could occur, but it is most likely due to misalignment of the sample during testing, or the crack may not have grown perpendicular to the surface. This results in the normalized response at the +5° mark and -5° mark being 41% signal loss and 31% signal loss, respectively.

A simple shifting within each sample's response column so that the maximum normalized response occurs at the same position (0° beam angle) can be seen in Table 9.4.2-3 and Figure 9.4.2-4. The shifted data then produces the expected symmetry.

Table 9.4.2-3. Realigned summary of the normalized response relative to angle of inspection.

Angle	AL1		AL7	AL8	AL9	AL11	AL36	AL37	C7	C9	C13	Average Normalized Signal
10			0.41	0.91	0.69	0.56			0.27	0.36		0.53
8	0.39		0.48	0.88	0.80	0.70			0.33	0.45	0.19	0.53
6	0.44		0.58	0.87	0.79	0.77	0.78	0.44	0.41	0.51	0.25	0.58

Angle	AL1		AL7	AL8	AL9	AL11	AL36	AL37	C7	C9	C13	Average Normalized Signal
5	0.49		0.62	0.92	0.85	0.85	0.79	0.50	0.48	0.60	0.34	0.64
4	0.58		0.68	0.95	0.90	0.86	0.81	0.62	0.51	0.67	0.40	0.58
3	0.67		0.73	0.97	0.93	0.85	0.93	0.72	0.62	0.76	0.52	0.77
2	0.81		0.76	0.99	0.90	0.88	0.98	0.84	0.66	0.81	0.71	0.83
1	0.90		0.79	0.97	0.98	0.97	0.94	0.93	0.78	0.99	0.93	0.92
0	1.00		1.00	1.00	1.00	1.00	1.00	1.00	1.00	1.00	1.00	1.00
-1	0.93		0.80	0.97	0.94	0.99	0.98	0.99	0.95	0.93	0.86	0.93
-2	0.79		0.75	0.96	0.83	0.90	0.93	0.93	0.91	0.91	0.66	0.86
-3	0.67		0.66	0.99	0.78	0.80	0.82	0.78	0.75	0.77	0.50	0.75
-4	0.55		0.59	0.99	0.79	0.70	0.77	0.68	0.62	0.79	0.40	0.69
-5	0.45		0.54	0.95	0.76	0.61	0.67	0.58	0.50	0.75	0.33	0.61
-6	0.39		0.48	0.97	0.69	0.55	0.62	0.53	0.43	0.62	0.28	0.56
-8	0.33		0.40	0.94	0.72	0.51	0.53	0.51	0.34	0.63	0.24	0.51
-10	0.25		0.33	0.91	0.65	0.50	0.50	0.27	0.52	0.19	0.46	0.46

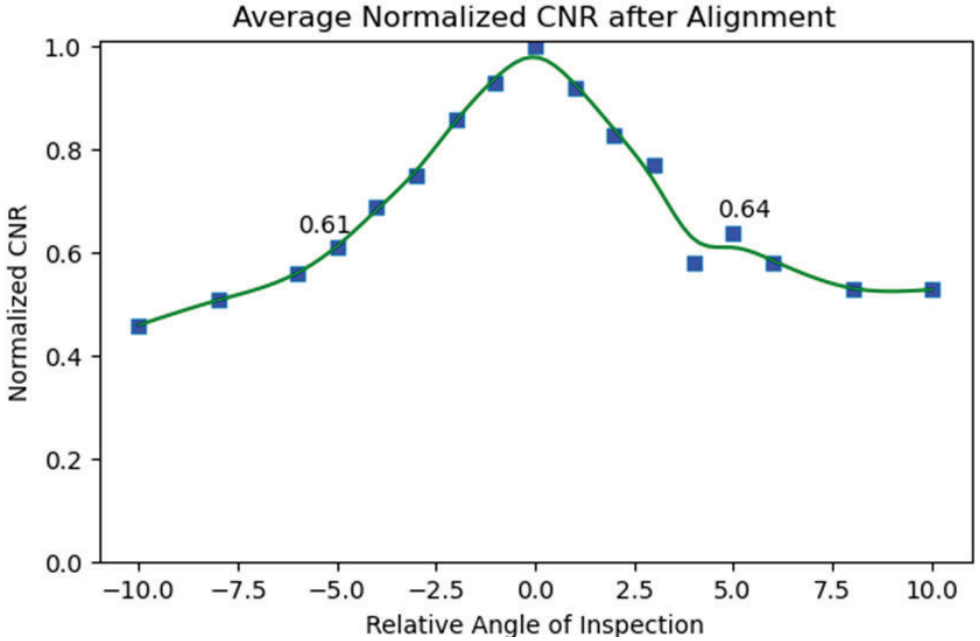

Figure 9.4.2-4. Realigned average normalized signal loss relative to angle for single wall inspection.

After realignment, a plot of the maximum normalized response shows a signal loss of 39% and 36%.

9.4.4 Summary Beam Angle Effects on Radiographic Detectability

Evaluating NASA-STD-5009C's requirement of beam angle within ±5° is challenging since Bishop's POD data do not support a Standard NDE flaw size estimate at each angle. Therefore, the Bishop POD study is unable to support or refute NASA-STD-5009C's requirement. For off-beam angles in Bishop's POD data, the etching performed before the inspection likely increased the detectability of cracks at beam angles greater than zero. Measurements indicate there is a decrease of approximately 40% in the CNR as the angle beam angle increases from 0° to 5°. While there is not a quantitative relationship between this decrease in CNR and the reduction of

POD as a function of angle, a 40% reduction in CNR will likely not significantly impact crack detectability (see Figure 9.4.2-1). With regard to the bi-nominal response required for POD no cracks were missed with the +/- 5° window. Therefore, the expectation is that the POD for a beam angle of 5° is not significantly different from that for 0°, which supports the NASA-STD-5009C's requirement. (See F-3)

10.0 Impact of Etching on Radiographic Crack Detection

This section examines the effect of etching on the detectability of cracks by radiographic inspection. Of primary concern is the effect etching might have had on the results of the Bishop POD study discussed in detail in Section 9.2. Radiographic inspections were performed before and after etching by the specimen providers Convair Aerospace and Martin Marietta, however, Rockwell's final POD assessment of the reliability of a radiographic inspection was based only on etched crack specimens [1].

The section begins with a review of the results of pre- and post-etching radiographic inspections of the Convair and Martin Marietta crack specimens.

10.1 Review of Radiography Inspection of Etched Crack Specimens by Convair Aerospace and Martin Marietta

The Convair Aerospace etching material removal was not reported. However, based on the etching rate and time of etching, it is estimated to be approximately 0.00075" (0.019mm) of material, and the Martin Marietta etch removed approximately 0.002" (0.051mm) of material, with both etches having been performed after crack growth. Therefore, Martin Marietta removed approximately 2.7 times more material than Convair Aerospace.

The Convair Aerospace report states cracks were visible with optical magnification following etching; note, the precise magnification was not reported. The Martin Marietta report states the cracks were visible without optical magnification. Therefore, the post-etching opening gap of the crack was likely larger for the Martin Marietta specimens than for Convair Aerospace specimens.

Martin Marietta and Convair Aerospace performed radiographic inspections of the cracked panels before and after etching. Convair Aerospace reported one less crack was detected after etching. However, Convair reported on only approximately one-third of the specimens supplied to Rockwell for their final POD assessment.

Martin Marietta performed radiographic inspections of more cracks than they supplied to Rockwell and reported a significant increase in the number of cracks detected post-etching. Martin Marietta breaks their results into two groups: the number of cracks detected by at least one inspector (always the largest number); and the number of cracks detected by all three inspectors. Their results are presented in Table 10.1-1 where about 4 times as many cracks were detected after etching by at least one of three inspectors. After etching about 6 times as many were detected by all three inspectors. Their results did not record if there was a difference between the thinner and thicker plates. Martin Marietta results clearly indicate etching increases the crack detectability. They attribute the difference between theirs and Convair Aerospace results as being due to the extent of etching. This is a reasonable explanation since the etching by Martin Marietta resulted in visible cracks without magnification, while optical magnification was required to visualize the cracks after the Convair Aerospace etching.

Approximately 75% of the cracks examined for the Bishop POD study were fabricated by Martin Marietta. Of these cracks, 28% were not detected by all three inspectors before etching, but were detected by all three inspectors after etching. Therefore, approximately 21% of the cracks examined for the Bishop POD study had radiographic detectabilities that were significantly increased by etching.

Table 10.1-1. Martin Marietta data on crack detection before and after etching.

	Number of Inspectors	Number of 328 Cracks Detected	Percentage Detected
Before Etching	1	51	15%
	3	20	6%
After Etching	1	197	60%
	3	113	35%

10.2 Microscopic Examination of Pre-Etch and Post-Heavy Etch Crack Surfaces

Before etching, optical microscopy was performed on specimens AL7, AL8, AL9, and AL11 at MSFC to image the crack and estimate the width of the crack opening. The micrographs were acquired with a high-resolution microscope with an approximate resolution of 0.5 μm. The micrograph of AL7 was the only image where a crack was detectable. For the other three specimens, it was postulated that the post-crack growth machining smeared aluminum over the crack, thereby hiding it. Following the light etch, microscopy was not performed due to time constraints and equipment availability.

Following the heavy etch it was noted that all the cracks were visible without magnification. Micrographs of the cracks were acquired with a lower resolution microscope available at LaRC. Micrographs and estimates of the crack opening width before and after etching are presented in the next four subsections.

10.2.1 AL7 Microscopic Image of Pre-Etch

A comparison of the radiograph with the specimen rotated 20° and an optical micrograph of AL7 is shown in Figure 10.2.. The radiograph was acquired post-heavy etch, and the micrograph was acquired before etching showing that some parts of the crack (labeled A, B, and C) are not visible in the micrograph before etching. The radiograph was manipulated to have the same orientation as the micrograph. The center image is the path of the crack as estimated by using expanded views of the micrograph without referring to the radiograph. As can be seen from the comparison of the center and bottom images in the figure, the estimated path of the crack (in red) from the micrograph is similar to the path of the primary radiographic indication for the stage/specimen rotated 20°. Comparison with other rotation angles suggests the significant indication in this radiograph is from the surface etch. However, the tip of the crack designated by C is difficult to detect in the optical image, even in a magnified view.

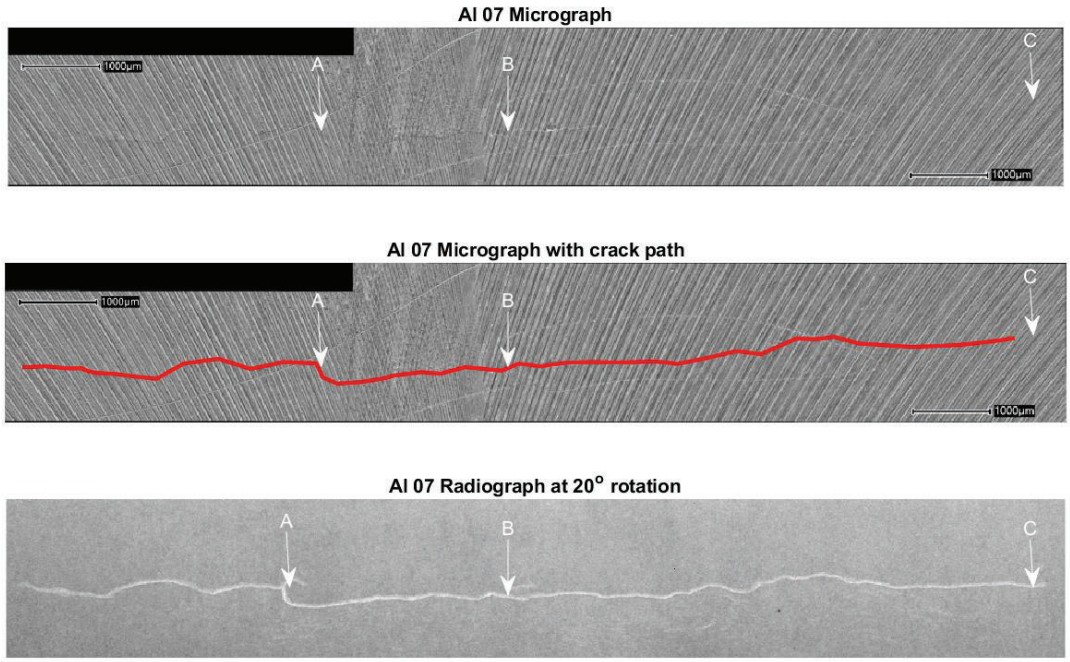

Figure 10.2.1-1. Comparison of AL7 micrograph and DR radiograph at 20° rotation

While the crack in the region indicated by C is difficult to visualize in the micrograph, after comparison to the radiograph, a closer examination of the region was performed. A closeup of all three regions are shown in Figure 10.2.. The crack opening is clearly seen in the images of locations A and B. A closer examination of the location C shows a faint indication of the crack, denoted by the white arrow. These images are utilized to estimate the crack opening widths. The opening widths in locations A and B vary significantly from point to point, with values ranging from about 1 µm to 5 µm, with an average opening width of 3 µm. The diagonal indications are likely due to the machining performed to remove material after crack growth. For future studies it is recommend machining in the direction of the crack in the future, and perform a surface polish instead of etch to remove smearing without etching crack fracture surface.

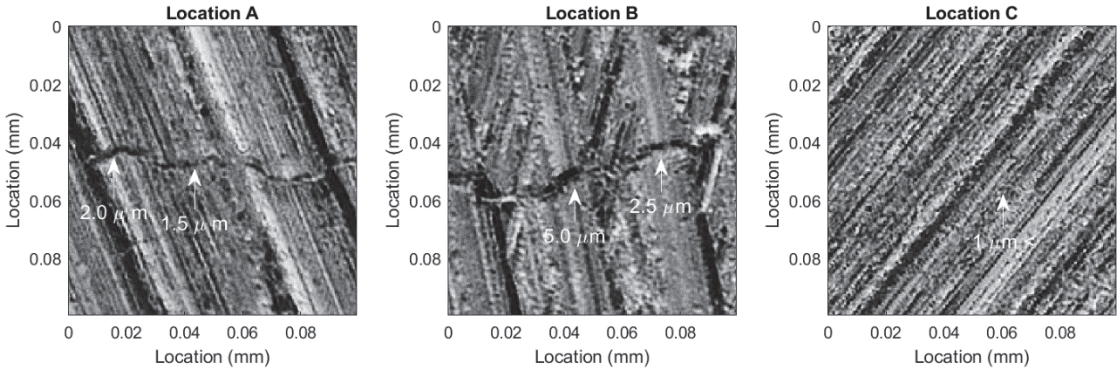

Figure 10.2.1-2. Different regions of the micrographs of AL7 indicating the variable gap widths.

In location C, the crack is barely visible in the micrograph. An estimate of the crack opening at this location is less than 1 µm. For a radiographic inspection, if the entire depth of the crack is open less than 1 µm, then it is considered to be a tight crack and detection with radiography is

unlikely [15]. Since this is at the tip of the crack, its depth is expected to be less than at the center of the crack.

10.2.2 AL7 Microscopic Image of After Heavy Etch

Following the heavy etch, AL7, AL8, AL9, and AL11 were imaged optically with magnifications between 2.5x and 50x to measure crack opening, etch depth, and crack profile along the length of the cracks. It was noted before using a microscope that the cracks were visible without aid of magnification. Samples AL7 and AL11 were found to have smaller etched crack openings, measuring approximately 60 µm. Samples AL7 and AL11 also had fine crack like features visible approximately 100 µm beneath the surface at an apparent bottom of the etched region. Samples AL8 and AL9 had wider crack opening on the etched surface, and a clear bottom of the etched region could not be imaged.

A comparison of the post-heavy etch microscopic image and the radiograph acquired with the specimen rotated 20° is shown in Figure 101. A comparison of the two images shows the same features of the crack visible in both. At locations designated by A and B, unusual features are visible in both images. These features are not clearly visible in radiographs acquired after the light etch, however, the maximum rotation of the specimen was only 10°. Location C is a portion of the crack that was difficult to detect in the microscopic image acquired before etching but is clearly visible in the microscopic image acquired after etching (see Figure 10.2.1-1).

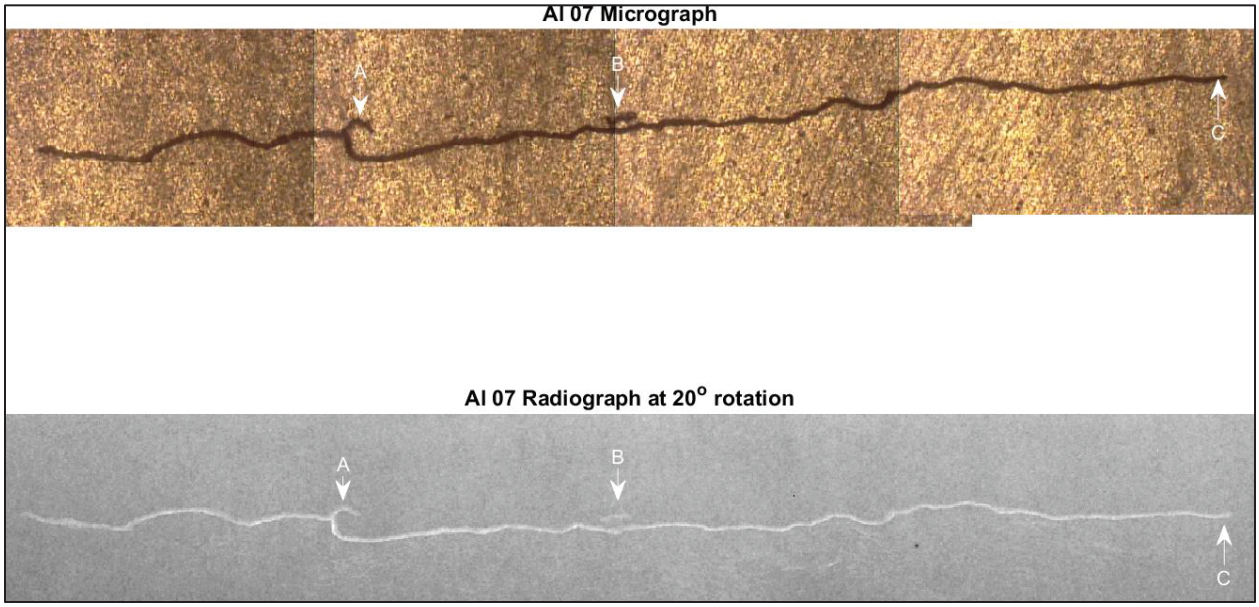

Figure 10.2.2-1. Comparison of microscopic image of crack and DR radiograph at 20° rotation for AL7 post-heavy etch. (The micrograph has been flipped about the horizonal axis to have the same orientation as the radiograph.)

High magnification micrographs of a small region of the crack in AL7 after the heavy etch are shown in Figure 10.2.2-2. The image on the left is with the microscope focused to the surface of the specimen. The edges of the crack are in focus, enabling a measurement of the width of the crack opening which is up to 66 µm but varies depending upon the measured location. The image on the right is focused 0.1 mm below the surface enabling imaging of the details at the bottom of the canyon created by the etching. At the bottom of the canyon, it is possible to see the crack

opening and estimate the crack opening at this depth of 0.1 mm to be 1 µm. If this is the case, this would be considered to be a radiographically tight crack.

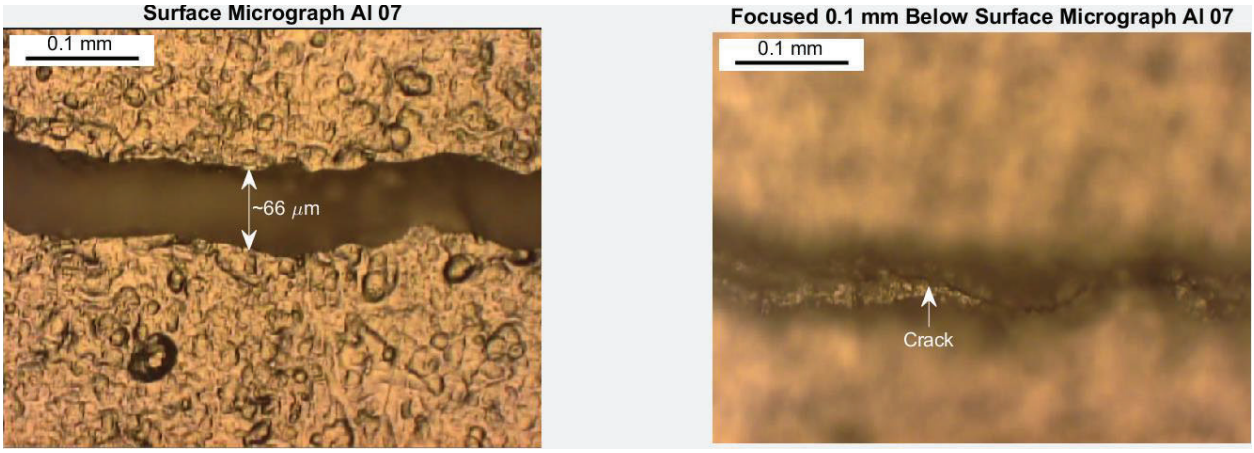

Figure 10.2.2-2. High magnification micrographs of a small region of the AL7 crack, with the microscope focused on the surface and at the bottom of the canyon created by the etching.

10.2.3 AL11 Microscopic Image of After Heavy Etch

High magnification micrographs were also obtained for a region of the crack in AL11, both focused on the surface and at 0.1 mm below the surface. A small region of the crack is shown in Figure 10.2.3-1, with the canyon created by the etching clearly visible in the image on the left and a small crack visible at the bottom of the canyon in the right image. As noted in the figure on the left, at least one point along the canyon is about 57 µm wide but will vary depending upon the measured location.,

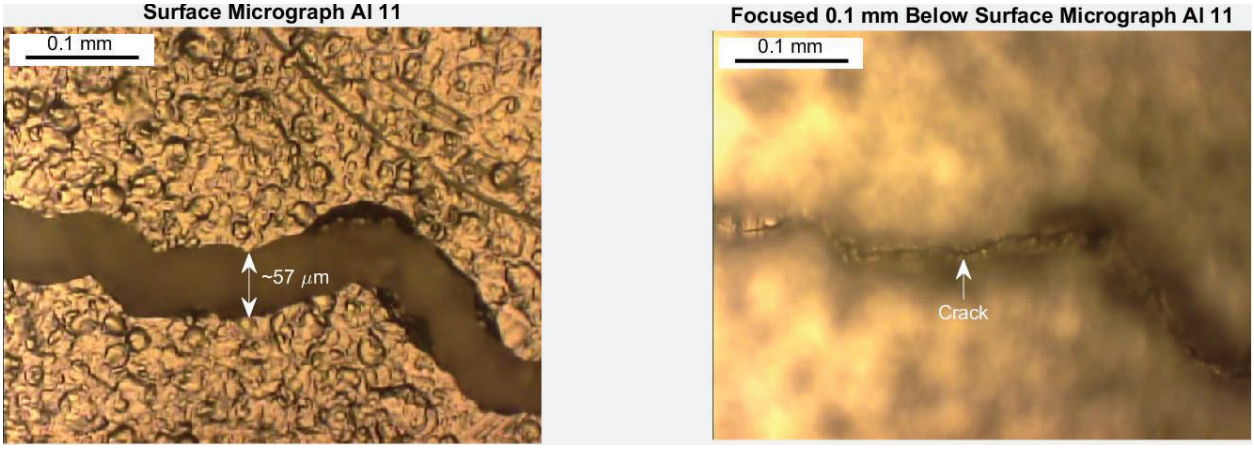

Figure 10.2.3-1. High magnification micrographs of a small region of the AL11 crack, with the microscope focused on the surface and at the bottom of the canyon created by the etching.

10.2.4 AL8 and AL9 Microscopic Image of After Heavy Etch

The high magnification micrographs of a region of the cracks in AL8 and AL9 are shown in Figure 10.2.4-1. An immediately noticeable difference between these canyons and the canyons in AL7 and AL11 is that they are considerably wider. For AL7 and AL11, the surface canyon width is approximately 60 µm, while for AL8 and AL9, the widths are approximately 90 µm and 130 µm, respectively. For AL8 and AL9, it was not possible to obtain micrographs focused such that

the bottom of the canyon is visible. This is presumably because the bottom of the canyon is too deep to obtain good images.

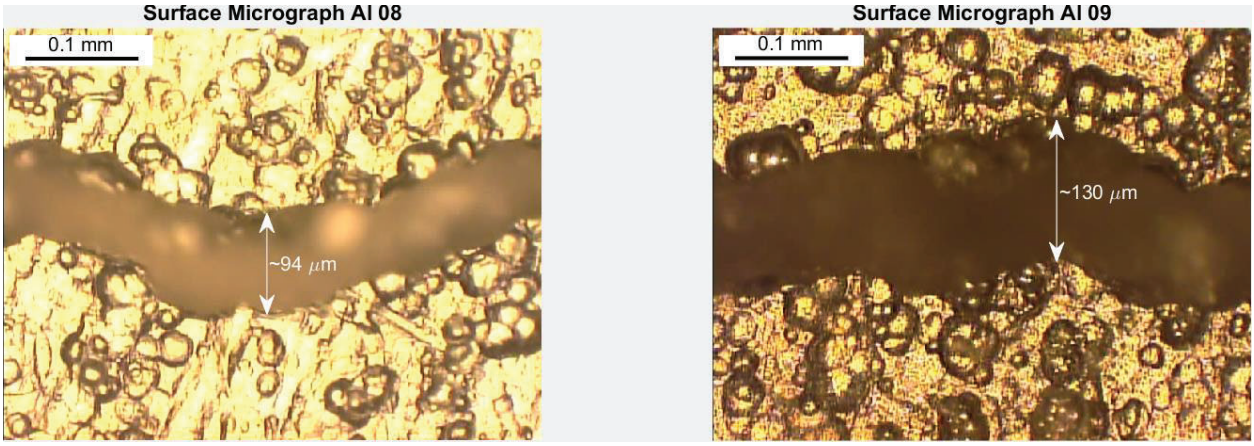

Figure 10.2.4-1. Micrographs of a small region on the cracks in AL8 and AL9.

Radiography images will indicate the amount of material difference between the cracks and the surface including the amount of material removed by etching. From the micrographs, etching canyons of AL8 and AL9 are expected to have much larger indications than the canyons in AL7 and AL11 because of the crack opening width. The significant difference in the radiographs for these different etches is seen in Section 10.4.

10.3 Computed radiography images of aluminum plates pre-etch, and post-light etch

During sample fabrication, a limited number of CR radiograms were taken prior to etching and after the light etching. Portions of the CR data containing the cracks are shown in Figure 10.3-1 and Figure 10.3-2. The CR data were taken with UR-1 imaging plates and digitized using a Fuji CR-IR 385 scanner. The software that was used to calculate the CNR values and generate the MSFC report was Fuji's DynamIx VU proprietary software. The CR data that were taken did contain high levels of background noise that influenced the CNR metrics. But the data are good enough to provide a visual and semi-quantitative inference on the effect etching can have on the visibility of a crack under X-ray inspection.

In three of four samples where CR was performed, the crack is visible prior to etching (AL7, A11, AL37). In two of these (AL7, AL11) the cracks appear to get more visible post-etch where AL37 visually appears the same. One of the four samples, AL9, is not visible prior to etching and is visible post-light etch as can be seen in Figure 10.3-1. Additionally, the CNR value for AL9 triples post-light etching. It is noteworthy that sample AL9 is similar in thickness to the samples used in the historical data as well as having an a90 close to the 0.7t that is stated in NASA-STD-5009C.

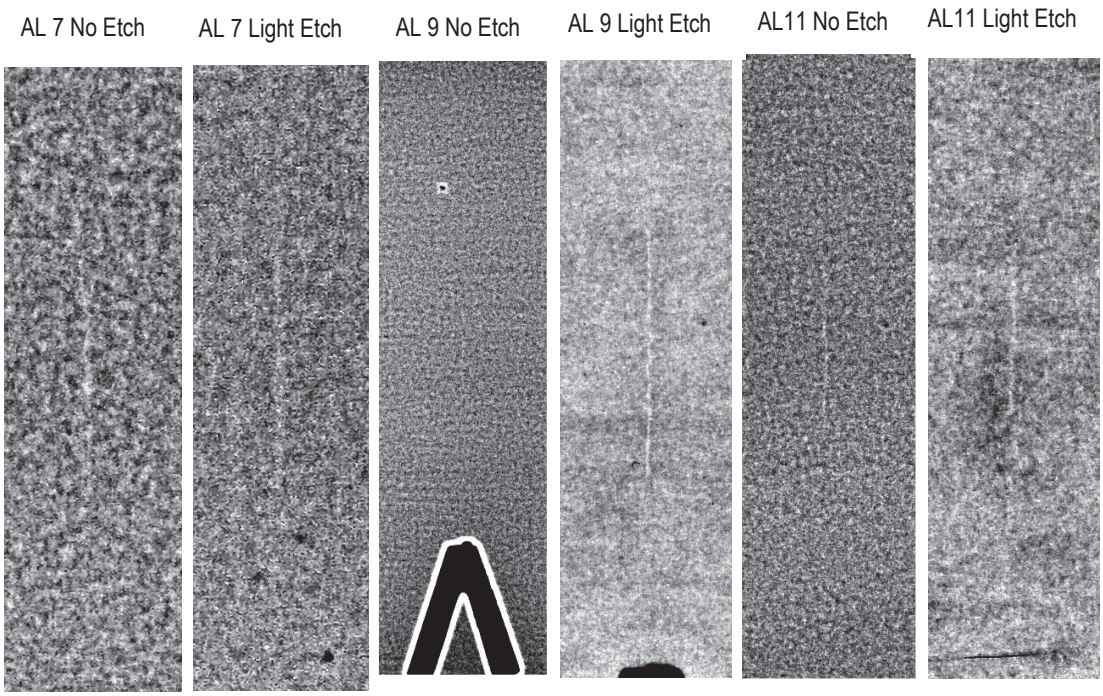

Figure 10.3-1. Comparison of computed radiography images of AL7, AL9, and AL11 pre-etch and post-light etch with zero rotation angle.

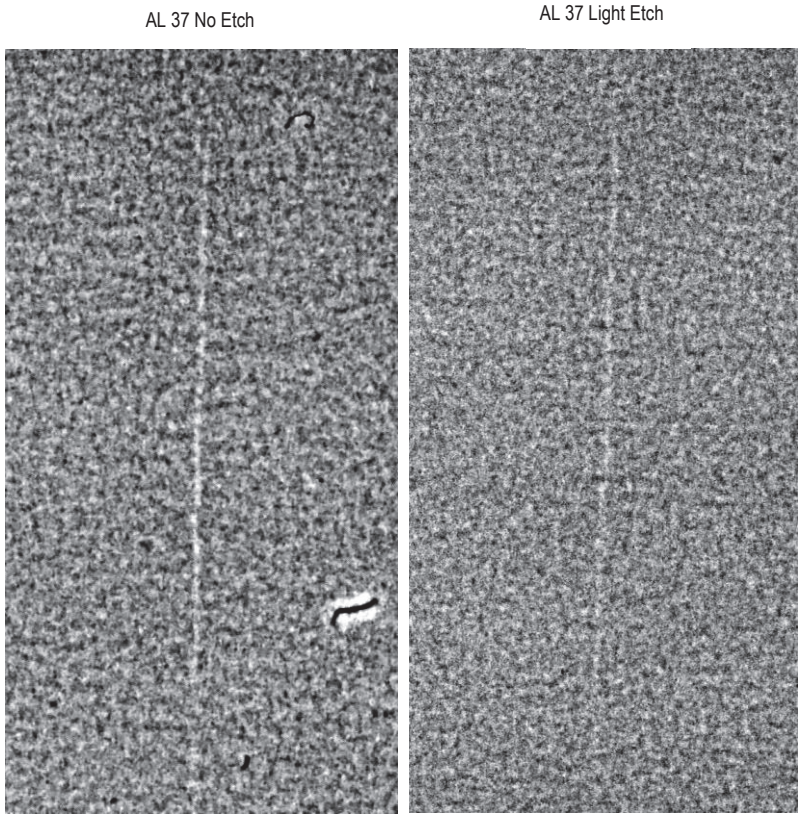

Figure 10.3-2. Computed radiography images of Al 37 pre-etch and post-light etch with zero rotation angle.

The pre-light and post-light etch CR data show that even under light etching conditions, a crack in a sample could be missed in the as-fabricated condition. However, it was determined that it was not possible to isolate the effect of the image acquisition and automated processing from the etching effect.

A limited number of samples were studied under these conditions, and future studies should be conducted with a statistically relevant sample set. But these data are important since the current practice in NASA-STD-5009C is that etching is not required prior to X-ray inspection. Additionally, as previously discussed in Section 9.2.1, the critical flaw size tables in NASA-STD-5009C are based on specimens tested that were etched prior to inspection. Current observation of a crack transitioning from non-visible to visible with CR inspection after light etching has implications to the validity of the original inspection data that the current NASA-STD-5009C X-ray tables are based on.

10.4 Digital radiography images of aluminum plates following a light and heavy etch

Digital radiography of three aluminum plates following a light and heavy etch are shown in Figure 10.4-1. There are no digital radiographs of the specimens prior to the light etch but a limited sample of CR data was completed prior to etching. All the digital radiographs were acquired with a zero angle of rotation. The sample is placed in the measurement system such that the zero rotation is as close as possible to when the crack is aligned along a line between the center of the source and the center of the detector. This orientation should give the maximum radiographic indication amplitude. There may be some orientation error since the plates are mounted on a stand that is significantly removed from both the source and detector. Therefore, the angle between the centerline of the source and detector and the surface normal of the plate is likely non-zero. This misorientation would result in the radiograph not showing the maximum indication. However, based on radiographs with small angles of rotation, the effects appear to be relatively small. A comparison of the available no etch and light etch results is shown in table 10.4-1.

Table 10.4-1. CNR Values for AL Samples Pre- and Post-light Etch

Specimen	No Etch CNR	Light Etch CNR	No Etch Maximum CNR	Light Etch Maximum CNR
AL7	1.474	1.115	2.482	1.762
AL9	0.665	1.809	1.183	3.807
AL11	1.459	2.87	0.515	1.556
AL37	1.547	0.881	2.82	1.549

For AL7 and AL11, the indication at the center of the crack is not significantly more visible in the light or heavy etches. For AL9, the entire length of the indication is significantly more visible in the heavy etch specimen in the digital radiographs.

From the CR inspection, AL7 and AL11 showed no difference in detectability between the pre-etch and light-etch crack condition, and AL9 went from non-visible to visible detectability. From the DR inspections (see figure 10.4-1), AL7 and AL11 showed no significant difference in detectability from light-etch to heavy-etch crack condition, and AL9 showed a significantly more visible detectability. Therefore, the heavy etch of AL8 and AL9 would almost certainly have been detected with the CR.

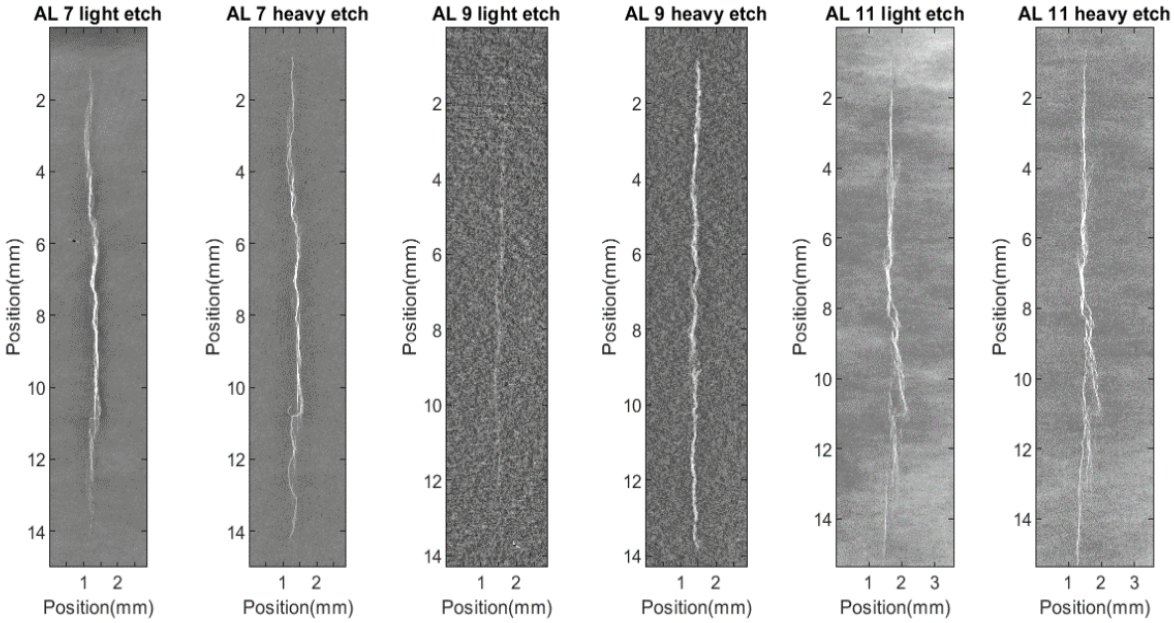

Figure 10.4-1. Comparison of digital radiography images of AL7, AL9, and AL11 post-light etch and heavy etch with zero rotation angle.

Figure 10.4-2 shows the 0° digital radiograph of the crack of specimen AL8 after heavy etching (left image) and the same radiograph having the estimated path of the crack highlighted (right image). The paths were also estimated for AL7, AL9, and AL11, all after heavy etching. The change in intensity along theses paths are shown in the right two plots of Figure 10.4-2. The shape of the profiles AL7 and AL11 are significantly different than the shape of the profiles for AL8 and AL9. AL7 and AL11 have a somewhat Gaussian shape, suggesting the depth of the crack decreases for increasing distances from the center of the crack as would be expected for a half-penny-shaped crack. AL8 and AL9 have an almost Heaviside Pi function shape, where the shape drops off at the end of the cracks. For AL9, the length of the indication is approximately 11.6 mm as compared to a length of 11.41 mm, measured by dye penetrant post-etching. For AL8, the length of the indication is 7.3 mm from the radiograph as compared to a length of 7.65 mm as measured by dye penetrant. As will be discussed in the next section, differences between the two shapes are indicative of a significant subsurface contribution to the amplitude.

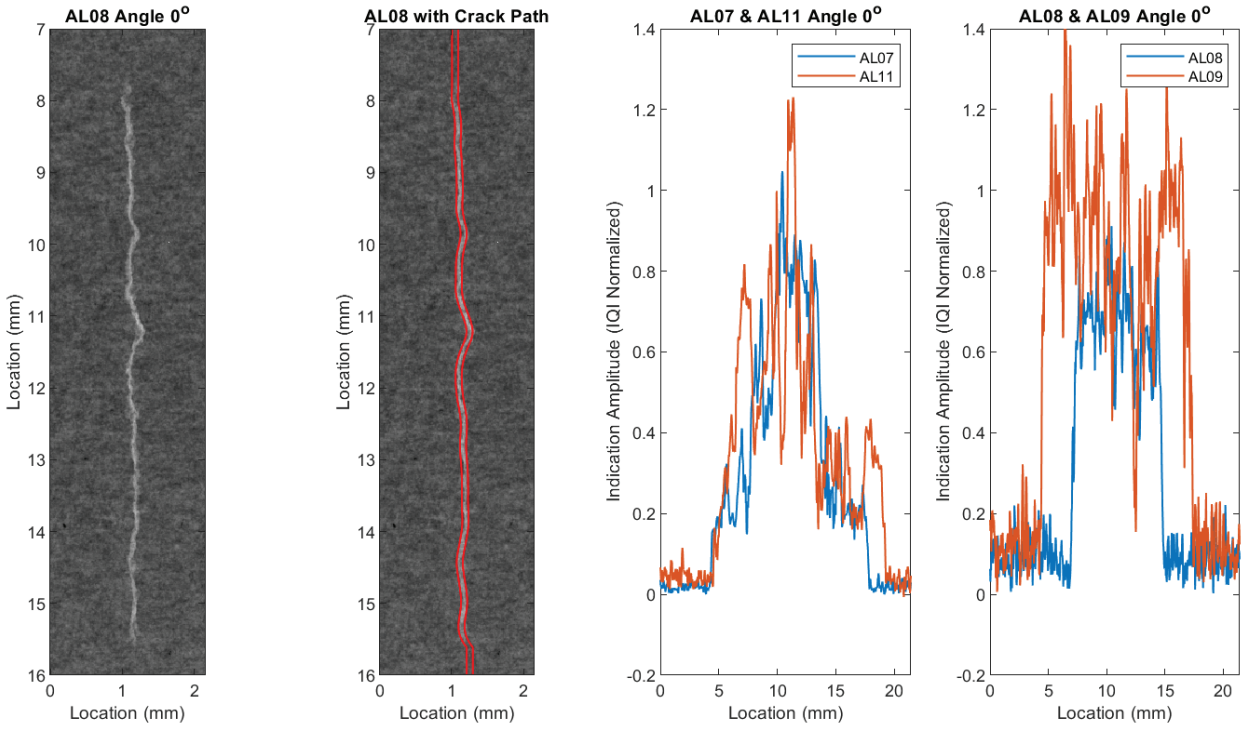

Figure 10.4-2. Digital radiograph of AL8 at 0° without and with estimated plot of crack location. The two right plots are of the values of the intensities along the crack path for AL7, AL8, AL9, and AL11 following heavy etches.

10.5 Simple Simulation of Rotated Specimen with Different Crack Configurations

To help interpret the off-angle digital radiographs, three configurations, shown in Figure 10.5-1, for the crack with and without etching were simulated. The crack is simulated with four long rectangular boxes designated in the figure as segments 1 to 4, with depths of 1. mm, 0.25 mm, 1. mm, and 0.25 mm, respectively, and offset such that they stack on each other in a plate 3mm thick. For all cases, segments 1 and 3 are set to be a tight crack with widths of 0.25 µm. For cases 1 and 2, segments 2 and 3 have gap openings of 8 µm. The length of all of the segments were 10 mm which extends in and out of the plane visualized in Figure 10.5-1.

Case 1 is intended to simulate a crack that is detectable before etching. The widths for segments 2 and 4 are 6 µm. These components of the crack enable its detection before etching.

Case 2 is intended to simulate the same specimen post-etch. The widths of all the crack segments are unchanged from Case 1, but the top half of an ellipsoidal cylinder (shown in Figure 10.7.1-1) is used to simulate the material removed by etching.

Case 3 is intended to simulate a tight crack specimen post-etch. All the crack segments are set to widths of 0.25 µm, and the same one half of an ellipsoidal cylinder is used to simulate the material removed by etching.

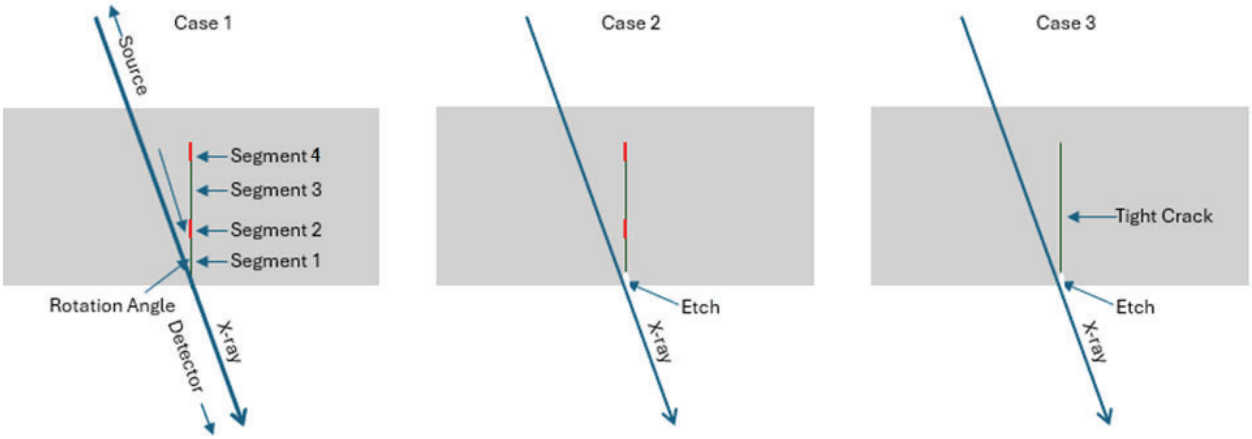

Figure 10.5-1. Configurations of simulation setup for the specimens in Cases 1-3

For all three cases, the three angles of rotation were 0°, 10°, and 20°. The simulations were performed such that the source and detector were rotated about the crack opening. In the plots of the crack projections shown in Figure 10.5-2, the center of rotation is at zero. Case 1 is the set of plots on the far left; Case 2 is the middle set of plots; and Case 3 plots are on the far right. The rows from top to bottom are 0°, 10°, and 20°, respectively. For all cases, the largest indication amplitude occurs when the X-ray beam is parallel to the crack (a rotation angle of 0°).

As the source and detector are rotated, segments 2 and 4 are offset from x=0. It is possible to estimate their depth via triangulation. As the rotation angle increases, the length of the projections for segments 2 and 4 increases and the amplitude decreases since the path of the X-ray beam through these segments decreases.

When an etching component is added to Case 1 to get Case 2, the indication amplitude increases by about 20%. For Cases 1 and 2, as the angle between the X-ray beam and the crack increases, the projections for segments 2 and 4 move away from the origin and the amplitude of the projections as shown in the middle plots decreases. For segments 2 and 4 in the simulation, the amplitude of the projection is approximately proportional to the width of the segment times the cosecant of the angle for X-ray passing through the two vertical sides of the segment. For Case 1, as the projections from subsurface components move, there is no longer an indication at x=0 due to the absence of the canyon created by etching.

For Case 2, the indication from the etch canyon is still projected at x=0 for rotation angles of 10° and 20°. The projections from subsurface components are identical to Case 1.

For Case 3, the primary indication is always at x=0. The material loss from the etch is shallow and the shape of its indication does not change significantly between 10° and 20°. Since all of the subsurface components are tight cracks, the amplitudes of their indications are very small and are barely visible in the plot.

These simulations help in the discussion in Section 10.6; however, the real cracks in this study were much more complicated than the simple segments used in these simulations. Therefore, these simulations are not intended to provide results that precisely match the measurements on real cracks.

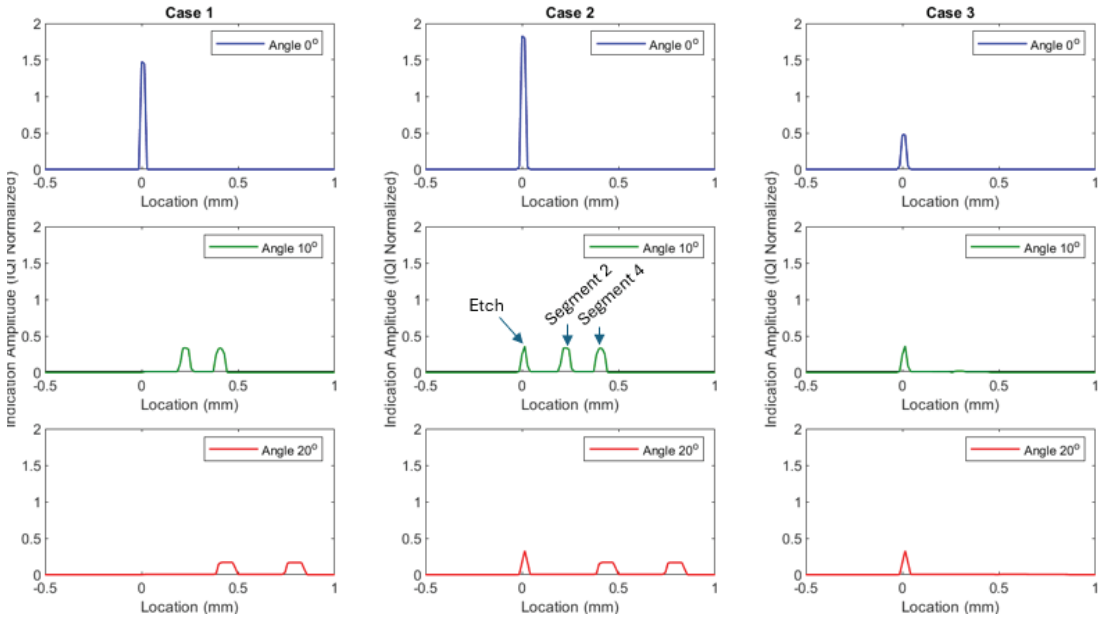

Figure 10.5-2. Profiles cross the simulation of cracks in Cases 1-3

10.6 Analysis of Post-Heavy Etch Specimens

10.6.1 AL7 Radiograph Image and Profile Comparison

Magnified comparisons of light and heavy etch in digital radiographs with the profiles across the center of the crack at for 0° and 10° rotations of AL7 are shown in Figures 10.6.1-1 and 10.6.1-2. This crack was visible before the etching in the CR images (see prior section). The radiographs and profiles are shown together to enable better visualization of the etching indication. Profiles show the values of the radiograph along the red line across the crack.

As can be seen in Figure 10.6.1-1 for 0° rotation, there is a sharp, relatively narrow peak for both the heavy and light etch AL7, which are approximately equal in amplitude. That they are approximately the same amplitude indicates the etching does not significantly increase the size of the indication.

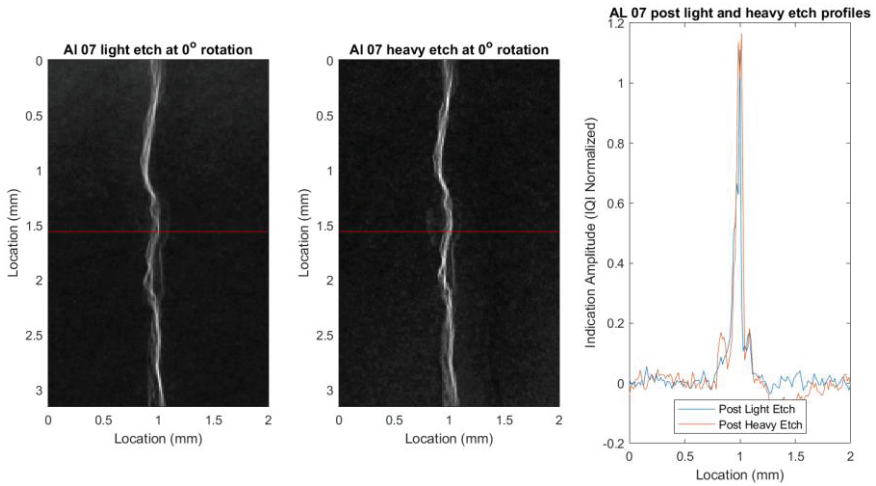

Figure 10.6.1-1. Digital Radiography: Comparison of post-light and heavy etch profile in AL7 for 0° rotation angle. The red line indicates the location of the profile.

While the effect of etching is not seen at 0° rotation, a radiographic indication related to the etching can be seen when the sample is rotated. For example, the 10° rotation is shown in Figure 10.6.1-2. The radiographs are visually similar except for the indication designated as the etch. The radiographic indication of the etching is visible when comparing the light and heavy etch radiographic profiles. The difference is similar to the difference between Case 1 and Case 2 simulations. The estimated depth of portions of the crack are indicated by the labels of 0.8 mm and 1.9 mm in the profile plot (see previous section). With the exception of the peak labeled as etch, the profiles are very similar with differences being probably due to a slightly different initial configuration of the specimens; specimens were placed on the rotation stage and aligned manually.

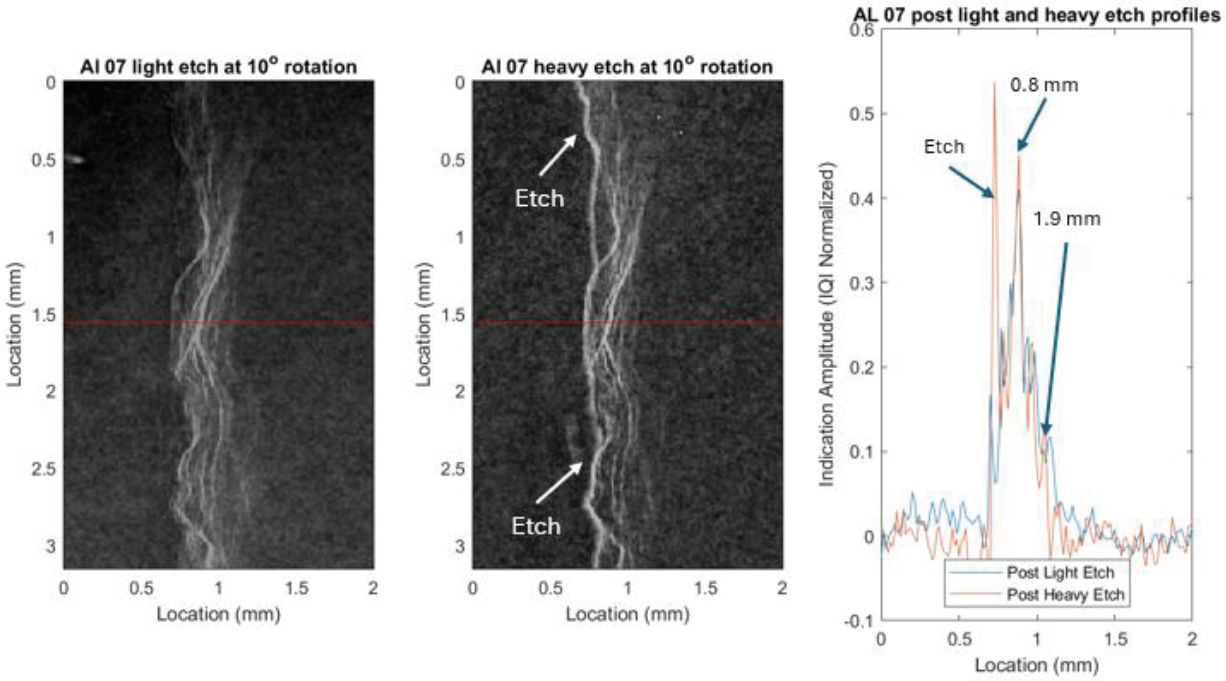

Figure 10.6.1-2. Digital Radiography: Comparison of light and heavy etch indication profiles for AL7 where specimen is rotated 10°

Based on PAUT measurements, the depth of the crack is 2.72 mm, which is considerably deeper than the 1.9 mm indication in the plot. There are multiple reasons why the this may be the case, including the deeper portion of the crack may be tight or the subsurface components of the crack are not in the same surface normal plane as the etch. It is notable that between the etch and the 0.8 mm labels in the profile plot, there is a dip in the amplitude, which is indicative of a reduction in the crack width in that region.

10.6.2 AL11 0° and 10° Radiograph Image and Profile Comparison

Radiographic data for AL11 for the 0° and 10° rotations along a line are indicated in Figures 10.6.2-1 and 10.6.2-2. This crack was visible before the etching in the CR images. The center of the radiograph has the same pattern as was noted the AL7 radiographs with the amplitude of the indication after the heavy etch being approximately the same amplitude as the indication after the light etch.

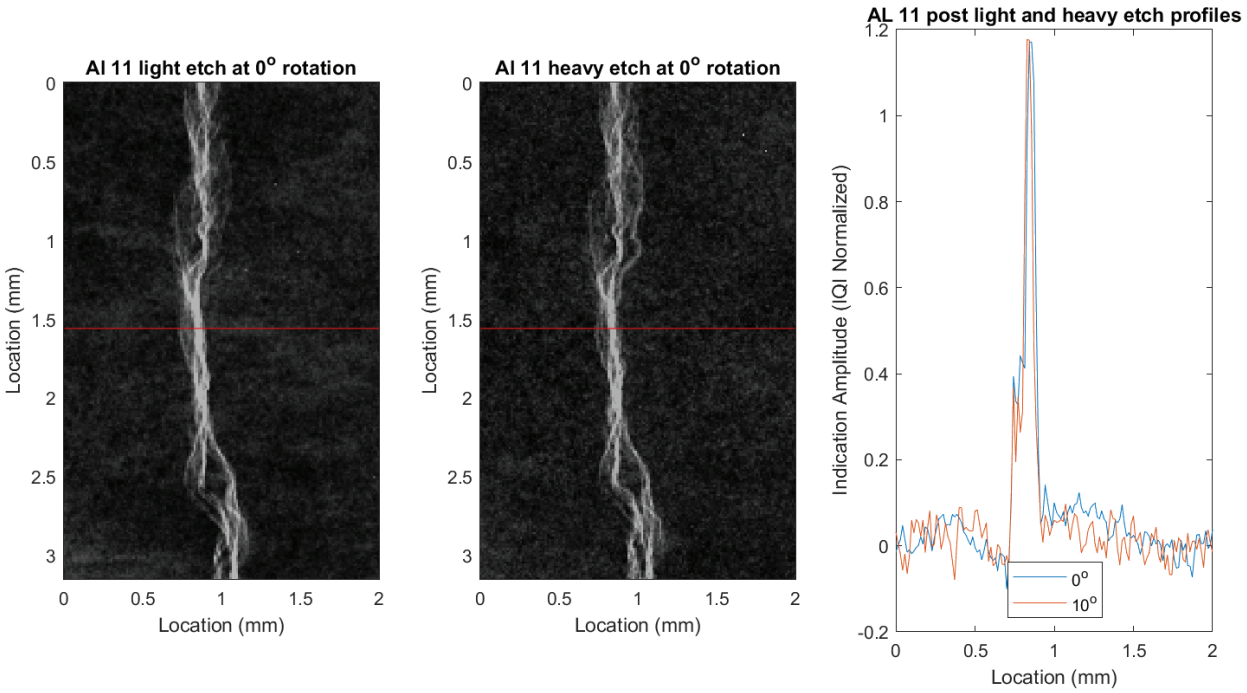

Figure 10.6.2-1. Digital Radiography: Comparison of post-light and heavy etch profile in AL11 for 0° rotation angle

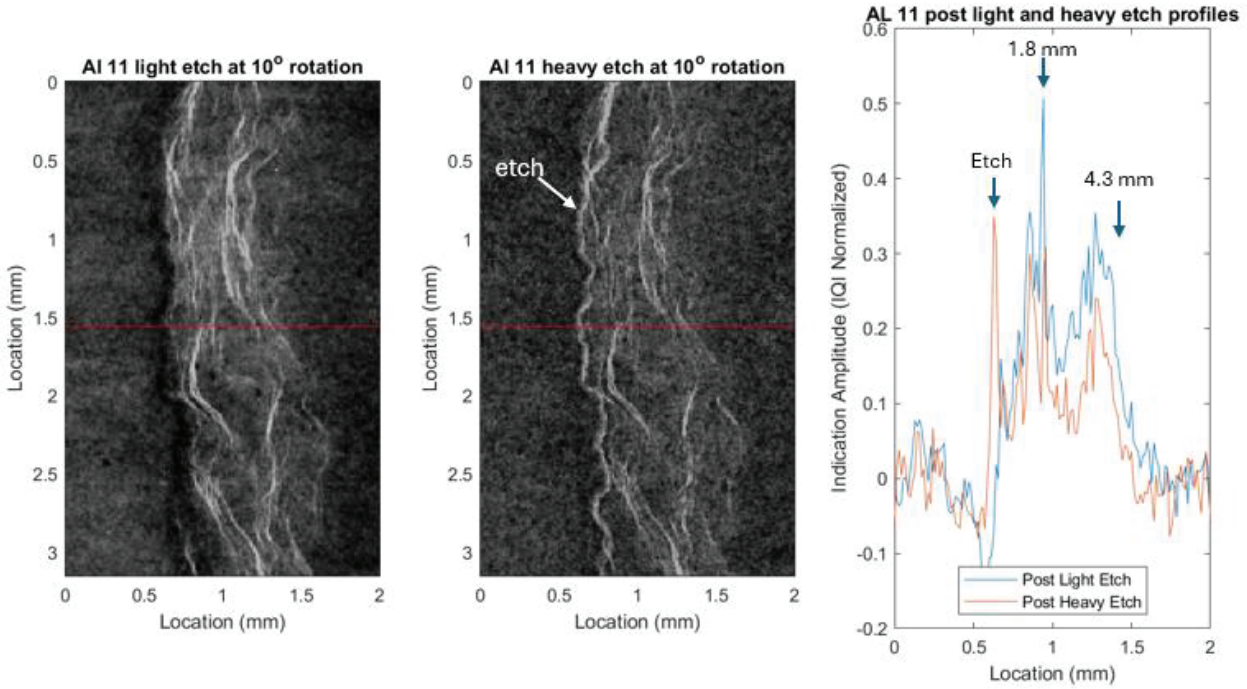

Figure 10.6.2-2. Digital Radiography: Comparison of light and heavy etch indication profiles for AL11 where specimen is rotated 10°

For the rotation of 10°, as was the case for AL7, radiographs are visually very similar except for the indication designated as the etch. The radiographic indication of the crack after etching is visible when comparing the light and heavy etch radiographic profiles. The difference is again

similar to the difference between Case 1 and Case 2 simulations. The estimated depth of portions of the crack are indicated by the labels of 1.8 mm and 4.3 mm, With the exception of the peak labeled as etch, the profiles are again similar with differences also probably due to slightly different initial configuration of the specimen. The estimated depth of the deepest component of cracks is 4.3 mm, which is close to the PAUT based measurement of 4.09 mm.

10.6.3 AL9 Radiograph Image and Profile Comparison

A comparison of the radiographic data for AL9 for the 0° is shown Figure 10.6.3-1. This crack was not visible with CR before etching as is discussed in Section 10.3. These computed radiography images show the visibility of indication is considerably increased after the heavy etch.

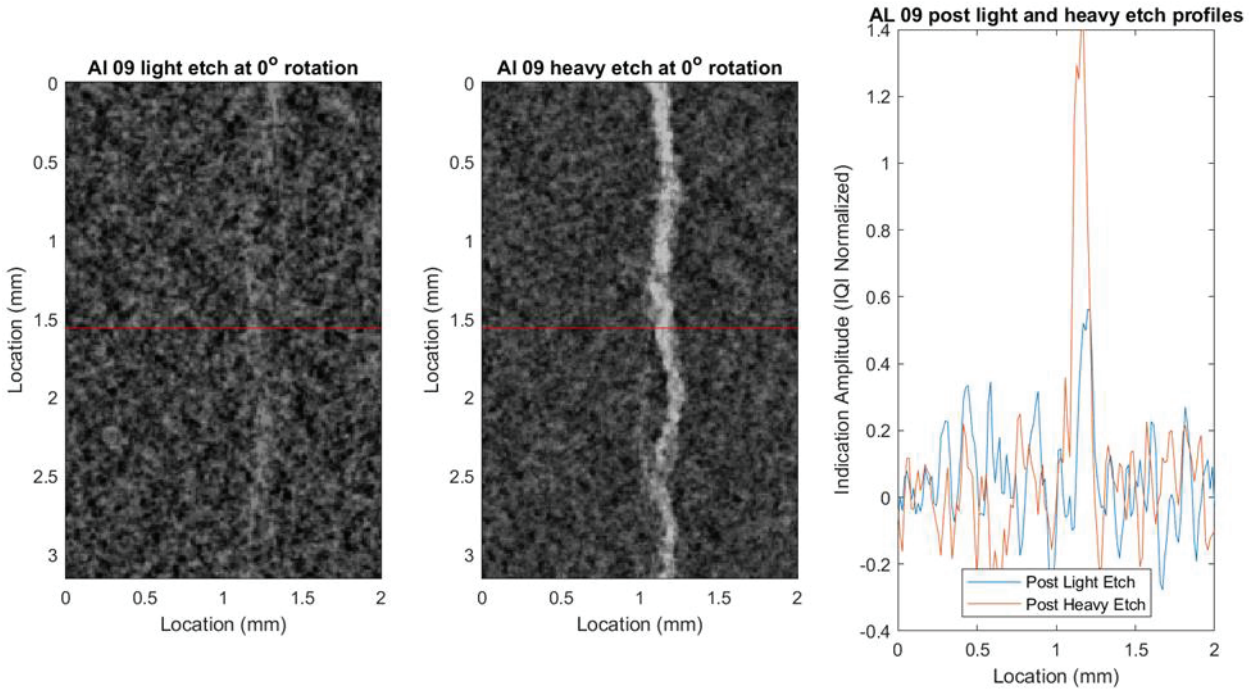

Figure 10.6.3-1. Digital Radiography: Comparison of light and heavy etch indication profiles for AL9 with the rotation angle of 0°

It is significant that the post-heavy etch indications at 0° of rotation for AL9 are almost the same amplitude and width as the 0° rotation radiographic indications for AL7 and AL11; therefore, while there was no visible indication with no etch via CR, after the heavy etch, the crack becomes visible. A comparison of the profiles is shown in Figure 10.6.3-2, where each profile is the average along a 1 mm length of crack starting at the approximate center of the crack. Also shown in the comparison is the profile for the 0° rotation radiographs image of AL8 discussed in the next section.

The indication amplitude is related to the reduction of mass along the path between the source and the detector relative to the nominal mass along the same path. Generally, the amplitude indication should be proportional to the mass removed by etching along the path of the crack. The largest normalized indication is from AL8. From Section 10.2.4, it is seen that this crack has the largest surface gap (130 µm) post-heavy etch, and the canyon was deeper than AL7 or AL11. AL9 has the second largest gap of 94 µm, and its canyon was also deeper than AL7 or AL11.

Since the canyon indications for post-heavy etch of both AL8 and AL9 are approximately as large as AL7 or AL11, they should have been just as detectable as AL7 or AL11 were by CR prior to etching.

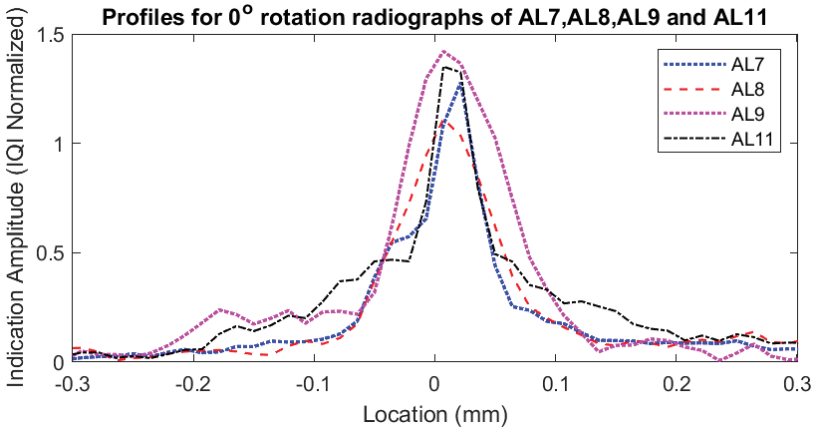

Figure 10.6.3-2. Digital Radiography: Post-light-etch Comparison of the profiles across the center of the 0° rotation radiographs of AL7, AL8, AL9, and AL11

The 10° rotation light etch and heavy etch radiographs for AL9, shown in Figure 10.6.3-3, are different than the radiographs at 10° rotation for AL7 or AL11 in that no subsurface crack components are visible in either of the radiographs. The PAUT measurement for the crack depth is 4.09 mm extending from 0 mm to 2.7 mm, however, in the lightly etched radiograph, there is no indication in that region above the noise. This is like the Case 3 simulation (Section 10.5), where the 10° simulation has an indication with approximately the same shape and amplitude as the 0° indication. This implies the initial fatigue crack gap was 1 µm or less and too tight to produce a significant radiographic indication, even with light etching. The heavily etch canyon at the crack opening is only feature detectable with DR.

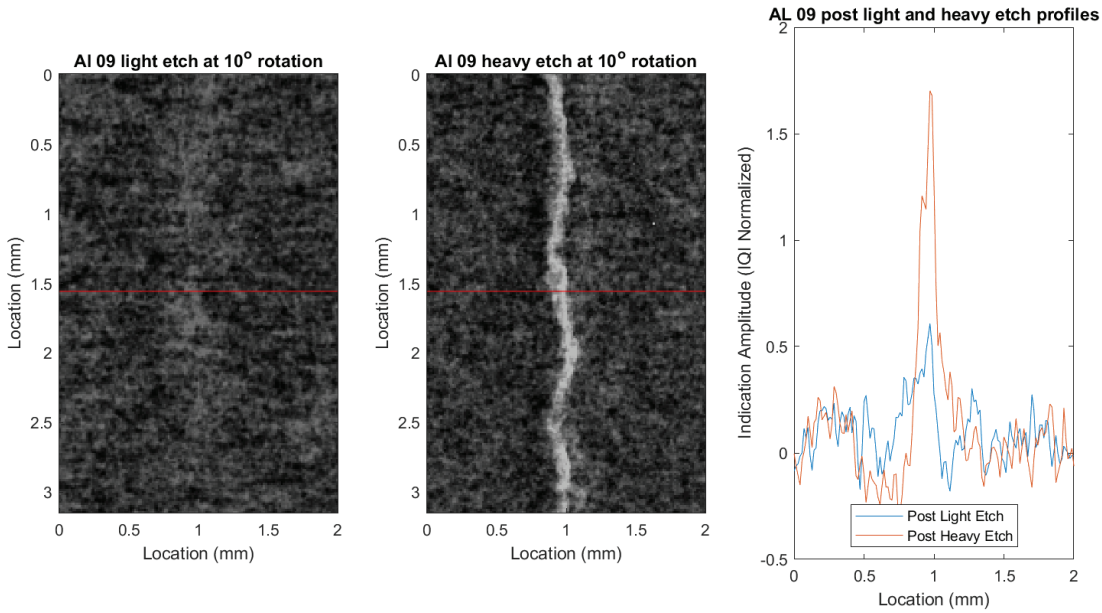

Figure 10.6.3-3. Digital Radiography: Comparison of light and heavy etch indication profiles for AL9 with the rotation angle of 10°

10.6.4 AL8 0° and 10° Radiograph Image and Profile Comparison

A comparison of the computed radiographs at 0° and 10° rotation acquired after the heavy etch of AL8 are seen in Figure 10.6.4-1. There are no digital radiography data for AL8 after the light etch. The images were acquired with the specimen rotated from -10° to 20°. The amplitude of the indication does not change significantly for all the rotations. The crack is identifiable following the heavy etch. For the 10° rotation, there is no indication of a subsurface component of the crack, and the crack appears to be similar to the Case 3 simulation (Section 10.5). While there is no significant subsurface contribution, the 0° and 10° rotation crack indications have amplitudes almost the same as the 0° rotation radiographic indications for AL7 and AL11. This is similar to Case 3 simulations (Section 10.5), where the 10º simulation has an indication with approximately the same shape and amplitude as the 0º indication. As was the case for AL9, this implies the initial fatigue crack gap was 1 µm or less and too tight to produce a significant radiographic indication. Only the indication from etch canyon is detectable with DR, and therefore, its detectability is not related to the crack depth. In a POD study, etched samples should not be included in the population of detectable cracks. However, for the Bishop POD study, cracks with similar amounts of etching were part of the population.

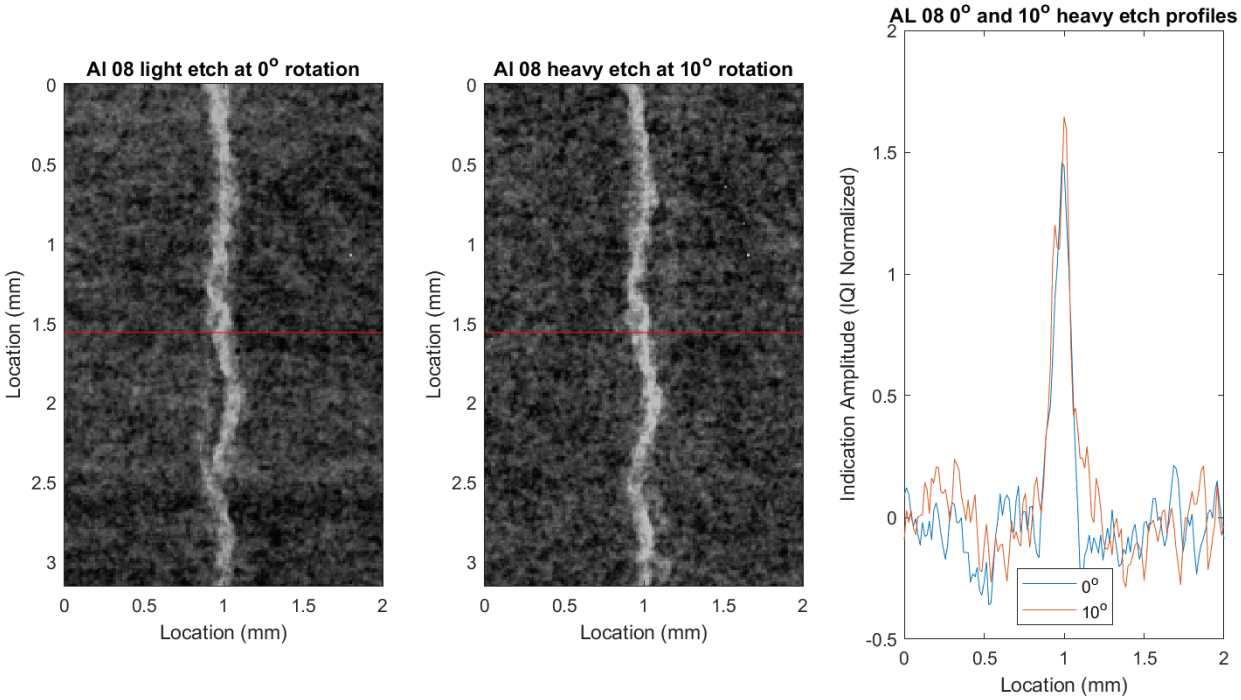

Figure 10.6.4-1. Radiographic data for AL8 after heavy etch

10.6.5 Comparison of Radiographs for 20° Rotation

Digital radiography for AL7 and AL11 for the 20° rotation are shown in Figure 10.6.5-1. The 20° rotation radiographs for AL7 and AL11 are significantly different than the 10° rotation computed radiographs seen in Figures 10.6.1-2 and Figure 10.6.2-2. For all the 20° rotations, the canyon created by the etch is the primary indication with a slight indication of subsurface components of the crack. Either the projections of subsurface portions of the crack are too thin to be detected or are translated far away from the etch projection as shown in Case 2 of Section 10.5. As shown in Figure 10.2.2-1, the indication in the 20° rotation radiograph of AL7 has the same shape as the

micrograph of the etch. This implies the indications in the 20° rotation radiographs of all four specimens are a result of the material removed by the etch (the canyon). Note that digital radiography post-etch for AL8 and AL9 for the 20° rotation are not significantly different from the 10° rotation. Indicating that the primary source of the radiographic response is from the canyon created by the etching.

The right two plots of Figure 10.6.5-1 are the peak values of the intensities along the crack path from the 20° rotation digital radiograph. At this rotation angle, the shape of the profiles AL7 and AL11 are also close to the Heaviside Pi function shape like AL8 and AL9, and different from the 0° rotation peak values for AL7 and AL11, which feature a Gaussian shape (see Figure 10.4-2). In Figure 10.6.5-1, since only the canyon created by the etch is being imaged, the Heaviside Pi function shape indicates the mass per unit length removed by the etch is same along with the entire length of the crack. For AL7, the length of the indication is approximately 13.3 mm as compared to a crack length of 11.68 mm as measured by dye penetrant. For AL11, the length of the indication is 14.8 mm as compared to a length of 13.84 mm as measured by dye penetrant. It is noted that AL11 appears to have several branching features as well but does not affect the length measurement. All the radiographic indications have lengths that are greater than the length of cracks as measured by dye penetrant. The amplitudes of the peaks for each of the specimens increase as the width of the canyon increases (Section 10.2), indicating that the narrowest canyon is in AL11 and the widest is AL9.

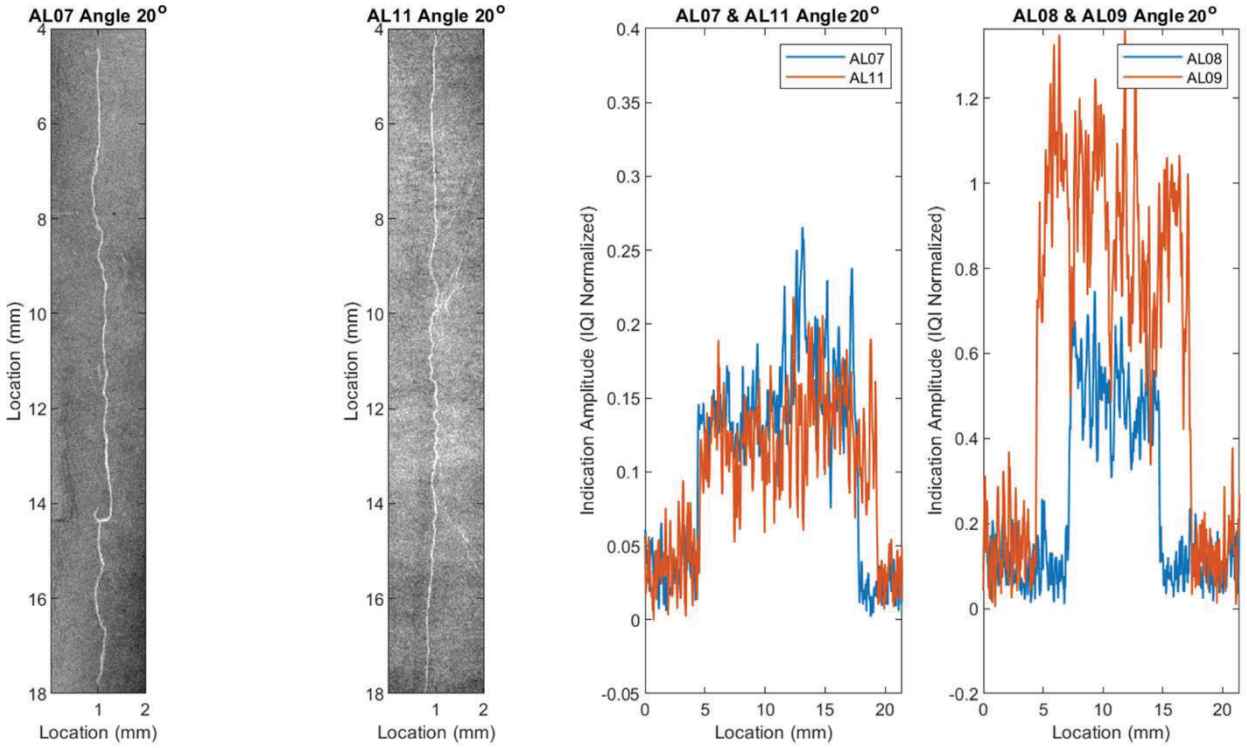

Figure 10.6.5-1. Digital radiographs of AL7 and AL11 at 20° rotation. The two plots on the right are of the peak values of the intensities along the crack path for 20° rotation of AL7, AL8, AL9, and AL11 following heavy etches

10.7 Estimation of Detectability with Etching with Film Inspection

While no film radiographs were performed for this study, this section attempts to determine if similar etching of a tight crack indication (Case 3 of Section 10.5) would be detectable by film radiography. In Section 10.6.5 it was noted that the mass per unit length removed along the crack by the etch is the same for the entire length of the crack. A wire can be placed on the surface, which would provide approximately the same amplitude and width indication (the sign is opposite since the wire adds mass instead than removing mass).

There are two steps to determine if the etched crack would be detectable by film radiography. First, the cross-sectional area of the etched crack is estimated by matching the 20° rotation radiography profile to the output of commercial simulation software. This step is discussed in the next section. Second, the diameter of an equivalent wire is assumed to have the same cross-sectional area as the etch. A formula equating a wire IQI to a plaque-type penetrameter/IQI relates the etch indication to the thickness of an equivalent plaque-type penetrameter/IQI. When the thickness of the equivalent plaque for an etch is greater than the 2-1T plaque penetrameter, the etch is designated detectable. This step is discussed in detail in Section 10.7.2.

10.7.1 Computational Simulations to Estimate Canyon Depth and Width

To estimate the cross-sectional area of the etch from the radiographic data, three-dimensional (3D) simulations were performed with a commercial simulation package, CIVA EXTENDE RT – CT, which is part of CIVA NDT Software for Simulation and Analysis [21]. The CIVA RT package includes film as a possible detector. It uses the EN 584-1:2006 European standard which requires a characterization of the density-dose curve to convert the dose to a film density. They have performed some validations of the film model for Kodak M100, which is the film in the Bishop report. For additional information regarding simulation of cracks and CIVA please refer to Appendix A.1.

For the simulation, the source-to-detector center distance is 1220 mm, and the source-to-crack surface is 81.333 mm, as was approximated from the measurement configuration. The simulation X-ray flat panel detector has a pitch of 0.02 mm, approximately 10 times larger than the spatial resolution of the experimental detector. The higher-resolution simulations guarantee the simulation ray tracing captures structural features, which are smaller than the detector resolution. The resulting magnification at the center of rotation is 14x with an effective spatial resolution in that plane of rotation of 1.428 μm for the simulation. These data are spatially averaged to give the 0.2 μm spatial resolution of the experimental flat panel detector with an effective spatial resolution in that plane of rotation of 14.28 μm. The simulation configuration is shown in Figure 10.7.1-1.

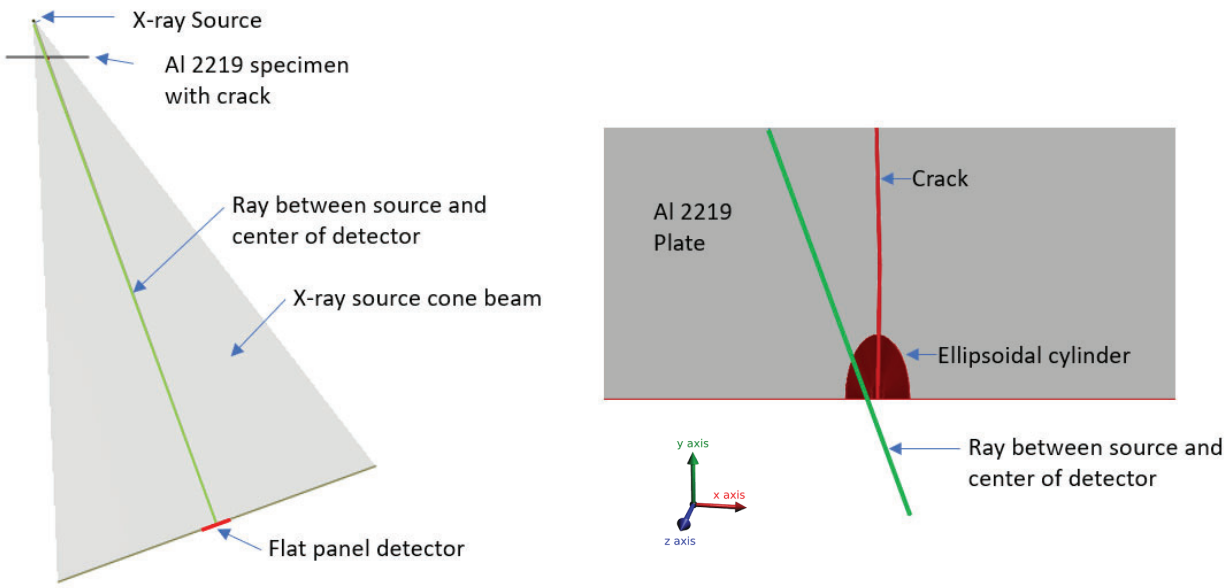

Figure 10.7.1-1. Simulation configuration with the left image giving the overall configuration and the right image focusing in on the crack surface and the ellipsoidal cylinder used to approximate the canyon

The right image of Figure 10.7.1-1 shows an expanded view of a cross-section of the 3D simulation configuration with a crack and an ellipsoid with the minor axis aligned with the surface of the specimen. The out-of-plane semi-axis (z-axis) of the ellipsoid was set to 10 mm (much thicker than the plate) to approximate, in the region of interest, a canyon with an ellipsoidal cylinder. The two-dimensional configuration in the figure shows a cross section of the ellipsoid with a major (y) axis of 0.05 mm and a minor (x) axis of 0.1 mm. A 75 keV radiograph is simulated, assuming the Al 2219 is an alloy with mean values of elemental composition for Al 2219. The same thicknesses of AL7, AL8, AL9, and AL11 were used for the thicknesses of the aluminum plates in the simulation. A thickness step increase in the aluminum plate of 0.127 mm located 1 mm to the right of the crack is used to simulate the IQI plaque thickness of the experimental configuration.

Simulations were performed with a grid search of major (y) and minor (x) ellipsoid axes for each plate thickness. A profile of the crack response was calculated from the noiseless simulation results by first subtracting the amplitude of the nominal plate response then normalized by using the simulated IQI amplitude which provides a predictable response between simulations. Each simulation profile was aligned with the 20° experimental crack response. At this angle, none of the radiographs show significant subsurface indications. The grid point with the smallest summed squared difference between the simulation profile and measurement profile was assumed to be the best estimate of the vertical (y) and horizonal (x) diameters.

From the radiographs acquired at 20°, estimated profiles of the canyon created by the etching were obtained. The profiles for AL7, AL8, AL9, and AL11 were compared with simulation results using their equivalent best estimate ellipsoids in Figure 10.7.1-2, which showed a significant variation in the amplitude of the canyon from specimen to specimen. The dimensions of the half-ellipse of the simulation, which best matches the experimental data, are given in Table 10.7.1-1, with the cross-sectional area of the canyon calculated from those parameters. Also shown in the table are the measurements of the width and depth as measured from the

micrographs in Section 10.2. The micrograph depths are based on the change in microscope focus required to bring the bottom of the crack into focus. There is not great agreement between the microscopic measurement and the values for width but though the trends are the same. The primary objective was to estimate the cross-section area of the canyon for determining the equivalent wire diameter in the next section.

For AL7 and AL11, the cross-sectional areas are in reasonable agreement between the microscopy and radiography, if the canyon is assumed to have a triangular shape. For AL8 and AL9, it is not possible to estimate the area, since the depth of the canyon is unknown. It is therefore assumed that the radiographic estimation of the material removed by the etch is accurate. It should be noted that this estimate is calibrated by the change in radiographic intensity between the base material and the IQI. Since the measurements and simulations are both IQI normalized, small changes in the chemical composition of the Al 2219, the X-ray source spectrum, or the detector sensitivity do not significantly change the relative measurements, since the amplitude of the indication is approximately the same size as the differential between the IQI and the base material.

Table 10.7.1-1 Simulation estimate of depths and widths of canyons with the estimated width and depth from the microscopic images.

Specimen	Width(µm)	Depth(µm)	Cross-sectional Area(mm²)	Micrograph Width (µm)	Micrograph Depth (µm)	Micrograph Cross-sectional Area(mm²)
AL7	35	45	0.0025	66	100	0.0033
AL8	100	50	0.0079	94	>100	>0.0047
AL9	100	187.5	0.0295	130	>100	>0.0065
AL11	50	30	0.0024	57	100	0.0029

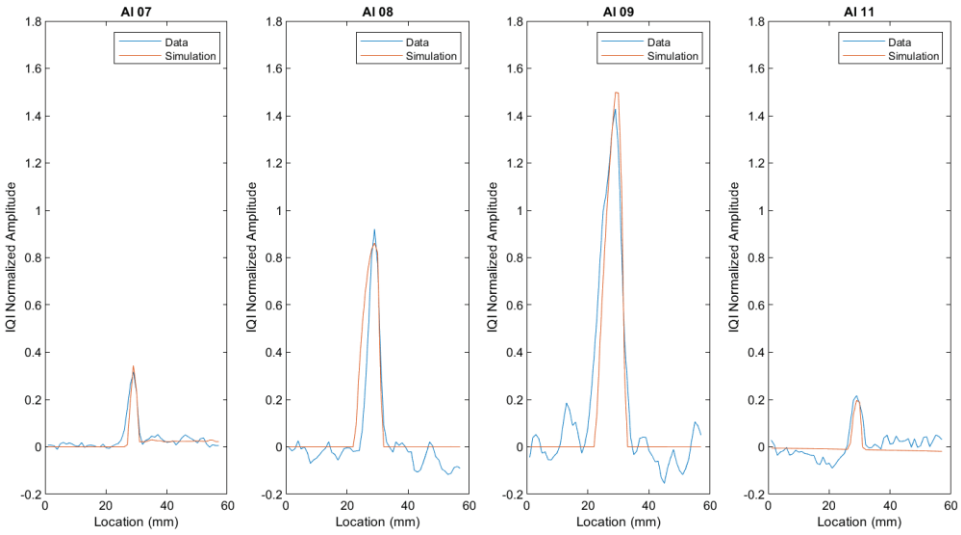

Figure 10.7.1-2. Aligned experimental results and simulations for 20° rotation

To provide a visualization of the cross sections of the half-elliptic cylinder used in the simulations of the canyons created by the etching, Figure 10.7.1-3 shows the surfaces of the canyon used in the simulations. For AL9, the simulation indicates the amount of material

removed at the crack opening was significantly more than the material removed for any of the other specimens.

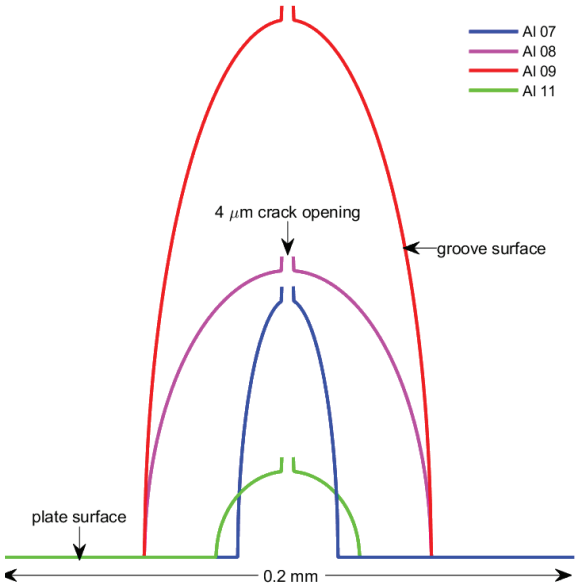

Figure 10.7.1-3. Relative shapes of the elliptic cylinder representation used in simulations for the surface canyons created by heavy etching

10.7.2 Equivalence of Etch Canyon, Wire IQI, and Plaque-Type Penetrameter / IQI

The canyon is similar to an IQI where the material is removed instead of a wire of the same material being placed on the surface. The relation between plaque (plaques are discussed in Section 7.2.2) thickness (p_e) for a hole IQI and a wire IQI with a diameter of d_e is given by [14]:

$$F^3 \, d_e^{\,3} \, l \; = \; p_e^{\,2} \, H^2 (\pi/4) \qquad (1\text{Eq. } 2)$$

from which the plaque thickness as a function of diameter is found to be

$$p_e = \frac{2\sqrt{l(F\,d_e)^3/\pi}}{H} \qquad (2\text{Eq. } 3)$$

where d_e is the effective diameter of the canyon, and l, the length of wire, is set to the length of the radiographic indication. F is a form factor for the wire equal to 0.79, and H is the hole size of interest. The effective diameter for each canyon (d_e) is approximated by the diameter of a circle with the cross-sectional area of the canyon and is given in Table 10.7.2-1. Hole size H is set to the minimum hole size of standard plaque IQIs of 0.254 mmmm (0.01 inch), which is greater than the 2% of the thickness of the thickest specimen of interest (for the thickest specimen, AL11, 2% of the thickness is 0.094 mm). The calculated effective plaque thickness for each of the canyons is given in Table 10.7.2-1 with 2% of the specimen thickness for each of the four specimens. If the plaque thickness is greater than 2% of the specimen thickness, then for a radiographic inspection where the required sensitivity is 2-1T, such as NASA-STD-5009C, this canyon should be detectable with film radiography. As can be seen from the table, all of the effective plaque thicknesses are greater than 2% of the specimen thicknesses, and all of the canyons should be detectable with film radiography.

Table 10.7.2-1 Diameter of equivalent wire IQI d_e and the plaque thickness p_e.

Specimen	d_e(mm)	Length(mm)	*t* Specimen Thickness(mm)	p_e Equivalent Plaque Thickness(mm)	2% of t (mm)
AL7	0.056	13.3	2.74	0.15	0.055
AL8	0.100	7.3	2.79	0.27	0.056
AL9	0.194	11.6	3.43	0.91	0.069
AL11	0.055	14.8	4.70	0.15	0.094

10.8 Summary of Radiography of Etched Specimens

Based on the Martin Marietta report, approximately 21% of the cracks examined for the Bishop POD study had radiographic detectabilities that were significantly increased by etching. The heavy etch performed on specimens in this report removed slightly more material than the Martin Marietta process (0.055-0.060 mm material removal for specimens in this report as compared to 0.051 mm removed by Martin Marietta). This degree of etching for Martin Marietta and heavy etch for this study makes the cracks visually detectable without magnification.

From the measurements (both from microscopic and radiographic imaging) performed for this report, etching preferentially erodes the region around the surface-breaking crack but does not produce a consistent amount of erosion. The etching performed for this report resulted in a sufficient amount of material loss that transformed previously undetectable cracks into detectable cracks. It is noted that for penetrant testing at NASA JSC PRC-6506 Ref F only specifies a minimum about of material to be removed for inspection.

It is estimated, based on equivalence with wire and plaque IQIs, that the canyons created by etching would be detectable with film radiography, regardless of the depth of the crack, assuming a 2-1T sensitivity for the film radiography. The etching that created these canyons is similar to the etching performed by Martin Marietta for the specimens used in the Bishop POD study and these canyons were visibly detectable as were the Martin Marietta canyons. Therefore, some significant portion of the cracks labeled as detectable in the Bishop POD study were likely detectable independent of the radiographic characteristics of the crack. In a POD study, the etched cracks should not have been included in the population of cracks examined. This study demonstrates that etching prior to X-ray inspection makes opens the cracks making them more detectable as compared to X-rays obtained without etching due to the increase in the crack face opening. Thus, the Standard NDE radiographic flaw sizes established based on testing of heavily etched crack samples may be nonconservative relative to standard practice requiring no etching. (See F-4)

For the specimens examined, the etching also enabled easy detection of the cracks at angles up to 20°. Likewise, etching could have impacted the incident angle measurement performed for the Bishop POD studies.

10.9 Analysis of Double-wall Radiography

This section reviews test data demonstrating how the addition of a second wall in double-wall radiographic inspections reduces the detectability of cracks. It has previously been suggested that double-wall radiography provides equivalent detection capability when there is sufficient wall separation such that the first wall only acts as an X-ray filter. Therefore, this section will examine the effect of the separation distance between the two walls on detectability.

10.9.1 Existing Publications on Double-Wall Radiographic Inspections

There is limited literature that delineates the difference in detectability between a single-wall, single-image pressure vessel inspection and a double-wall, single-image pressure vessel inspection. There is literature recommending using a single-wall inspection when possible. An example of such a recommendation is in ASME's Boiler and Pressure Vessel Code [17]: "A single-wall exposure technique shall be used for radiography whenever practical. When it is not practical to use a single-wall technique, a double-wall technique shall be used."

That a single-wall inspection is considerably more effective than a double-wall inspection is demonstrated in a paper by Bavendiek, *et al.* [18]. This paper compares the POD for single and double-wall inspection of EDM notches in a 10.16 cm diameter Inconel pipe with a wall thickness of 1.981 mm. Seventy-two EDM notches with 18 different volumes were created in the pipes. The probability of detection for the single-wall and double-wall film inspection as a function of EDM slot volumes is shown in Figure 10.9.1-1. The volume of EDM notches that resulted in 90% probability of detection for a single-wall inspection was 0.23 mm^3 while the 90% POD volume was larger (0.49 mm^3) for the double-wall inspection. Another indication of the better results using single-wall inspection was that for single-wall inspection, 79% of the EDM notches were detected, while for double-wall inspection only 56% of the EDM notches were detected. Although the effect may be material dependent and is not discussed here.

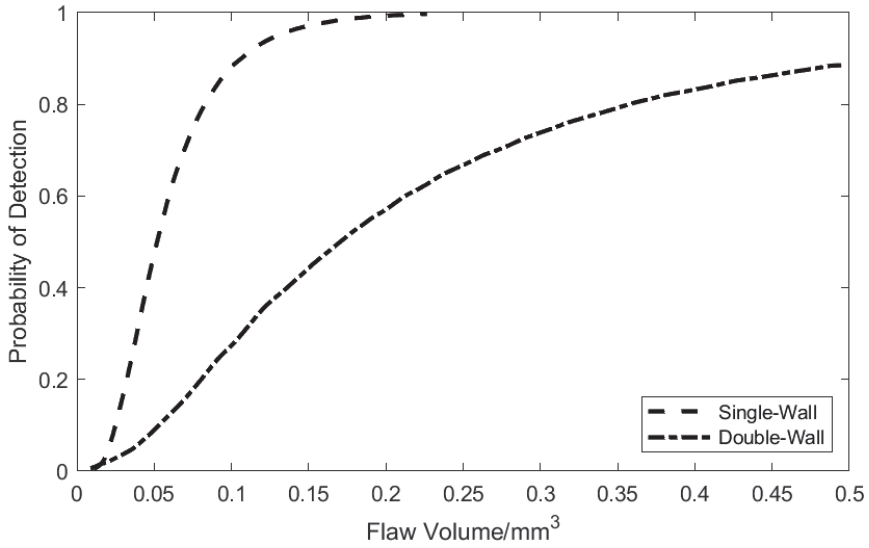

Figure 10.9.1-1. Comparison of single-wall and double-wall POD as a function of EDM notch volume for film radiography from Bavendiek et al.

It should be noted that EDM notches are not cracks, and PODs for EDM notches are not equivalent to PODs for cracks. Compared to fatigue cracks, EDM notches are very wide with well-defined geometries. "Cracks feature complex geometric morphologies related to material microstructure, residual stresses, material properties dispersions and so on." [19]. An important part of a POD study is obtaining cracks with the expected variety of crack morphologies.

10.9.2 Measurement procedure for comparing crack indication amplitude for double-wall to single-wall.

For the measurements taken in this report, a cylinder configuration was simulated with two flat plates. Flat plates with cracks are simpler to produce than cylinders with cracks. Assuming the diameter of the cylinder is large, the flat plates are a good approximation.

Before performing double-wall measurements, the cracked specimen was mounted on a rotation stage and a DR image was acquired. For double-wall measurements, a second uncracked plate (second wall of the cylinder) of the same material and thickness was placed at different locations between the flat panel detector and the cracked specimen without moving the cracked specimen. The second plate was placed at three different locations. The first location was as close as possible to the cracked specimen. The second location was approximately 15 cm from the cracked specimen and the third location approximately 70 cm from the cracked specimen. An illustration of the measurement setup is shown in Figure 10.9.2-1.

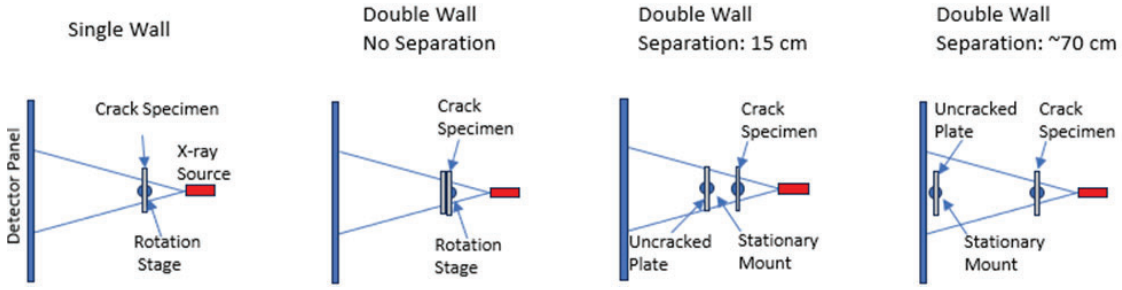

Figure 10.9.2-1. Measurement configurations for Double-wall Assessment (not to scale)

DR images were acquired on five different aluminum specimens (AL1, AL7, AL9, AL11, and AL36) and two different Inconel specimens (C7 and C9) in the four configurations shown in Figure 10.9.2-1. Before mounting the specimen in the system, an IQI was attached to the specimen parallel to the crack. The source voltage was kept constant for each set of measurements.

10.10 Results of Single- and Double-wall Measurements

10.10.1 Aluminum Double-wall Measurements

As examples, Figures 10.10.1-1, 10.10.1-2, and 10.10.1-3 show the data acquired in the region of the crack for three of the aluminum specimens. Starting from the left, the first three images in the figures are the cases of a second plate placed between the cracked sample and the detector (*i.e.*, equivalent to a double-wall inspection). The fourth image in the figures is the case of only the cracked plate (i.e., equivalent to a single wall inspection). The distance between the cracked sample and the second plate are given in the title of each image. All of the radiographs for a particular specimen (e.g., AL7) are displayed with the same intensity scaling.

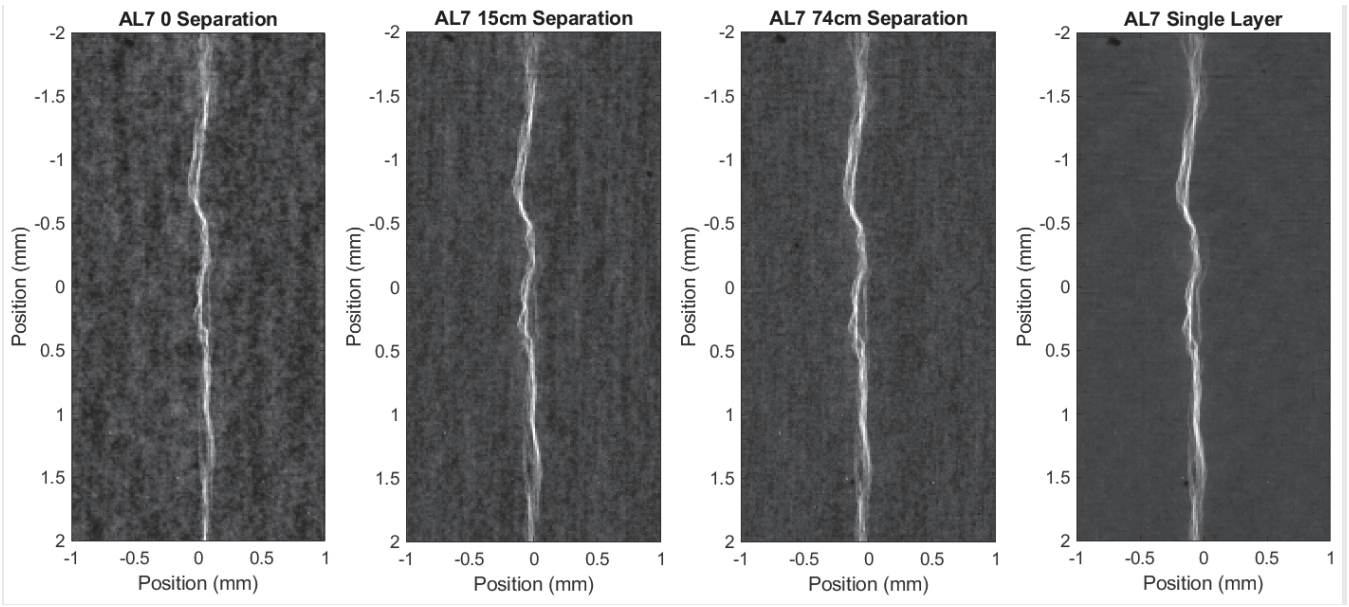

Figure 10.10.1-1. Data obtained for three different separations between the AL7 and a second plate with the same thickness and data obtained for AL7 alone. Plate separations are given in the titles for the images.

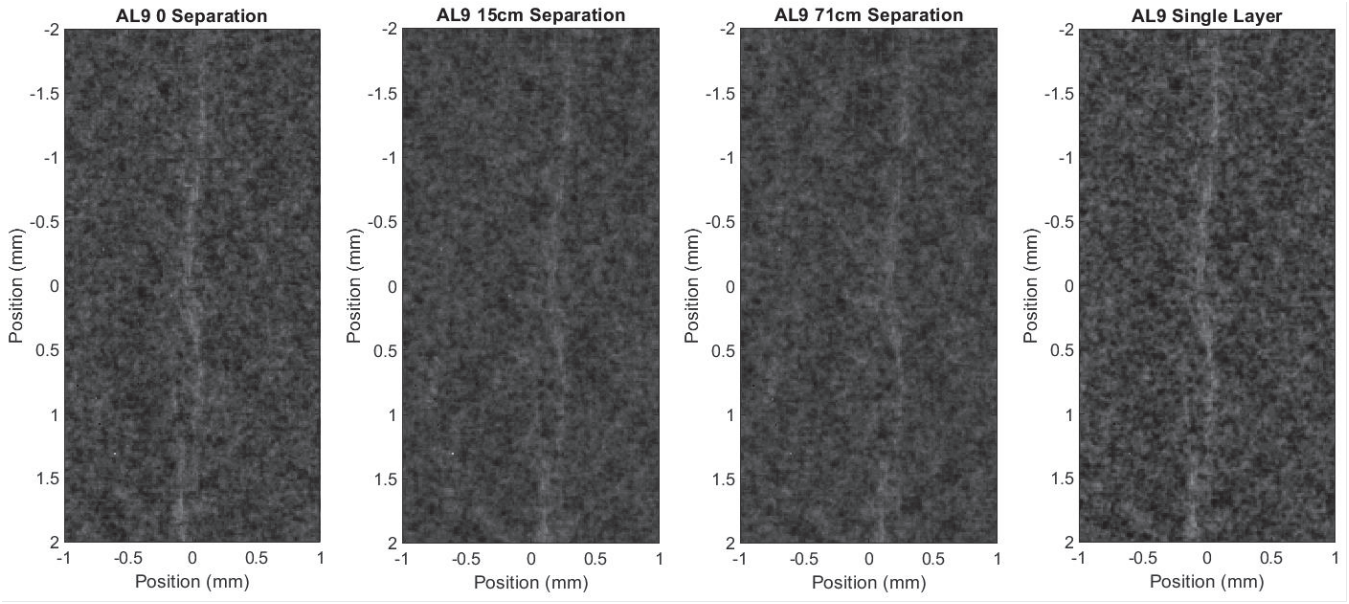

Figure 10.10.1-2. Data obtained for three different separations between the AL9 and a second plate with the same thickness and data obtained for AL9 alone. Plate separations are given in the titles for the images.

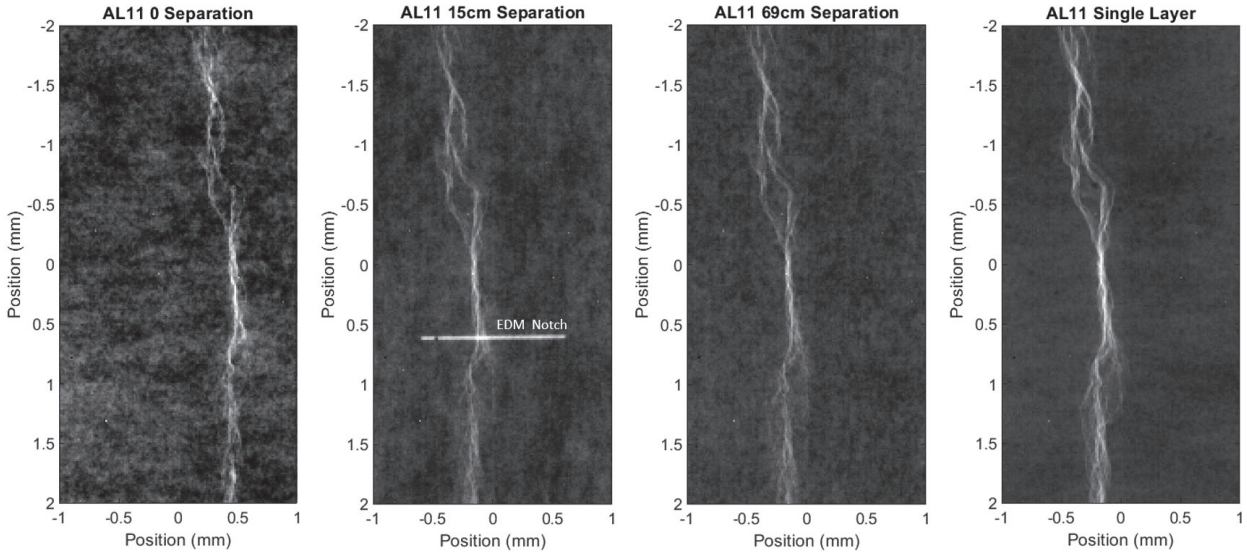

Figure 10.10.1-3. Data obtained for three different separations between the AL 11 and a second plate with the same thickness and data obtained for AL 11 alone. Plate separations are given in the titles for the images.

From a visual examination of the figures, it is difficult to discern a difference between three images for the double-wall configuration for all three cracked specimens. However, for all three specimens, the DR image in the single-wall configuration is less noisy. The crack in specimen AL9 visually has the least amount of contrast between the nominal material and the crack. The profiles and CNR values provide a more quantitative assessment.

Profiles created for each of the cracked specimens are shown in Figure 10.10.1-4. The profiles are normalized by dividing the measured values by the difference between the mean value in a nominal plate intensity adjacent region to the IQI and of the intensity of the plate plus the IQI. For all three of the specimens, the double-wall profiles look very similar when there is some spacing between the two plates. For all three specimens, single-wall amplitude is the largest of the four profiles, however the amplitude of the indication does not change dramatically for any of the configurations, only the noise. This is expected for two reasons: first, the indications are normalized to a fixed thickness of aluminum (IQI 0.127 mm). second, the cracks for all configurations displace the same mass of material out of the X-ray path between the source and detector, and the radiograph is simply a measure of the change in mass along that path. This is similar to the computational simulation results for the four configurations discussed in Section 10.12.

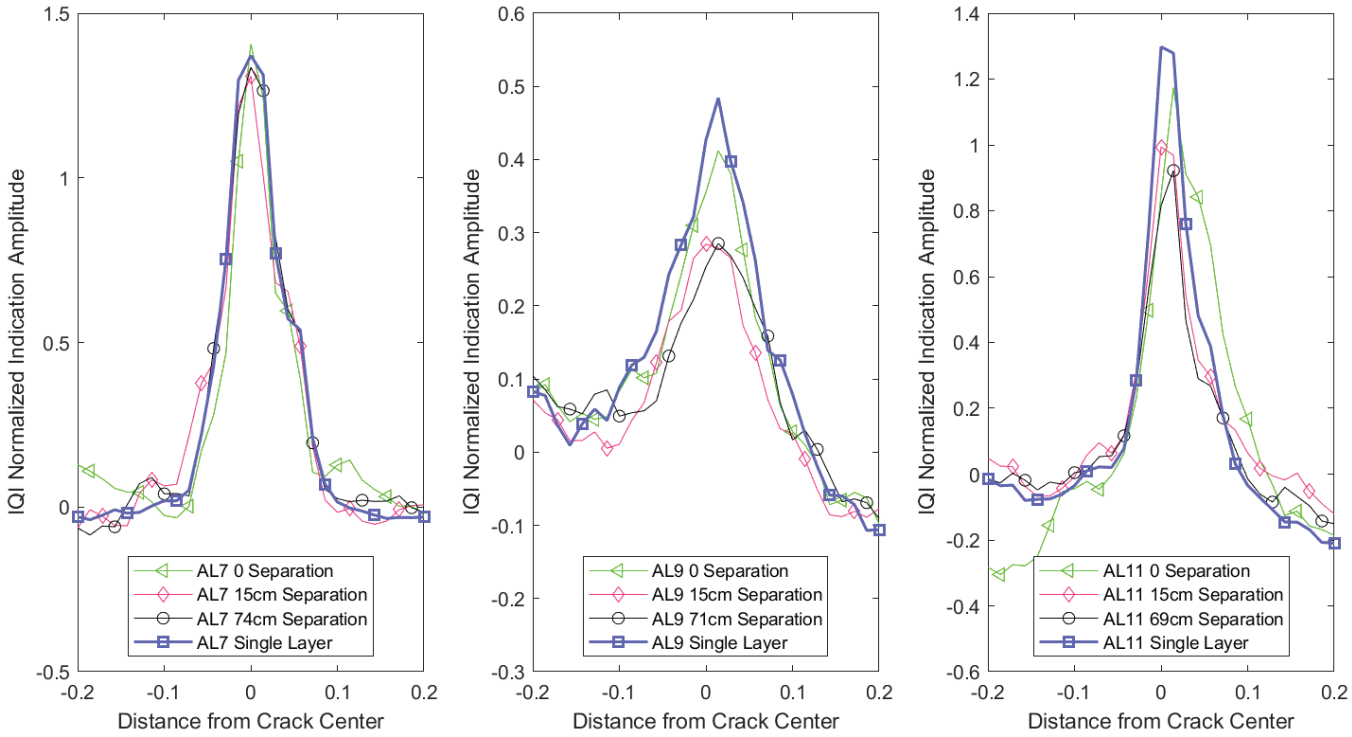

Figure 10.10.1-4. For data acquired on AL7, AL9, and AL11 the normalized indication amplitude as a function of distance from the center of the crack.

A more quantitative comparison is performed by calculating the CNR for the four configurations of the five different aluminum specimens. The CNRs for all the measurements are given in Table 10.10.1-1 along with the IQI normalized amplitude of the crack indication and the IQI normalized noise in the nominal material. An examination of the table shows that the indication amplitude for a given crack does not change significantly for any configuration, however, the noise does increase as would be expected when a second plate is placed between the crack and the detector. This is reflected in the CNR for a given crack, decreasing when a second plate is added. As seen in Figure 10.10.1-2, the crack in AL9 is least distinguishable in the radiograph and has the smallest CNR.

It can be concluded from these measurements that changing the spacing between the two aluminum plates, for the double-wall configuration, does not significantly change the detectability of the crack.

Table 10.10.1-1. Measured radiographic crack indication amplitude, noise and CNR for different aluminum double-wall and single-wall specimens and configurations

Specimen	Configuration	Separation (cm)	IQI Normalized Indication Amplitude	IQI Normalized Noise	Average CNR	Max CNR
AL 1	Double Layer	0	1.06	0.09	9.584	16.103
AL 1	Double Layer	20	1.06	0.10	10.212	15.015
AL 1	Double Layer	74	1.18	0.10	9.393	12.891
AL 1	Single Layer	0	1.11	0.07	10.385	17.584
AL 7	Double Layer	0	0.75	0.18	7.264	11.939
AL 7	Double Layer	15	0.72	0.11	10.251	17.149

Specimen	Configuration	Separation (cm)	IQI Normalized Indication Amplitude	IQI Normalized Noise	Average CNR	Max CNR
AL 7	Double Layer	74	0.62	0.09	21.100	13.370
AL 7	Single Layer	0	0.83	0.07	23.193	43.977
AL 9	Double Layer	0	0.19	0.15	2.093	4.28
AL 9	Double Layer	15	0.20	0.17	1.956	4.734
AL 9	Double Layer	71	0.19	0.20	1.882	4.412
AL 9	Single Layer	0	0.25	0.19	2.171	4.998
AL11	Double Layer	0	0.37	0.21	4.879	11.341
AL11	Double Layer	15	0.48	0.16	6.884	14.738
AL11	Double Layer	69	0.48	0.16	7.68	15.949
AL11	Single Layer	0	0.54	0.08	15.605	46.143
AL36	Double Layer	0	0.1	0.03	3.054	6.21
AL36	Double Layer	20	0.12	0.03	3.609	7.752
AL36	Double Layer	74	0.11	0.03	2.871	4.85
AL36	Single Layer	0	0.08	0.16	3.211	6.641

10.10.2 Inconel Double-wall Measurements

The following figures show the results of measurements on two Inconel specimens. Images of the data acquired in the region of the crack are shown in Figure 10.10.2-1 and Figure 10.10.2-2.10.10.2-2. The radiographs for specimen C7 have visible crack indications for all configurations, however, double-wall configurations have increased noise levels.

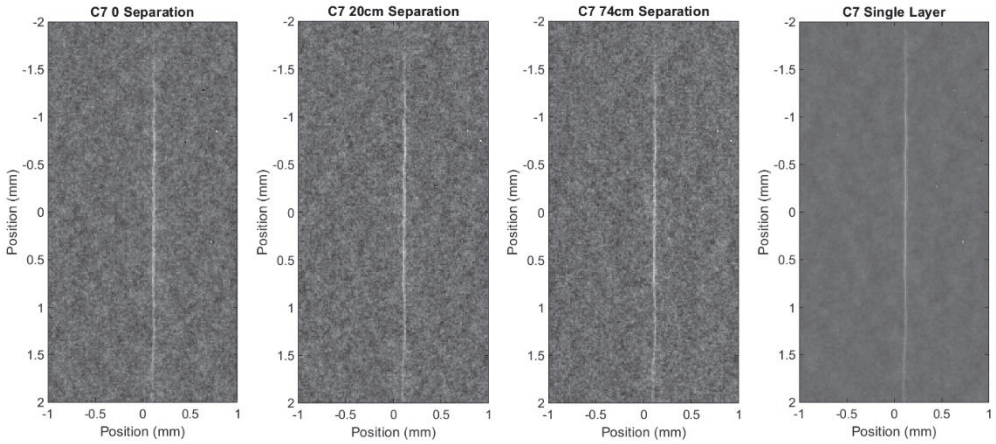

Figure 10.10.2-1. Data obtained for three different separations between the C7 specimen and a second plate with approximately the same thickness and data obtained for the C7 specimen alone. Plate separations are given in the titles for the images.

As was the case for specimen AL9, the crack indication in the double-wall configurations is not as definitive, however, if one knows it is there, it is visible. The crack indication in the single layer configuration is clearer.

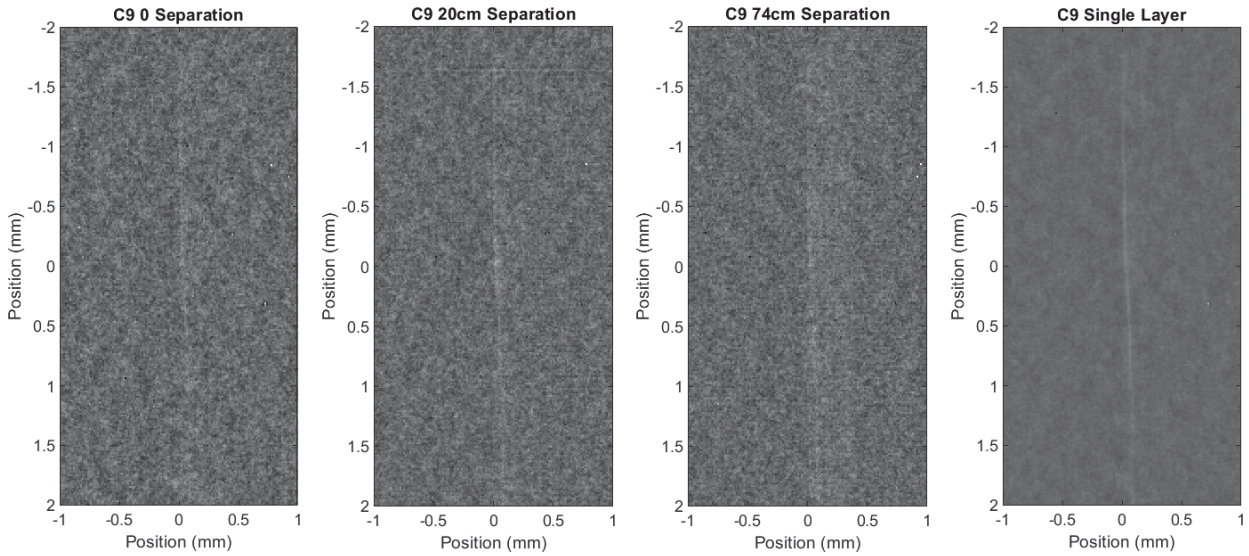

Figure 10.10.2-2. Data obtained for three different separations between the C9 specimen and a second plate with approximately the same thickness and data obtained for the C9 specimen alone. Plate separations are given in the titles for the images.

Profiles created for each of the cracked Inconel specimens are shown in Figure 1.10.2-3. For all the double-wall configurations, the indication amplitudes are about equal. The indication amplitude of the single wall configuration is smaller than the indication amplitude of the double-wall configurations, however, the noise in the nominal material is much smaller than for double-wall configurations. CNR is calculated by dividing by the standard deviation of the noise which would cause the CNR value to increase in the double wall configuration.

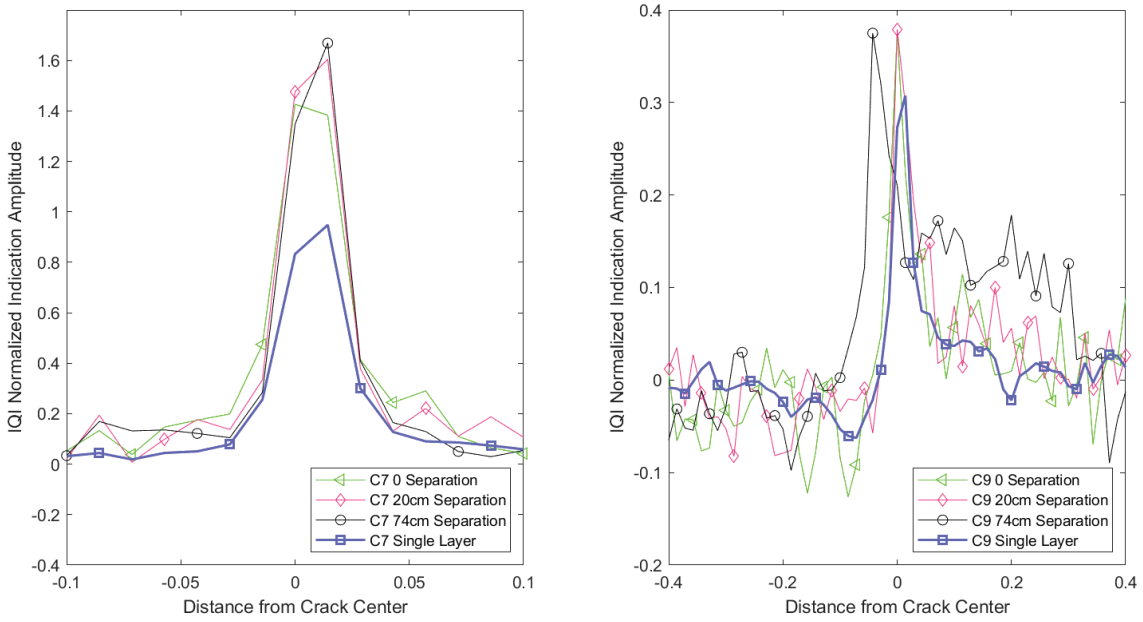

Figure 10.10.2-3. For data acquired on specimens C7 and C9, the normalized indication amplitude as a function of distance from the center of the crack

A more quantitative comparison is given in Table 10.2-1, which shows that the indication amplitude is independent of the spacing between the two walls. It also illustrates that CNR values for double-wall configurations are smaller than for the single-wall configuration.

Table10.10.2-1. Measured radiographic crack indication amplitude, noise, and CNR for different Inconel-Inconel double-wall and single-wall configurations.

Specimen	Configuration	Separation (cm)	IQI Normalized Indication Amplitude	IQI Normalized Noise	CNR	Max CNR
C7	Double Layer	0	1.07	0.380	4.216	6.549
C7	Double Layer	20	1.15	0.408	4.031	6.291
C7	Double Layer	74	1.14	0.411	3.609	6.030
C7	Single Layer	0	0.69	0.105	8.25	15.332
C9	Double Layer	0	0.26	0.38	1.054	1.842
C9	Double Layer	20	0.26	0.41	1.209	2.611
C9	Double Layer	74	0.27	0.41	1.167	2.238
C9	Single Layer	0	0.23	0.11	2.967	5.607

10.11 Change in CNR between Single Wall and Double Configurations

The difference in CNR between double-wall configurations and the single wall configurations are all given in Table 10.11-1. All but one of the double-wall configurations show a reduction in the CNR for the double-wall configuration relative to the single wall configuration. Inconel has a much more consistent reduction in the CNR than aluminum, with reduction of all the Inconel specimens being greater than 50%. It is easy to see from an examination of the Inconel radiographs in Figures 10.10.2-1 and 10.10.2-2 that the noise in the double-wall configuration is considerably greater than in the single wall configuration.

Table 10.11-1. Combined Aluminum and Inconel Double-wall CNR Reduction compared with single wall configuration for Different Wall Separations

Specimen	Thickness(mm)	Separation(cm)	Percent Reduction Average CNR	Precent Reduction Max CNR
AL1	10.39	0	7.8	8.4
AL1	10.39	20	1.7	14.6
AL1	10.39	74	9.6	26.7
AL7	2.74	0	68.7	72.9
AL7	2.74	15	55.8	61
AL7	2.74	74	9	69.6
AL9	3.43	0	3.7	14.4
AL9	3.43	15	9.7	5.4
AL9	3.43	71	13.4	11.8
AL11	4.7	0	68.7	75.4
AL11	4.7	15	55.9	68.1
AL11	4.7	69	50.8	65.4
AL36	12.7	0	5	6.5
AL36	12.7	20	-12.5	-16.7

Specimen	Thickness(mm)	Separation(cm)	Percent Reduction Average CNR	Precent Reduction Max CNR
AL36	12.7	74	10.6	27
AL37	18.53	0	49.1	50.1
AL37	18.53	15	6.2	23.8
AL37	18.53	74	9.4	19.8
C7	4.37	0	48.8	57.3
C7	4.37	20	51.2	59
C7	4.37	74	56.2	60.7
C9	3.96	0	64.6	67.2
C9	3.96	20	59.3	53.5
C9	3.96	74	60.6	60.1
Average CNR Reduction			31.8	40.1

AL36, one of the thicker specimens, shows an increase in CNR between the double wall and single wall when the separation was 20 cm. The normalized indications for these two configurations are shown in Figure 10.11-1. The indication amplitude is smaller for the single wall configuration, which may be a result of the specimen being slightly moved after the single wall data were taken. An examination of the two radiographic images shows for the single wall configuration the crack indication is displaced from center by about 0.2 mm, while for the 20 cm separation the crack indication is at the center of the image. The noise for the double-wall configuration is greater than the single wall configuration noise, however, the indication amplitude-to-noise ratio for the single wall is less than the indication amplitude-to-noise ratio for the double-wall configuration.

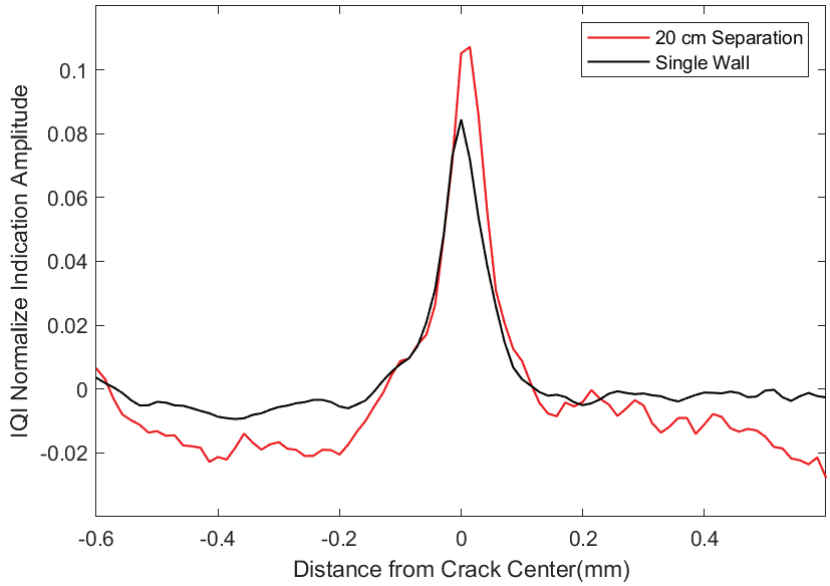

Figure 10.11-1. Comparison of the normalized indication of AL36 single wall and double-wall with 20 cm separation

10.12 Computational Simulations of Double-wall Inspection

Simulations were performed using the commercial NDE simulation package CIVA. This enabled the examination of different materials and geometries of COPV tanks of interest to NASA. The simulations were performed assuming the detector was film, and the output of the simulation was an image of the film density. To get reasonable images of the cracks, the detector spacing was set to 0.5 μm, then the resulting image was convolved with a filter that assumed the film resolution was 20-line pairs per millimeter. This seemed to be a good approximation based on literature on film resolution, however, we were unable to find any exact characterization of film resolution.

To perform the simulation, for each material/total thickness combination, the X-ray voltage was varied in steps of 5 keV while keeping the current-times-exposure equal to 1000 mA-sec until the optical density of the plate away from the crack was approximately 3. The current-times-exposure was then changed until the film density of the base plate was close to 3. For the aluminum configuration discussed in the previous paragraph, these parameters were found to be 35 keV and a current-times-exposure of 1500 mA-sec. The acceleration voltages and exposures for each of the material/total thickness combinations are given in Table 10.12-1. As can be seen in Table 10.12-2, the simulated film density of nominal material is very close to 3.

Table 10.12-1. Simulation X-ray source acceleration voltage and exposure for different material and total thickness combinations

Material	Configuration	Total Thickness mm	Acceleration Voltage keV	Current-times-exposure mA-Sec
Al 2219	Single Wall	1.27	30	590
Al 2219	Double Wall	2.54	40	727
Inconel	Single Wall	1.016	85	900
Inconel	Double Wall	2.016	100	1436
Ti-6Al-4V	Single Wall	0.763	55	1160
Ti-6Al-4V	Double Wall	1.524 (0.060)	70	1948

Cracks were assumed to be a set of randomly oriented segments as can be seen in Figure 10.12-1. This is similar to the “periodically kinked crack” model used for predication of fatigue crack growth [20]. For all materials, an IQI equal to 2% (IQI1) thickness of the single wall was included in the simulation. The crack height was set to 70% of the single wall thickness. The crack gap was linearly reduced from a surface opening gap of 1.5 μm to 0.5 μm at the tip of the crack. This resulted in a crack indication amplitude in the convolved image approximately equal to the IQI1 amplitude.

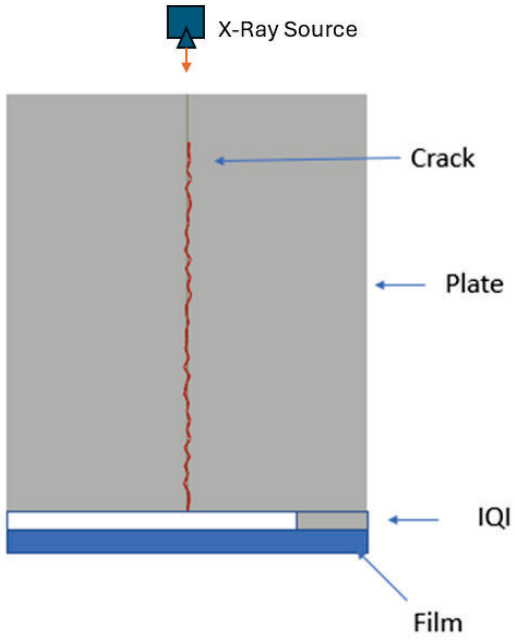

Figure 10.12-1. Side view of simulation configuration for a single wall with randomized crack path.

The amplitude of the IQI1 is used to normalize the profile of the change in film density. A typical set of optical density profiles across the crack is shown in Figure The simulated configuration is a single aluminum plate with a thickness of 1.27 mm and a crack depth of 70% of the thickness (0.889 mm) and three double-wall configurations. The first double-wall configuration is two walls in contact (*i.e.*, with no separation) with a thickness of 1.27 mm each, with a crack depth 70% of the 1.27 mm (0.889 mm) which is 35% of the 2.54 mm total thickness. The second set of configurations is two plates, each of 1.27 mm thickness, and an outer wall separation of 15.24 cm. The third set of configurations is similar to the second, except the configuration is a cylinder with an outer wall diameter of 15.24 cm and a wall thickness of 1.27 mm. Both have cracks 0.889 mm deep.

For film radiograph, the film transparency is what the inspector views and an instrument is required to convert the transparency to the film density. The density and the transparency are two different ways of displaying the same data. CIVA calculates film density, and the film transparency is calculated from the film density. The film densities given in the simulations are converted to changes in transparency and normalized such that the change in transparency of IQI1 is 1. The change in normalized indication transparency is shown in Figure Since transparency of the film decreases exponentially with increased film density, a change over the crack is negative.

Both Figure 10.12-2 and Figure 10.12-3 show that a change in plate separation for the double-wall inspection does not significantly change the profiles for film density or film transparency when normalized to the IQI1.

Double-wall simulations were also normalized by an IQI (IQI2) whose thickness is 2% of the total wall thickness for both walls (so IQI2 is twice the thickness of IQI1). Table 10.12-2 shows when the double-wall images are normalized by the IQI2, the indication

amplitude for all double-wall configurations is considerably smaller than for the 2% of the total wall thickness crack.

Simulations were also performed assuming walls fabricated of Inconel and Ti-6Al-4V with different ODs. The details of all the configurations are given in Table 10.12-2**Error! Reference source not found.**. For all of the simulations performed, there was no significant change in the amplitude of the crack indication, when there was no separation or significant separation. The Standard NDE flaw size of 0.7t is not reasonable for a cylinder since a crack of 0.7t of the total thickness (two walls) is greater than the thickness of one of the layers.

As can be seen in the Figures 10.12-2 and 10.12-3, the amplitudes of all the indications are approximately the same for all configurations, both single wall and all the different separations for the double-wall regardless of the separation of the walls. This is similar to the measurement results shown in Figure 10.10.1-4 for AL 7, AL9, and AL11. This is reasonable since the mass displaced by the crack, out of the path of the X-ray, is the same for all configurations and all the configurations are normalized to the same change in density for a relatively small change in mass along the path, i.e., the same as the mass added by the IQI. The change in film densities for the crack and IQI1 are all small, approximately 0.1 or less.

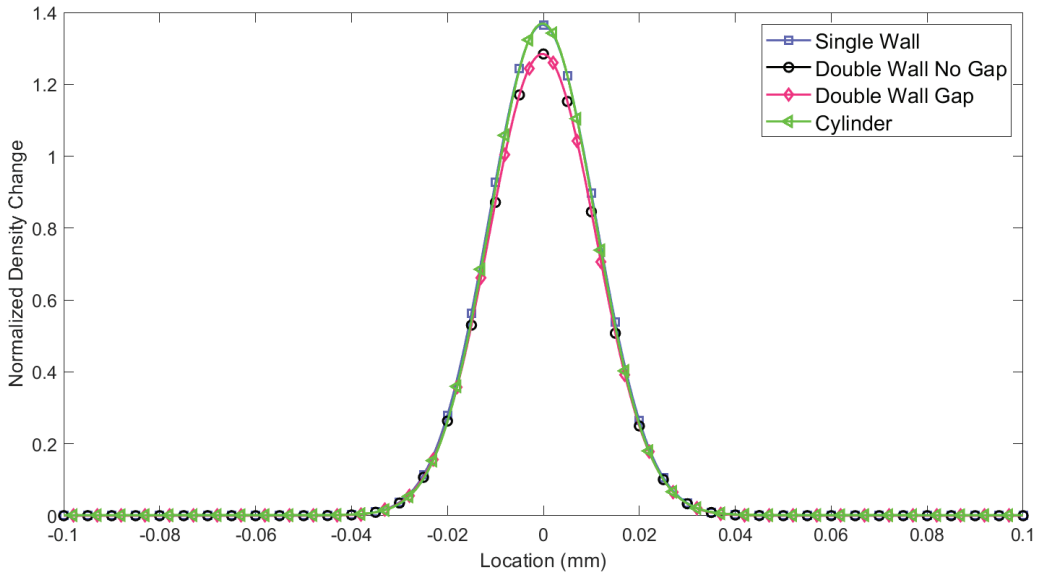

Figure 10.12-2. Change in normalized optical density profiles across the crack in aluminum plates with specifics of different configurations in the text

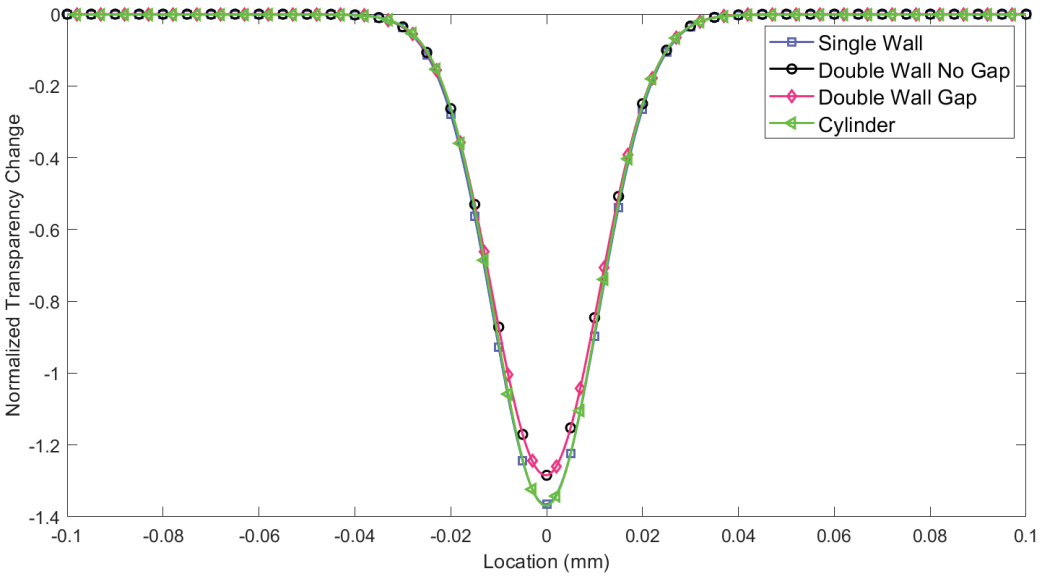

Figure 10.12-3. Normalized change in film transparency profiles across the crack in aluminum plates with specifics of different configurations in the text

IQI 1 has a thickness that is 2% of the thickness of single wall, therefore the IQI is specified for a single-layer inspection. However, the IQI 2 thickness is the proper thickness of an IQI for a double-wall inspection or 2% of the combined thicknesses of the two walls. Therefore, the indication of the double-wall is smaller than the proper IQI (*i.e.* IQI 2), therefore less likely to be detected than if the same crack was part of a single wall inspection.

CIVA can be configured to simulate noise based on an estimation of the quantum noise of the detector. A measure of the noise in normalized images is also given in Table 10.12-2. Similar to the experimental measurements, the noise in the double-wall configurations is always larger than the noise in the single-wall configuration.

Based on the simulation noise and the indication amplitudes, the CNR for all the configurations are also given in Table 10.12-2. Similar to the measurements, the CNR is reduced by the presence of a second wall. On average, the reduction is 50%. This indicates a 0.7t crack in a single wall of a double-wall configuration would be more difficult to detect than a 0.7t crack in a single wall configuration, and one cannot rely on single wall inspection validation for a double-wall inspection. A double-wall radiographic inspection should therefore be considered as "special NDE."'

Table 10.12-2. Simulation Results for Single-wall, Double-wall, and Cylinders for Materials and Thicknesses of typical COPVs

Material	Total Thickness (mm)	Crack depth(mm)	Configuration	Nominal Material Film Density	Normalized Density Change IQI 1	Normalized Density Change IQI 2	Normalized Crack Transparency	Normalized Density Noise	CNR
AL	1.27	0.889	Single Wall	3.02	1.365		-1.005	0.103	13.3
AL	2.54	0.889	Double-wall no separation	3.03	1.284	0.648	-1.111	0.174	7.4

Material	Total Thickness (mm)	Crack depth(mm)	Configuration	Nominal Material Film Density	Normalized Density Change IQI 1	Normalized Density Change IQI 2	Normalized Crack Transparency	Normalized Density Noise	CNR
AL	2.54	0.889	Double-wall 15.24 cm OD	3.00	1.284	0.648	-1.113	0.175	7.3
AL	2.54	0.889	Cylinder 15.24 cm OD	3.03	1.369	0.691	-1.180	0.164	8.3
Inconel	1.016	0.711	Single Wall	3.00	1.290		-1.013	0.123	10.5
Inconel	1.016	0.711	Double-wall no separation	3.02	1.248	0.629	-1.065	0.218	5.7
Inconel	1.016	0.711	Double-wall 55.88 cm OD	3.01	1.248	0.629	-1.066	0.208	6.0
Inconel	1.016	0.711	Cylinder 55.88 cm OD	3.05	1.189	0.599	-1.018	0.219	5.4
Ti-6Al-4V	0.763	0.534	Single Wall	2.99	1.303		-0.985	0.080	16.2
Ti-6Al-4V	0.763	0.534	Double-wall no separation	3.00	1.245	0.634	-1.085	0.179	6.9
Ti-6Al-4V	0.763	0.534	Double-wall 58.42 cm OD	2.96	1.245	0.634	-1.087	0.200	6.2
Ti-6Al-4V	0.763	0.534	Cylinder 58.42 cm OD	3.01	1.278	0.651	-1.111	0.168	7.6

10.13 Summary of Double-wall Inspection

The consensus recommendation in inspection manuals is a single wall radiographic inspection is advisable over a double-wall radiographic inspection, which certainly implies a single wall inspection is more sensitive to flaws.

POD studies in the literature for a single wall and double-wall radiographic film inspection of EDM notches indicate smaller volume of EDM notches are significantly more detectable with the single wall inspection than a double-wall inspection.

Both measurements and simulations indicate there is a significant reduction in the CNR when a second wall is inserted in the path between the source, wall with the crack, and detector.

For the double-wall inspection, both the measurements and the simulations indicate the separation between the walls does not significantly impact the CNR for the configurations tested in this report. An inspection validation study performed with a one spacing should be adequate for all spacing.

Modeling and inspections demonstrated a decrease in contrast in radiographic images obtained in double-wall test configurations as compared to testing the same crack sample in a single wall test configuration. This loss of signal is consistent with previous Special NDE demonstrations showing that the special POD is reduced when testing in double-wall configurations as compared to single wall inspection. (See F-5, F-6, and F-7)

11.0 Findings

F-1. The historical POD study that derived the Standard NDE flaw size for radiographic testing in NASA-STD-5009C included inspections that spanned beam angles of ±5° (i.e., the current 5009C limit).

F-2. Analysis of the historical radiographic POD study data showed that etched RT flaw detection capability deteriorates with increasing beam angles exceeding 2.4°. However, the study data are insufficient to determine the angle where POD is reduced below the 90/95 requirement, although the data suggest that an angle between 3.6° and 4.8° is acceptable. Thus, the historical POD study data is insufficient to support or refute the ±5° requirement in NASA-STD-5009C.

F-3. DR etched Image analyses of inspections from a limited number of samples showed a loss in amplitude of approximately 40% at the current beam angle limit of ±5° allowed in NASA Standard 5009C.

F-4. This study demonstrated that etching prior to X-ray inspection makes cracks more detectable due to an increase in the crack face opening as compared to X-rays obtained without etching cracks. Thus, the Standard NDE radiographic flaw sizes established based on testing of heavily etched crack samples may be nonconservative relative to standard practice requiring no etching.

F-5. While a formal, quantifiable transfer function was not developed as required by NASA-STD-5009, CT modeling and DR testing did not demonstrate significant signal loss due to the effects of plate spacing between walls for double-wall inspection configurations compared to single-wall configuration.

F-6. CT modeling and DR inspections demonstrated a decrease in contrast in radiographic images obtained in double-wall test configurations compared to testing the same crack sample in a single wall test configuration. This loss of signal is consistent with previous Special NDE demonstrations showing that the POD is reduced when testing in double-wall configurations compared to single wall inspection.

12.0 Observations:

O-1. In addition to the concerns relative to the Standard NDE radiographic flaw size investigated in this study, NASA/TM−20220013820, A Survey of NASA Standard NDE, identified additional concerns that may lead to the values being nonconservative due to inadequate flaw size distributions in the test samples and issues with the original POD analysis techniques.

O-2. Current Standard NDE radiographic flaw sizes apply to film radiography, which was used in the historical POD test program. However, film is becoming less readily available as the industry transitions to digital radiographic methods, which currently must be treated as Special NDE inspections.

O-3. Testing was limited to a small number of crack specimens in materials that were thicker than pressure vessels of inspection interest. However, the thicker specimens are thought to introduce a larger amount of material inhomogeneity, and thus the results may be bounding in terms of deteriorating POD of thinner materials of inspection interest.

13.0 Recommendations:

Recommendations are directed toward JSC Engineering.

R-1. Make no immediate changes to the current ±5° limit between the X-ray beam and assumed crack plane requirement for Standard NDE, film based, X-ray inspections. (***F-1, F-2, F-3***)

R-2. Perform all double-wall radiographic qualification testing as Special NDE utilizing double-wall mock-up testing configurations. If crack panels are not available that are representative of the vessels to be inspected, assess similarity of available crack panels. (***F-5, F-6, F-7***)

R-3. Consider planning and performing a new Standard NDE radiographic POD test program to include both film and digital radiographic media in accordance with the NASA Guidebook/TM on Design and Analysis of Standard NDE Study. (***F-1, F-2, F-3, F-4, O-1, O-2***)

14.0 Alternate Technical Opinion(s)

No alternate technical opinions were identified during the course of this assessment by the NESC assessment team or the NESC Review Board (NRB).

15.0 Other Deliverables

No unique hardware, software, or data packages, other than those contained in this report, were disseminated to other parties outside this assessment.

16.0 Recommendations for the NASA Lessons Learned Database

No recommendations for NASA lessons learned were identified as a result of this assessment.

17.0 Recommendations for NASA Standards, Specifications, Handbooks, and Procedures

No recommendation for NASA standards, specifications, handbooks or procedures were identified as a result of this assessment.

18.0 Definition of Terms

Finding	A relevant factual conclusion and/or issue that is within the assessment scope and that the team has rigorously based on data from their independent analyses, tests, inspections, and/or reviews of technical documentation.
Lesson Learned	Knowledge, understanding, or conclusive insight gained by experience that may benefit other current or future NASA programs and projects. The experience may be positive, such as a successful test or mission, or negative, as in a mishap or failure.
Observation	A noteworthy fact, issue, and/or risk, which is not directly within the assessment scope, but could generate a separate issue or concern if not

addressed. Alternatively, an observation can be a positive acknowledgement of a Center/Program/Project/Organization's operational structure, tools, and/or support.

Recommendation — A proposed measurable stakeholder action directly supported by specific Finding(s) and/or Observation(s) that will correct or mitigate an identified issue or risk.

19.0 Acronyms and Nomenclature List

3D	three-dimensional
CNR	Contrast to Noise Ratio
COPV	Composite Overwrapped Pressure Vessel
CR	Computed radiography
CT	Computed testing
DR	Digital radiography
EDM	electro discharge machined
IP	Imaging plate
IQI	image quality indicator
NDE	Nondestructive evaluation
NESC	NASA Engineering and Safety Center
NRB	NESC Review Board
POD	Probability of detection
ROI	Region of interest
RT	Radiographic testing
t	thickness

20.0 References

[1] Bishop, C. R. (1973). *Nondestructive Evaluation of Fatigue Cracks.* Rockwell International-Space Division.

[2] Rummel, W. D., Todd Jr, P. H., Frecska, S. A., & Rathke, R. A. (1974). *The detection of fatigue cracks by nondestructive testing methods.* Martin Marietta.

[3] Anderson, R. T., T. J. Delacy, and R. C. Stewart. (1973). Detection of fatigue cracks by nondestructive testing methods. Convair Aerospace

[4] ASTM E1025-18 (2018) Standard Practice for Design, Manufacture, and Material Grouping Classification of Hole-Type Image Quality Indicators (IQI) Used for Radiography.

[5] ASTM E2737-10 (2018) Standard Practice For Digital Detector Array Performance Evaluation and Long-Term Stability.

[6] Rose, A. (1973). Vision: human and electronic. In Applied Solid State Physics (pp. 79-160). Boston, MA: Springer US.

[7] Tisseur, D., Létang, J. M., & Banchet, J. (2007, July). Phase contrast imaging in laboratory. In Proceedings of DIR (pp. 25-27).

[8] Schindelin, J., Arganda-Carreras, I., Frise, E., Kaynig, V., Longair, M., Pietzsch, T., … Cardona, A. (2012). Fiji: an open-source platform for biological-image analysis. Nature Methods, 9(7), 676–682.

[9] Ruescher, E. H. (1973). Influence of some X-ray penetrameters on crack detection capability. Materials Evaluation, 31(8), 152-154.

[10] "Nondestructive Inspection Methods, Basic Theory", TO 33B-1-1, NAVAIR 01-1A-16-1,TM 1-1500-335-23, page 6-151 (33B-1-1 (af.mil)).

[11] King, J. R., Julian, P., & Johnson, K. R. (1974). Space Shuttle Orbiter Fracture Control Plan (No. SD73-SA-0082A).

[12] Parker, P. A., Koshti, A., Forsyth, D. S., Suits, M. W., Walker, J. L., & Prosser, W. H. (2022). A Survey of NASA Standard Nondestructive Evaluation (NDE). NASA/TM-20220013820.

[13] Salkowski, C. (1995). Nondestructive inspection reliability assumptions for critical aerospace components. In Nondestructive Evaluation of Aging Aircraft, Airports, Aerospace Hardware, and Materials (Vol. 2455, pp. 449-457). SPIE.

[14] ASTM E747-18, A. (2018). Standard Practice for Design, Manufacture and Material Grouping Classification of Wire Image Quality Indicators (IQI) Used for Radiology. ASTM.

[15] Halmshaw, R. a. (1995). Radiographic techniques: sensitivity. Industrial Radiology: Theory and practice. Springer Link.

[16] Rummel, W. D. (1975). The detection of tightly closed flaws by nondestructive testing (NDT) methods. No. NASA-CR-144639.

[17] ASME, Boiler and Pressure Vessel Code. Section V. Nondestructive Examination (2019). Article 2 - Radiographic Examination.

[18] Bavendiek, K., Heike, U., Meade, W. D., Zscherpel, U., & Ewert, U. (2006). New digital radiography procedure exceeds film sensitivity considerably in aerospace applications. In 9th European Conference on NDT (pp. 1-16). European Federation for Non-Destructive Testing.

[19] Carpinteri, A., Spagnoli, A., & Terzano, M. (2019). Crack morphology models for fracture toughness and fatigue strength analysis. Fatigue & Fracture of Engineering Materials & Structures, 42(9), 1965-1979.

[20] Carpinteri, Andrea et al. "Influence of the crack morphology on the fatigue crack growth rate: A continuously kinked crack model based on fractals. Engineering Fracture Mechanics 75.3-4 (2008): 579-589

[21] Boucher, M. Fabrice, et al. "An overview of validation campaigns of the CIVA simulation software." *NDT. net: Gothenburg, Sweden* 9 (2018).

Appendix

A.1 Computational Simulation of the Radiographic Inspection Technique

Simulations of the radiographic technique were performed to support this effort and discussed in the sections on double-wall inspections and the effects of etching on radiographic crack detection. This section is intended to assist future attempts to simulate radiographic images of cracks in structures. While all of the simulations were performed with the EXTENDE CIVA, NDT Simulation Software using the RT Simulation Module some of the setup parameters may be important to consider even if other software is used. It is important to note regarding the simulations that there is no expectation that the simulations will give the absolute values of measurement results, such as the exact change in the film density, or the exact number of photons detected even within the bounds of the counting noise; however, the simulations are expected to provide reasonable trends in the measurements. This is a result of the simulation being based largely on theoretical values such as what is the X-ray absorption of a particular element, and the Kramer model estimates the X-ray spectrum of a tungsten tube for a given electron acceleration. Empirical models relate the film density change to a given exposure.

A typical setup was a rectangular block of an alloy of interest. For simulations including a thin layer (IQI) that is typically 2% of the block thickness is used. The initial thickness of the block is set as the desired thickness of an experiment thickness, then a thin plate region of the block measuring the thickness of the IQI is removed from a portion of the measurement regions, leaving two thicknesses in the measurement region: one thickness of the experimental block; and one, the thickness of an IQI plus the experimental block. The width and length of the block are always set to greater than 30 mm, to ensure the edge of the block was not in the simulation field of view. By normalizing the simulation results to the change in intensity between the block and the block-plus-IQI, as was done in the measurements performed at MSFC and LaRC, it is expected the simulation would correlate well with the experimental results if specimen geometry were accurately represented.

EXTENDE CIVA does not have the alloys of interest for this study, however, does allow for the creation of alloys based on the percentage of atoms in the mixture. For Al 2219, Inconel 718, and Ti-6Al-4V, the percentage of each element by weight was based on a web search for the alloys. For each, there is a range mass percentage for each element, such as for Al 2219, copper content can range from 5.8% to 6.8% by weight, which changes the absolute absorption of X-rays; however, is unlikely to yield an absolute difference in the simulations greater than the experimental error or other unknowns in the simulations. From the mass compositions the atomic percentage of atom is calculated.

A ‘Kramer model’ in the module is used to generate the X-ray spectrum. Inputs for the model are acceleration voltage, energy step normally chosen to be approximately 0.5 keV, anode material (tungsten) and anode angle which was 25° for all simulations. Smaller steps can be used, however, this was not found to significantly change the results and it increased the computation time. No filter between the tube and the specimen, with the expectation that the lower X-ray energies were totally attenuated by the specimen block. 1 mA was always assumed to be the electron current. All exposures were defined in terms of mA-sec.

For comparison to the digital radiography and computed radiography, the specimen location was fixed, and the source and detector were rotated in opposite directions around a center of reference either within the specimen or close to one of the surfaces of the specimen. For measurements as multiple rotations, multiple angles of rotation can be performed with "Parameter Study" by creating a file with the proper source location and rotation and detector location and angle. It was advantageous to reduce the number of output images saved to disk by opening the 'Storage' window and selecting only the images of interest such as 'Radiography' and 'Radiography no noise.'

For the Radiographic Module of EXTENDE CIVA, a small detector spacing is required to capture small defects such as cracks. Since the routine is effectively a ray-tracing routine, if the ray does not intersect the flaw, it has no effect on the output radiographs. If a detector spacing is chosen to be equal to the 0.5 microns for cracks with 5-micron gap openings when the simulated detector is flush to the specimen should be used. For the digital radiography with the source 87.143 mm from the source to the crack surface of the specimen and 1132.857 mm from the center of the detector and the crack surface of the specimen. This results in a geometric magnification of 14. For this case, the detector size was 20 microns, giving an effective detector size at the surface of the specimen of approximately 1.43 microns.

Early studies used straight prism cracks with 5 micron opening gaps and 0 microns as the tip. The produced radiographic images were found to not accurately represent the experimental data particularly when the rays were aligned with the axis of the crack. Better agreement was found by representing the crack as a series of equal-length segments with randomly varying angles and monotonically decreasing gap width as the crack moves deeper in the layer. This is similar to the "periodically-kinked crack" model used for predication fatigue crack growth, Carpinteri (2008). To incorporate the segmented crack into CIVA, the CIVA configuration with a specimen of the desired thickness but no crack, source and detector specification is created and saved as an Extensible Markup Language file. This file is modified by a MATLAB routine that incorporates the segmented crack. This file is opened with CIVA, and the simulation is run.

In general, the computational simulations produced results that are in qualitative agreement with the experimental measurements performed. To obtain quantitative results, additional information would be required, of utmost importance the morphology of the crack. A characterization of the detector panels would also be necessary — in particular, the quantum efficiency and sensitivity to energies of interest. There are other more accurate models for the X-ray source which could be easily incorporated; however, the Kramer model employed within CIVA is unlikely one of the major sources of discrepancies. Obtaining quantitative agreement between the simulation results and DR measurements was considered beyond the scope of this study. No film measurements were performed for comparison with the computational film simulations.